U.S. DEPARTMENT OF ENERGY

PNNL-18869

Prepared for the U.S. Department of Energy
under Contract DE-AC05-76RL01830

Improving the Physics Impact of ^{76}Ge Neutrinoless Double-Beta Decay Experiments

TW Hossbach

June 2009

Pacific Northwest
NATIONAL LABORATORY

Proudly Operated by Battelle Since 1965

DISCLAIMER

PACIFIC NORTHWEST NATIONAL LABORATORY
operated by
BATTELLE
for the
UNITED STATES DEPARTMENT OF ENERGY
under Contract DE-AC05-76RL01830

Printed in the United States of America

Available to DOE and DOE contractors from the
Office of Scientific and Technical Information,
P.O. Box 62, Oak Ridge, TN 37831-0062;
ph: (865) 576-8401
fax: (865) 576-5728
email: reports@adonis.osti.gov

Available to the public from the National Technical Information Service
5301 Shawnee Rd., Alexandria, VA 22312
ph: (800) 553-NTIS (6847)
email: orders@ntis.gov <http://www.ntis.gov/about/form.aspx>
Online ordering: http://www.ntis.gov

(8/2010)

IMPROVING THE PHYSICS IMPACT OF NEXT-GENERATION ^{76}GE NEUTRINOLESS DOUBLE-BETA DECAY EXPERIMENTS

By

Todd William Henry Hossbach

Bachelor of Science
University of Evansville 1997
Master of Science
University of South Carolina 2005

Submitted in Partial Fulfillment of the Requirements

for the Degree of Doctor of Philosophy in

Physics and Astronomy

College of Arts and Sciences

University of South Carolina

2009

Accepted by:

Frank T. Avignone III, Major Professor

Richard J. Creswick, Committee Member

Jeffrey R. Wilson, Committee Member

Harry S. Miley, External Examiner

James Buggy, Interim Dean of the Graduate School

DEDICATION

To my parents, Wayne and Carol Hossbach, for their many years of love, support, and encouragement.

ACKNOWLEDGMENTS

I must begin by thanking the scientists, staff, and management of the Pacific Northwest National Laboratory. I have worked with fantastic people and been given many unique opportunities over the years for which I am extremely grateful.

I'd like to express my sincere gratitude to Dr. Craig E. Aalseth and Dr. Harry S. Miley for many years of encouragement and patient guidance of a very stubborn graduate student.

Most importantly, I would like to thank Dr. Frank T Avignone, III. Its hard to find the words to adequately express my gratitude for his many years of generous support and mentoring. Frank is the kind of advisor most students want, but few are lucky enough to find. I feel extremely fortunate to be one of the few.

ABSTRACT

Next-generation ^{76}Ge neutrinoless double-beta decay experiments will require an unprecedented ultra-low level of radioactive background. The cryostat, shielding materials, and front-end electronics are a significant source of background. Efforts to improve materials purity are ongoing and analysis techniques are under development to mitigate the few expected remaining backgrounds. Two of these techniques – detector segmentation and pulse-shape discrimination – have been implemented for a prototype physically-segmented p-type germanium detector (PSEG) to experimentally quantify background rejection efficacy. The result of applying both cuts is a 90% improvement in the predicted $T^{0\nu}_{1/2}$discovery sensitivity for a PSEG-based next-generation experiment. When considering the practical reality of having to electronically instrument each additional segment, the increased experimental background results in a 19% reduction in the $T^{0\nu}_{1/2}$discovery sensitivity for a PSEG-based next-generation experiment. In comparison, using the published background rejection efficacy for a new type of unsegmented germanium detector (p-type point contact – PPC) resulted in a 168% improvement in the predicted $T^{0\nu}_{1/2}$discovery sensitivity for a PPC-based next-generation experiment. The two active ^{76}Ge neutrinoless double-beta decay collaborations – MAJORANA and GERDA – are planning to field some or all segmented germanium detectors. In light of the research presented in this document, these collaborations must consider that the added background associated with segmentation can quickly negate any

benefit gained and even reduce the sensitivity of a next-generation ^{76}Ge neutrinoless double-beta decay experiment.

Contents

List of Tables

List of Figures

CHAPTER 1

INTRODUCTION

The late nineteenth and early twentieth century was a truly exciting time in Chemistry and Physics. Following Röntgen's accidental discovery of the x-ray in 1895, a rapid series of related discoveries were made. In 1896, Becquerel classified three types of emitted rays, which he determined were negative, positive, and neutral. His work continued into the 1900's, during which time one of his students, Marie Curie, first referred to this ray-emitting process as radioactivity. Becquerel along with Marie and Pierre Curie shared the 1903 Nobel Prize for their pioneering work with radioactivity. But, it was Ernest Rutherford's discovery and classification of radioactivity based upon penetrating ability – alpha-, beta-, and gamma-rays – that marked the birth of Nuclear Physics.[36]

In the 1920's, physicists were puzzled by the continuous energy spectrum of electrons emitted in beta decay. By the end of the decade, a crisis was brewing as none of the existing theories could explain this behavior. In response to the situation, Wolfgang Pauli postulated the existence of a new particle. He theorized that this light, neutral, spin-1/2 particle is emitted simultaneously with the beta-decay electron in a manner such that the sum of the energies is constant.[11] Two years later, Enrico Fermi developed the formal theory of beta decay and clearly demonstrated its agreement with experimental data.[25]

In the seventy-nine years since the existence of the neutrino was first postulated, tremendous effort has gone into elucidating the properties of these weakly-interacting particles. For nearly fifty years after Pauli's postulation

and Fermi's formal theory on beta decay, those physicists who believed neutrinos existed, also believed them to be massless. This belief was reinforced by the development of the Standard Model during the 1970's, whose core theoretical predictions were based on a massless neutrino.[11] However, evidence from neutrino oscillation experiments has proven that neutrinos are indeed massive particles, implying physics beyond the Standard Model.[28][3]

Neutrino oscillation experiments have precisely measured the difference in mass eigenstates of neutrinos that undergo a flavor change, however, they are incapable of determining the absolute neutrino-mass scale. The only known practical ways to probe the mass range suggested by these oscillation experiments are through precision tritium endpoint-energy measurement or neutrinoless double-beta decay ($0\nu\beta\beta$-decay).

Of these two techniques, $0\nu\beta\beta$-decay experiments are much more sensitive probes of the suggested neutrino mass range. Additionally, $0\nu\beta\beta$-decay is the only practical method to determine if the neutrino is its own anti-particle (Majorana) or whether they are distinct particles (Dirac). If the neutrino is Majorana in nature, this has important consequences as it would be the first evidence for lepton number non-conservation. Some of the proposed $0\nu\beta\beta$-decay experiments have additional physics reach into dark matter, neutrino astronomy, solar axion, electron lifetime, coherent neutrino scattering, and neutrino-interaction cross-section measurements.

1.1. Tritium Endpoint Energy Measurements

Of the two methods mentioned above, tritium endpoint energy measurement is the only direct search for neutrino mass. And unlike $0\nu\beta\beta$-decay experiments, it is not sensitive to the Majorana or Dirac nature of the neutrino. Tritium is used for this type of experiment because it has the second lowest endpoint energy (18.6 keV), a short half life, (12.3 yr), and because of the simple

electron shell configuration – which makes e^- plus ^{3}H interaction corrections easier to calculate.

Like all beta-decay isotopes, the decay of tritium results in the emission of an electron and an electron anti-neutrino:

$$^3\mathrm{H} \rightarrow {}^3\mathrm{He}^+ + e^- + \bar{\nu_e} \tag{1}$$

The resulting electron energy spectrum is continuous up to the endpoint energy – see Figure 1.1a. Since the neutrino is a massive particle, the actual endpoint energy of the spectrum, E, must be less than the theoretically-predicted endpoint for a massless neutrino, E_0. For the case of a massive neutrino, the energy spectrum is given by:[17]

$$\frac{dN}{dE} = C \times F(Z,E)p(E+m_ec^2)(E_0-E)\sqrt{(E_0-E)^2-m_\nu^2}\cdot\Theta(E_0-E-m_\nu) \tag{2}$$

where m_ν is the mass of the electron neutrino, m_e is the mass of the electron, $\Theta(E_0-E-m\nu)$ is a step function to guarantee energy conservation, $p(E+m_ec^2)$ is the momentum of the electron, and $F(Z,E)$ is the Fermi function. The value of C is given by:

$$C = \frac{G_F^2}{2\pi^3}\cos^2\theta_C|M|^2 \tag{3}$$

where G_F is the Fermi constant, θ_C is the Cabibbo angle, and M is the nuclear matrix element for the process. In an experiment, a slight distortion in the energy spectrum will be observed at the electron energy $E_0 - m(\nu_e)$. Where $m(\nu_e)$ is defined as:

$$m^2(\nu_e) = \sum_{k=1}^{3}|U_{ek}|^2\cdot m_k^2\ . \tag{4}$$

and U_{ek} is the neutrino mixing matrix. This energy spectrum distortion is illustrated in Figure 1.1b for an electron neutrino mass of 1 eV.

There is currently one international collaboration – KATRIN – that is actively pursuing a new tritium endpoint-energy measurement. The experiment

has been designed to measure the mass of the electron neutrino with a sensitivity of 0.2 eV. The tritium source and magnetic spectrometer have been constructed and experimental runs are about to begin.[16]

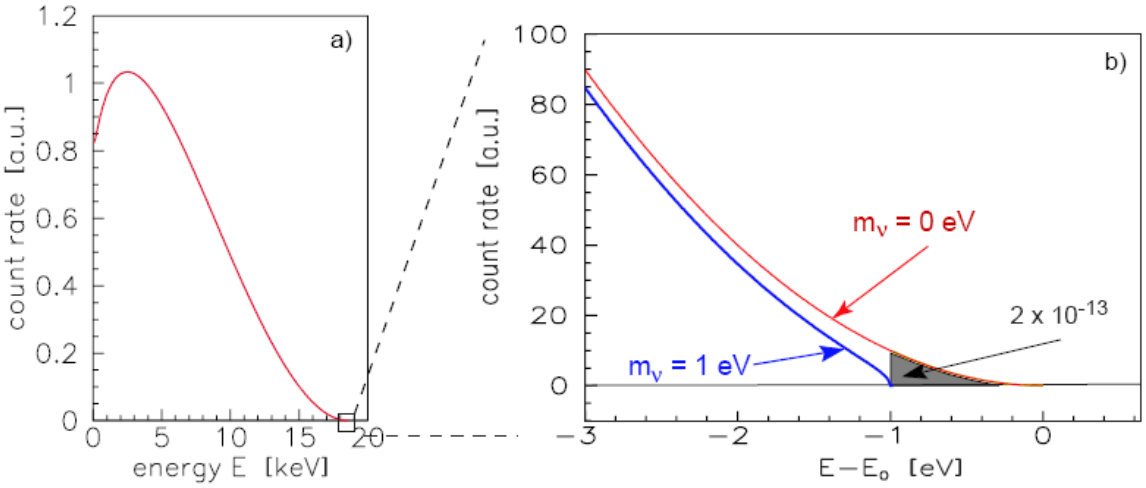

FIGURE 1.1. The electron energy spectrum of tritium β decay: complete (a) and narrow region around endpoint E_0 (b). The β spectrum is shown for neutrino masses of 0 and 1 eV. The value of 2×10^{-13} shown in (b) is the fraction of the total number of events that fall within the last 1 eV before the endpoint. Graphic taken from [17]

1.2. DOUBLE-BETA DECAY

For most even-even nuclei, ordinary beta decay is energetically forbidden. However, for some of these nuclei an energetically permissible process known as double-beta decay exists, whereby the nucleus changes atomic number by two while simultaneously emitting two beta particles.

To understand why double-beta emission is permissible while single-beta emission is forbidden, one must look at the binding energy of the nucleus, B, given by:

$$B(A,Z) = [Z(M_p + m_e) + (A-Z)M_n - M(A,Z)] \cdot c^2 \tag{5}$$

where M_p is the mass of the proton, m_e is the mass of the electron, M_n is the mass of the neutron, A is the mass number, and Z is the atomic number. The Weisäcker formula, also known as the semi-empirical mass formula (equation 6) is a parameterization of the nuclear mass, M in terms of A and Z, and is given by the phenomenological formula: [42][8][50]

$$\begin{aligned} M(A,Z) &= NM_n + ZM_p + Zm_e - a_v A + a_s A^{2/3} \\ &+ a_c \frac{Z^2}{A^{1/3}} + a_a \frac{(N-Z)^2}{4A} + \frac{\delta}{A^{1/2}} \end{aligned} \tag{6}$$

where a_v (volume), a_s (surface), a_c (Coulomb), a_a (asymmetry) , and δ (pairing) are constants whose exact values depend on the mass range of interest. For the current discussion, only the pairing term is of interest. For odd-odd nuclei, δ is positive. For odd-even nuclei, δ is zero. And for even-even nuclei, δ is negative. Therefore in the case of double-beta decay candidate nuclei, $M(even, even) < M(even, odd)$ and thus $B(even, even) > B(even, odd)$. For A=76, the mass parabola in Figure 1.2 shows the effect of a more strongly bound even-even nucleus.

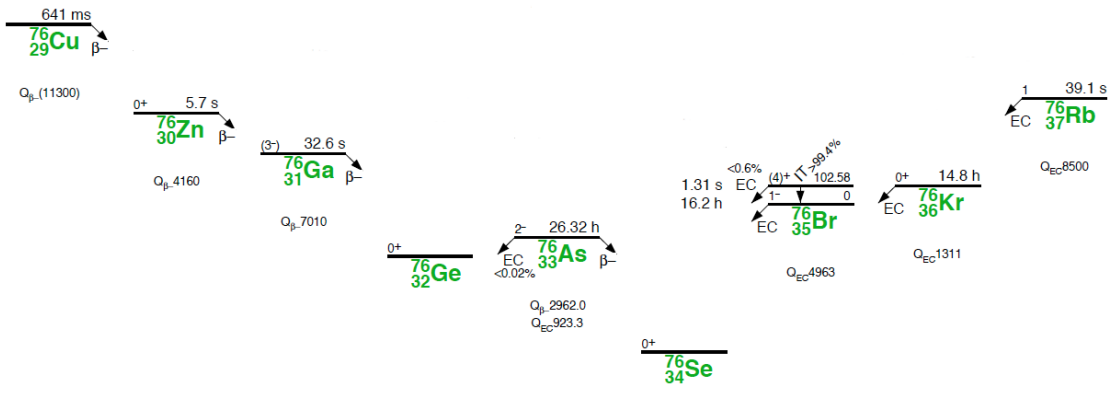

FIGURE 1.2. Mass parabola for A=76. [27]

1.2.1. Double-Beta Decay Modes. The two modes of double-beta decay most frequently studied are referred to as two-neutrino (2ν) and zero-neutrino (0ν). In the 2ν mode, two neutrinos are emitted simultaneously with two beta-decay electrons, resulting in a continuous energy spectrum similar to ordinary beta decay. In the 0ν mode, the two beta-decay electrons are emitted without accompanying neutrinos, and the electrons practically share the entire decay energy. This mode results in a monoenergetic line in the energy spectrum at the $Q_{\beta\beta}$ of the isotope. These two modes are illustrated in Figure 1.3 and a list of eleven double-beta decay candidate isotopes is compiled in Table 1.1.[9] With either mode, it is possible for the decay to proceed through excited states in the Z+2 daughter nuclei. Details of these excited state transitions will not be discussed in this work. However, there are extremely exciting research opportunities since unique gamma-ray energies can be measured along with the electrons. [5][6][48]

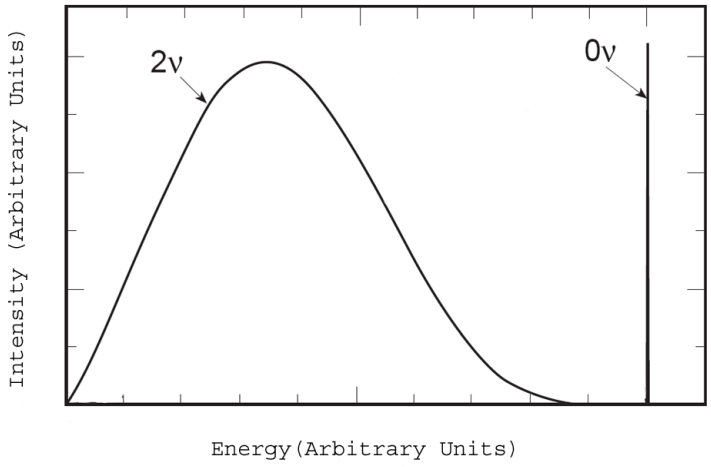

FIGURE 1.3. This plot shows the difference in the energy spectra of the two double-beta decay modes.

1.2.2. Neutrino Mass from 0ν Double-Beta Decay. While techniques will vary, the goal of a double-beta decay experiment is to measure the decay and thus the half life of the candidate isotope. For the $2\nu\beta\beta$-decay mode, the half-life has been measured in eleven isotopes – refer to Table 1.2. The theoretically-predicted $2\nu\beta\beta$-decay half-life is given by,

$$[T^{2\nu}_{1/2}]^{-1} = G_{2\nu}(Q_{\beta\beta}, Z)|M_{2\nu}|^2 \,, \tag{7}$$

where $G_{2\nu}(Q_{\beta\beta}, Z)$ is the four-particle phase space factor, and $M_{2\nu}$ is the nuclear matrix element for this process. The decay rate for this process does not depend on the masses of the neutrinos. However, accurate measurement helps to validate the models used to calculate the nuclear matrix elements.

Of more fundamental importance is the measurement of $0\nu\beta\beta$-decay since the rate is mediated by the neutrino mass. The theoretically-predicted rate is given by,

$$[T^{0\nu}_{1/2}]^{-1} = G_{0\nu}(Q_{\beta\beta}, Z)|M_{0\nu}|^2\langle m_{\beta\beta}\rangle^2 \,, \tag{8}$$

where $G_{0\nu}(Q_{\beta\beta}, Z)$ is the phase space factor for the emission of the two electrons, $M_{0\nu}$ is the 0ν nuclear matrix element, and $\langle m_{\beta\beta}\rangle$ is the effective Majorana mass of the electron neutrino given by,

$$\langle m_{\beta\beta}\rangle \equiv |\sum_k m_k U^2_{ek}| \tag{9}$$

$$\langle m_{\beta\beta}\rangle = \left|m_1|U_{e1}|^2 + m_2|U_{e2}|^2 e^{i(\alpha_2-\alpha_1)} + m_3|U_{e3}|^2 e^{i(-\alpha_1-2\delta)}\right| \tag{10}$$

where U_{ek} is the neutrino mixing matrix that turns well-defined mass eigenstates into well-defined flavor eigenstates. The imaginary terms describe the Majorana (α_1 and α_2) and Dirac (δ) phases, and can be neglected if one chooses to neglect CP violation.[5]

To extract the effective neutrino mass from the experimental measurement one begins with equation 8 and with simple rearrangement obtains,

$$\langle m_{\beta\beta}\rangle = [T^{0\nu}_{1/2} G_{0\nu}(Q_{\beta\beta}, Z)|M_{0\nu}|^2]^{-1/2} \ . \tag{11}$$

Multiplying both sides by the electron mass yields,

$$\langle m_{\beta\beta}\rangle = m_e[T^{0\nu}_{1/2} G_{0\nu}(Q_{\beta\beta}, Z)|M_{0\nu}|^2 m_e^2]^{-1/2} \ . \tag{12}$$

Combining all of the nuclear model-dependent parameters into the nuclear structure function, F_N,

$$F_N = G_{0\nu}(Q_{\beta\beta}, Z)|M_{0\nu}|^2 m_e^2 \tag{13}$$

one obtains the compact form,

$$\langle m_{\beta\beta}\rangle = m_e[T^{0\nu}_{1/2} F_N]^{-1/2} \ . \tag{14}$$

The discovery sensitivity of a next-generation experiment is given by the analytical expression, [4]

$$T^{0\nu}_{1/2}(n_\sigma) = \frac{4.16 \times 10^{26} y}{n_\sigma} \left(\frac{\varepsilon a}{W}\right) \sqrt{\frac{Mt}{b\Delta(E)}} \ , \tag{15}$$

where n_σ is the desired standard deviation of the measurement, ϵ is the event-detection efficiency, a is the isotopic abundance in the source material, W is the molecular weight of the source material, M is the total mass of the source, b is the background rate in counts/(keV kg y), and ΔE is the spectral resolution of the experiment. To determine the mass sensitivity of a next-generation $0\nu\beta\beta$-decay experiment, one need only substitute equation 15 into equation 14.

This very brief experimentally-motivated theoretical discussion would not be complete without addressing an important outstanding issue. While $T^{0\nu}_{1/2}$can be precisely measured in a carefully conducted experiment, the calculation of

the effective neutrino mass – equation 14 – is not as certain. This uncertainty results from the uncertainty in the calculation of the nuclear matrix element, $M_{0\nu}$. Over the past several years, the values of the nuclear structure function have changed substantially for all of the candidate isotopes. This was largely the result of the increased focus on double-beta decay after the neutrino oscillation experiments verified a massive neutrino. The models that have been used in the calculations have and will continue to improve.

TABLE 1.1. Candidate double-beta decay isotopes, their theoretical end-point energy, and the best reported limits for $T^{0\nu}_{1/2}$.[5]

$\beta\beta$-Decay Candidates	$Q_{\beta\beta}$ (keV)	$T^{0\nu}_{1/2}$ (yrs)	$\langle m_{\beta\beta}\rangle$ (eV)
^{48}Ca	4271	$> 1.4 \times 10^{22}$	<7.2-44.7
^{76}Ge	2039	$> 1.9 \times 10^{25}$	< 0.35
^{76}Ge	2039	$(2.23^{+0.44}_{-0.31}) \times 10^{25}$	0.32 ± 0.03
^{76}Ge	2039	$> 1.57 \times 10^{25}$	$< (0.33 - 1.35)$
^{82}Se	2995	$> 2.1 \times 10^{23}$	<(1.2-3.2)
^{100}Mo	3034	$> 5.8 \times 10^{23}$	<(0.6-2.7)
^{116}Cd	2802	$> 1.7 \times 10^{23}$	<1.7
^{128}Te	868	$> 7.7 \times 10^{24}$	<(1.1-1.5)
^{130}Te	2527	$> 3.0 \times 10^{24}$	<(0.41-0.98)
^{136}Xe	2479	$> 4.5 \times 10^{23}$	<(0.8-5.6)
^{150}Nd	3367	$> 3.6 \times 10^{21}$	

1.3. SUMMARY

Tremendous excitement exists in the neutrino physics community today. Solar and atmospheric neutrino oscillation experiments have precisely measured the differences in the mass eigenstates and thus proven the existence of a massive neutrino. Many outstanding questions regarding the nature of the neutrino still remain – what is the absolute mass scale of the neutrino, what is the neutrino mass hierarchy ($m_3^2 < m_1^2$ (inverted) or $m_3^2 > m_2^2$ (normal)), is the neutrino a Majorana or Dirac particle? It is the goal of next-generation

TABLE 1.2. A list of double-beta decay isotopes and the experimentally determined $T^{2\nu}_{1/2}$values. [5]

Isotope	$T^{2\nu}_{1/2}$ (years)
^{48}Ca	$(4.2^{+2.1}_{-1.0}) \times 10^{19}$
^{76}Ge	$(1.5 \pm 0.1) \times 10^{21}$
^{82}Se	$(0.92 \pm 0.07) \times 10^{20}$
^{96}Zr	$(2.0 \pm 0.3) \times 10^{19}$
^{100}Mo	$(7.1 \pm 0.4) \times 10^{18}$
^{116}Cd	$(3.0 \pm 0.2) \times 10^{19}$
^{128}Te	$(2.5 \pm 0.3) \times 10^{24}$
^{130}Ba 2ν	$(2.2 \pm 0.5) \times 10^{21}$
^{130}Te	$(0.9 \pm 0.1) \times 10^{21}$
^{150}Nd	$(7.8 \pm 0.7) \times 10^{18}$
^{238}U	$(2.0 \pm 0.6) \times 10^{21}$

$0\nu\beta\beta$-decay experiments to find these answers. In the following chapters the details of the development of a new type of germanium detector proposed for ^{76}Ge $0\nu\beta\beta$-decay are presented. Advanced analysis techniques have been implemented with this prototype detector to improve the neutrino mass sensitivity of planned next-generation experiments. The efficacy of these techniques is quantified and discussed. New experimental evidence is presented that should be seriously considered when choosing the type of germanium detector for next-generation $0\nu\beta\beta$-decay experiments.

CHAPTER 2

EXPERIMENTALLY MEASURING NEUTRINOLESS DOUBLE-BETA DECAY

Next-generation neutrinoless double-beta decay experiments will employ a variety of measurement techniques based upon the candidate isotope. For ^{76}Ge $0\nu\beta\beta$-decay, the favored technique is to use HPGe detectors that have been enriched to 86% in ^{76}Ge. First suggested by Ettore Fiorini, this source-in-detector technique yields dramatically higher detection efficiency.[26] Currently, there are two collaborations working toward a next-generation experiment – GERDA and MAJORANA. GERDA is a funded effort to operate $\sim$35 kg of segmented germanium detectors by direct immersion in liquid argon.[14] MAJORANA is a proposed experiment consisting of $\sim$60 kg of germanium detectors using conventional cryostat cooling techniques.[20][18] Both of these collaborations are currently working to resolve technological issues related to achieving a 1 ton scale ^{76}Ge $0\nu\beta\beta$-decay experiment. On the surface, these two experiments have only a candidate isotope in common. To some degree that is true, but the research detailed in this document pertains equally to both experiments since the underlying technology – germanium detectors – and major issues – backgrounds – remain the same.

2.1. BACKGROUNDS AND SIGNALS IN GERMANIUM DETECTORS

The difficulty inherent to all neutrinoless double-beta decay experiments is the extremely low-background levels required to reach the needed sensitivity. These low-background levels are driven by the extremely long half-lives

of the candidate isotopes. Fortunately, most backgrounds can be mitigated in carefully constructed experiments.

For germanium-based experiments, the remaining backgrounds fall into one of two categories – primordial contamination and cosmogenically produced. Primordial contamination, consisting of the ^{238}U and ^{232}Th decay chains and Bremsstrahlung radiation from the ^{210}Pb daughter ^{210}Bi, is found in the cryostat, internal electronics components, and shielding materials. Cosmogenically produced backgrounds are found in the germanium crystal (^{54}Mn, ^{57,58}Co, ^{65}Zn, ^{68}Ge) and in copper used in the cryostat and for shielding (^{54}Mn, ^{56,57,58,60}Co, ^{59}Fe).

These background sources are problematic because they decay by emitting a positron or gamma ray(s) that are above the $Q_{\beta\beta}$ for ^{76}Ge (2039.006 keV [23]) and could easily contaminate the $0\nu\beta\beta$-decay region of interest (ROI). Differentiating between these backgrounds and the $0\nu\beta\beta$-decay signal is a necessary objective.

The electrons emitted in a double-beta decay event have a short mean-free path length in germanium – on the order of 1 mm. This means that the electron-hole pairs created in the germanium crystal by each double-beta decay electron are indistinguishable. Analysis of the current pulse from the detector would lead one to believe that a single electron-hole cloud was produced in this event. This type of event is referred to as a single-site event.

For the background sources listed above, historical evidence and simulations have shown that these backgrounds tend to deposit energy at multiple locations within the germanium crystal through Compton scattering or positron annihilation.[29][1] Analysis of the current pulse from the detector would distinctively show the arrival of different electron-hole clouds. Events that deposit energy at multiple-locations within the crystal are thus referred to as multi-site events.

Differentiating between the double-beta decay signal and the background is then a matter of determining the multiplicity of the event. In Figures 2.1 to 2.8, several graphical examples are given for the different types of energy-depositing interactions that can occur in a detector.

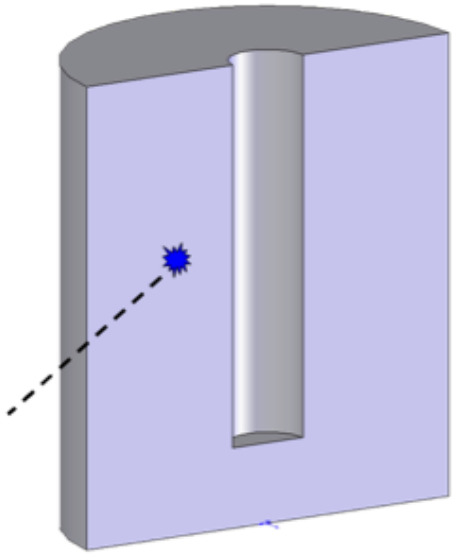

FIGURE 2.1. Background external to the germanium crystal. All of the energy is deposited at a single location in the crystal – single-site event.

2.2. ANALYSIS TECHNIQUES FOR BACKGROUND REMEDIATION

Using ultra-low background materials and implementing special handling techniques reduces a majority of experimental backgrounds. Unfortunately, a level is reached where it is no longer practical or feasible to remove the remaining backgrounds. In addition to a basic energy cut, analysis techniques are being developed to mitigate the effects of trace radioactive impurities, by taking advantage of the large number of germanium crystals, high-bandwidth electronics, and the excellent energy resolution of germanium. Taken together, the effect of all the analysis-based mitigation techniques is a predicted reduction in the remaining background of up to 90%.[20]

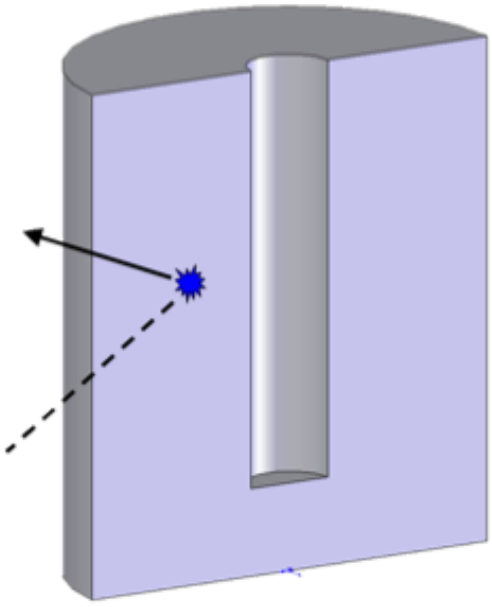

FIGURE 2.2. Background external to the germanium crystal. Energy is deposited at a single location and then scatters out of the crystal – single-site event.

2.2.1. Granularity. The term granularity refers to detector-to-detector coincidence background rejection. In a large array of densely packed detectors, the close placement of germanium crystals allows one to veto events where signals are simultaneously generated in more than one detector. These events include external gamma rays that hit one detector, and Compton scatter into an adjacent detector (see Figures 2.2 and 2.4), or internally generated gamma rays that escape the crystal (see Figures 2.6 and 2.8). External backgrounds such as ^{208}Tl and ^{214}Bi from the ^{232}Th decay chain and^{60}Co have decay schemes well suited to granularity cuts. As an example, assume that an external ^{208}Tl gamma ray (2615 keV) hits a crystal and deposits 2039 keV of energy at a single site inside the crystal. There is a high probability that the escaping gamma would hit one of the surrounding detectors depositing the remaining 576 keV. With an expected count rate for MAJORANA of 1 count per day per crystal any

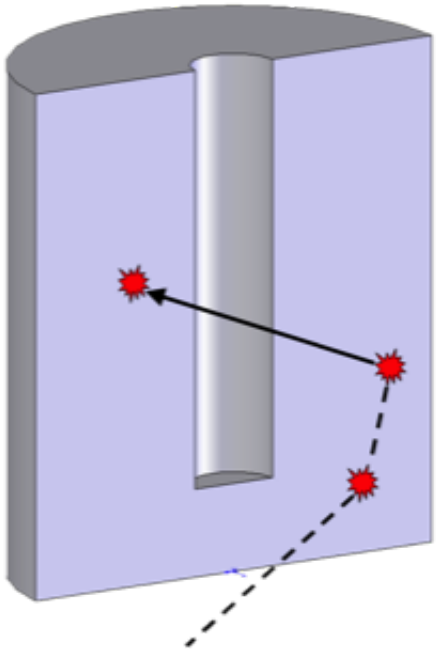

FIGURE 2.3. Background external to the germanium crystal. All of the energy is deposited at multiple locations within the crystal – multi-site event.

two-detector events within a time window of 1 μs could be vetoed with negligible effect on the system live-time.[20]

2.2.2. Single-Site Time Correlation. Single-Site Time Correlation is a decay-chain specific cut that looks forward or backward in time from an event in the $Q_{\beta\beta}$ ROI (2039 keV) to find signatures of parent or daughter isotopes. For an event rate of $\sim$1 event per day per detector this cut will work exceptionally well for internal short-lived parent/daughter nuclei like ^{68}Ge/^{68}Ga and for other backgrounds, such as ^{208}Tl and ^{214}Bi, with a somewhat lower rejection efficiency.[19][20]

Using internal ^{68}Ge contamination as an example, the efficacy of the single-site time correlation cut can be explored. The decay of ^{68}Ge via electron capture releases a series of soft x-rays. Within a few half-lives of the daughter, ^{68}Ga, a positron of end-point energy 2.9 MeV should be detected. Looking backward

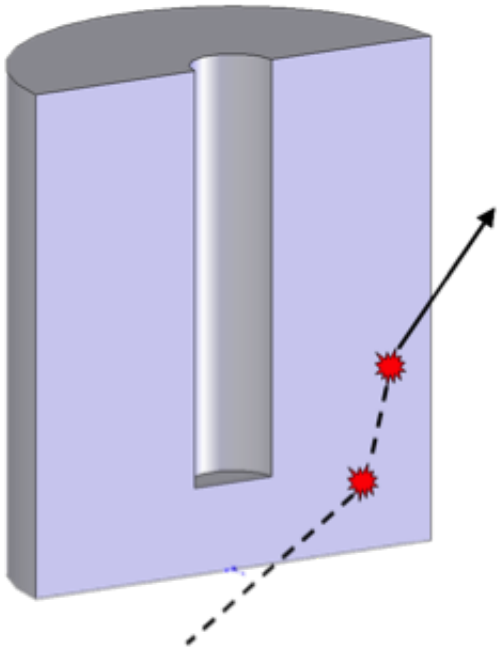

FIGURE 2.4. Background external to the germanium crystal. Energy is deposited at multiple locations and then scatters out of the crystal – multi-site event.

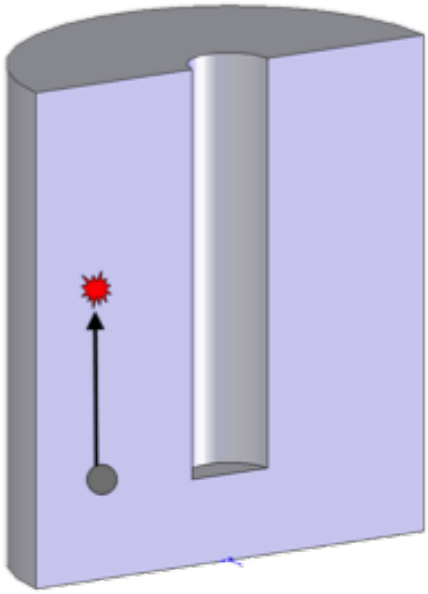

FIGURE 2.5. Background internal to the germanium crystal. All of the energy is deposited at a single location in the crystal – single-site event.

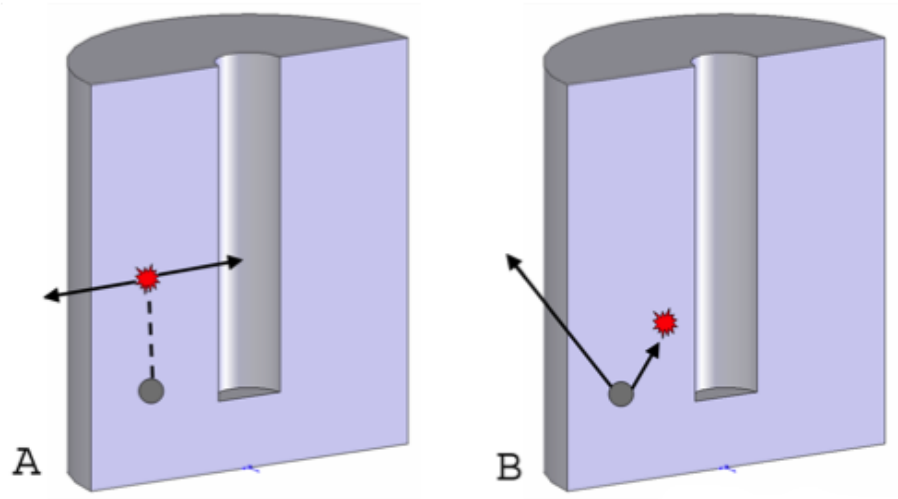

FIGURE 2.6. Background internal to the germanium crystal. Part of the total energy is deposited at a single location in the crystal – single-site event. The remaining decay energy escapes the crystal. A.) Corresponds to internal ^{68}Ge. B.) Corresponds to internal ^{60}Co.

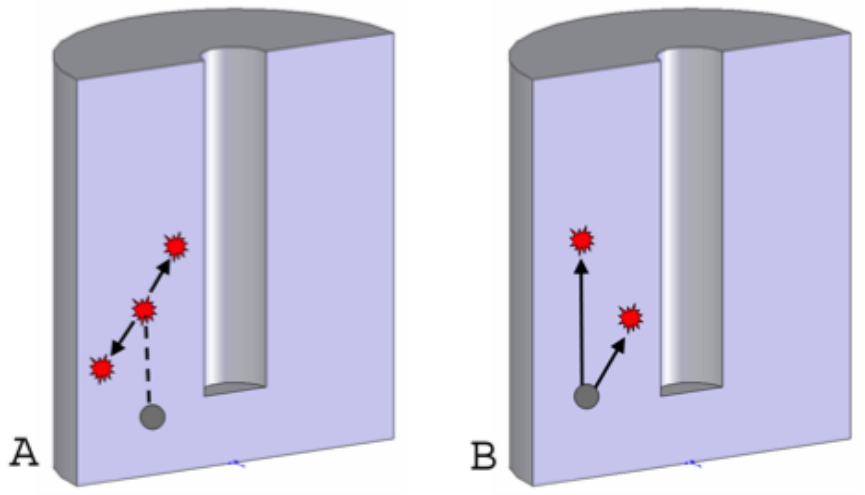

FIGURE 2.7. Background internal to the germanium crystal. All of the decay energy is deposited at multiple locations in the crystal – multi-site event. A.) Corresponds to internal ^{68}Ge. B.) Corresponds to internal ^{60}Co.

in time from the positron event, the decay of ^{68}Ge should be seen, providing a time-correlated cut for events that may have passed the other analysis cuts. The number of half-lives that can be used to find the precursor signal are limited by the count rate of that detector. One must be careful in looking back

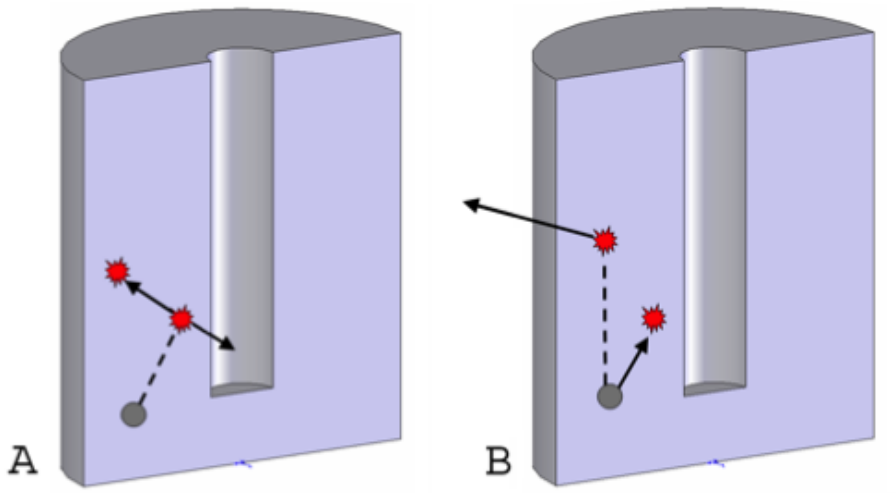

FIGURE 2.8. Background internal to the germanium crystal. Part of the total energy is deposited at multiple locations in the crystal – multi-site event. The remaining decay energy escapes the crystal. A.) Corresponds to internal ^{68}Ge. B.) Corresponds to internal ^{60}Co.

through too many half-lives because the probability of catching a random event increases for each half-life that is included in the cut. Figure 2.9 illustrates the effect of the single-site time correlation cut on internal ^{68}Ge contamination.

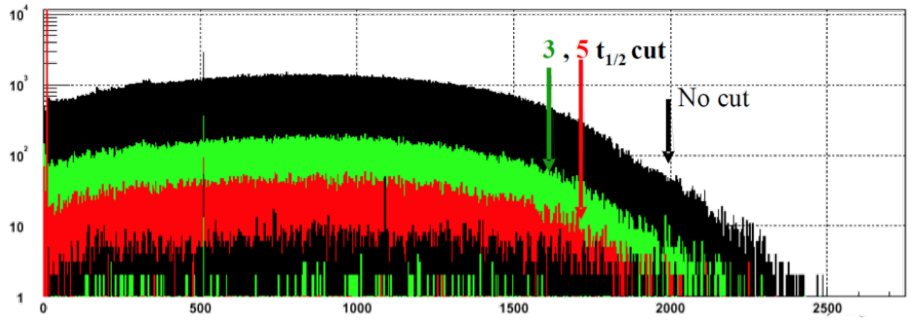

FIGURE 2.9. Effect of applying the Single-Site Time Correlation cut to simulated internal ^{68}Ge contamination looking back 3 (green) and 5 (red) half lives, with rejection factors 8 and 32 respectively.[20]

2.2.3. Detector Segmentation. Segmentation uses the electrical isolation of the detector contacts to effectively create sub-volume elements within a single germanium crystal. Similar to the granularity cut, one is able to veto

those events that occur in more than one segment. Highly-segmented germanium detectors have demonstrated, utilizing advanced pulse-shape analysis, gamma-ray-interaction position resolution of $\sim$1 mm.[15] The downside to this degree of segmentation is not only in the added monetary expense to the experiment, but more so in the added background from each additional electronically-instrumented segment. The segmentation cut works well for both internal and external multi-site events. Referring to Figures 2.3, 2.4, 2.7, and 2.8, one could imagine how detector with active subvolumes would be able to differentiate multi-site events from single-site events. A more detailed discussion of detector segmentation can be found in chapter 3.

2.2.4. Pulse-Shape Discrimination (PSD). Pulse-shape discrimination uses the unique features in the shape of the evolved current pulse to determine the number of unique energy deposition locations within a crystal for a given event. Regardless of whether an event is multi-site or single-site, each electron or hole cloud created by a radiation event will drift towards its respective contact with a velocity proportional to the electric field. A majority of the time, the electron and hole clouds will arrive at their respective contacts at different times. This time difference, coupled to the amount of charge measured by the electronics can crudely determine the event location within the crystal. If multiple electron-hole clouds reach the contact in a short time window ($<1\mu$s), the event is considered multi-site and vetoed. This principle is illustrated in Figure 2.10. Again, referring to Figures 2.3, 2.4, 2.7, and 2.8, one could imagine how the arrival of multiple electron-hole clouds could be determined by analyzing the current pulse. A more detailed description of the pulse shape analysis technique used in this research can be found in section 5.2.

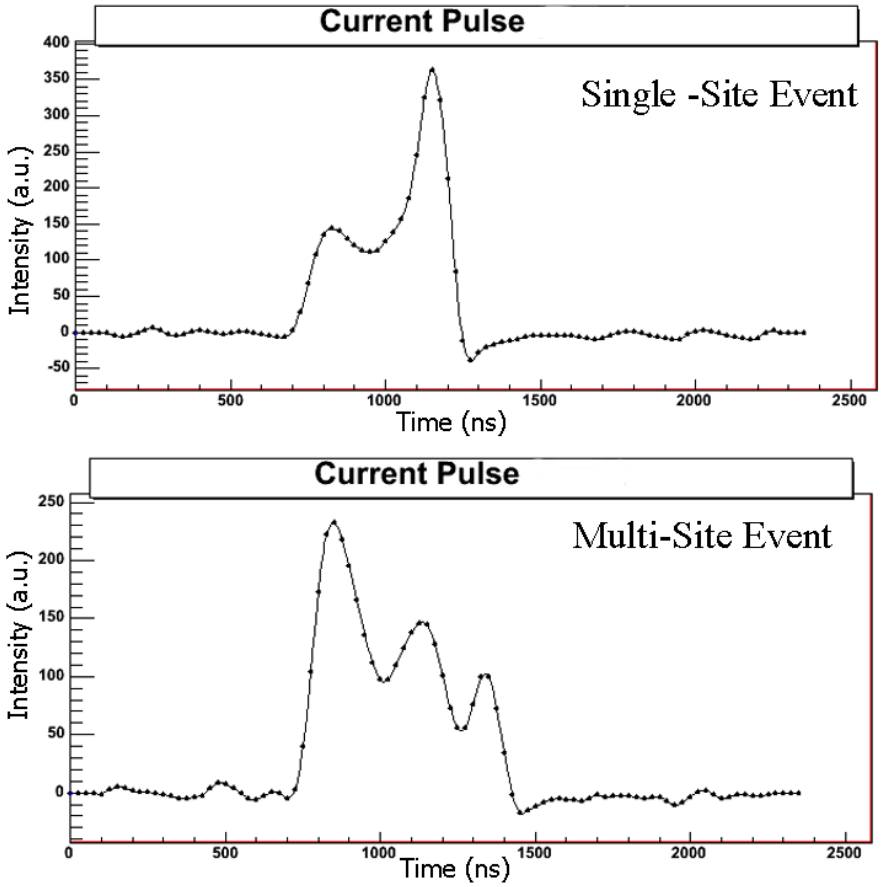

FIGURE 2.10. This figure shows two example current pulses from a commercial germanium detector. The top graph represents a typical single-site energy deposition. As the electrons and holes drift toward the contacts, they arrive at different times. Based upon the shape of the pulse (size of the measured charge and time of collection), this event occurred near the outside radius of the crystal. The bottom graph represents a typical multi-site energy deposition with at least three distinct arrivals of charge.

2.2.5. Quantifying Remediation Efficacy. To quantify the efficacy of the analysis cuts a figure of merit (FOM) can be defined. This FOM is a multiplicative factor on $T^{0\nu}_{1/2}$(equation 15) and thus directly yields the sensitivity improvement one might expect to obtain by implementing the analysis cuts. This figure of merit is defined as:

$$FOM = \frac{\epsilon_{\beta\beta}}{\sqrt{\epsilon_{\text{background}}}} \tag{16}$$

where $\epsilon_{\beta\beta}$ and $\epsilon_{\text{background}}$ are the post-cut acceptance fractions, for $0\nu\beta\beta$-decay events and background events, respectively. To test the efficacy of the cuts just described, it is necessary to find a substitute for the $0\nu\beta\beta$-decay signal. A single-site surrogate can be obtained from double-escape peak (DEP) events. When a high-energy gamma ray enters the detector and produces an electron-positron pair, the positron immediately annihilates with an electron in the lattice, producing back-to-back 511 keV gammas. Since the germanium detector is finite in size, either one or both the gammas can escape the crystal. If both gammas escape (double-escape) then the energy of the event will appear to have been deposited at a single location within the detector – similar to the $0\nu\beta\beta$-decay signature.

For a germanium-based experiment, the figure of merit can vary substantially based on the design of the experiment – degree of segmentation, electronic bandwidth, background level, etc. An example based on segmentation might help illustrate this variability.

Consider the calculated figures of merit in Table 2.1. These values were calculated using equation 16 from a EGS4-based Monte Carlo simulation of various internal and external – to the crystal – background sources. The simulations recorded energy deposition location such that arbitrary segmentation schemes could be applied to the same data set. To avoid any possible geometric bias, each individual element for a given segmentation scheme is equal-volume. It is clear from this tabulated data that "more is better" when it comes to segmentation. This of course disregards many other real-world experimental factors that must be considered.

A final note regarding the use of this FOM for multiple analysis cuts. In attempting to determine the overall efficacy of background removal, one can not simply add the FOMs for each analysis cut in order to obtain the overall FOM for the experiment. Some of the analysis cuts – such as segmentation

TABLE 2.1. Table summarizing the calculated figures-of-merit (FOM) from simulated data for various segmentation schemes and background sources. Z is the number of axial segments and ϕ is the number of azimuthal segments.

No of Segs		Figure of Merit (FOM)			
ϕ	Z	^{60}Co Int	^{60}Co Ext	^{68}Ge Int	^{208}Tl Ext
1	1	3.121	2.520	1.808	1.958
1	2	4.081	3.295	2.158	2.148
1	3	4.875	3.946	2.474	2.262
1	4	5.247	4.600	2.792	2.365
1	5	6.733	5.103	2.932	2.410
1	6	6.821	5.467	3.130	2.518
1	7	7.720	5.638	3.263	2.474
1	8	7.763	6.785	3.372	2.500
1	9	8.600	6.871	3.744	2.605
1	10	11.525	7.531	4.027	2.589
2	2	5.481	4.268	2.658	2.319
4	4	8.075	6.638	3.656	2.542
6	6	10.979	9.303	4.202	2.643
8	8	12.998	9.393	4.855	2.666
10	10	15.992	10.394	5.430	2.653

and PSD – will almost certainly overlap in the events that are cut. If this fact is neglected then the overall predicted background-reduction efficacy of the cuts will be overestimated resulting in an unrealistic predicted-sensitivity enhancement for the experiment. More details on this topic are presented in chapter 5.

2.3. SUMMARY

Determining the validity of the simulation-based FOMs in Table 2.1 is extremely important. In the next chapter, the details of the development of a new type of segmented detector will be presented. This unique detector is an ideal tool for determining the true FOMs for segmentation and PSD along with the orthogonality of these cuts.

CHAPTER 3

A NEW TYPE OF SEGMENTED GERMANIUM DETECTOR FOR ^{76}GE DOUBLE-BETA DECAY

Spurred by the technological achievements of World War II, a considerable effort was dedicated to investigating new materials for radiation detection – specifically, direct charge collection with insulating single crystals such as diamond and alkali halides. Initial research into germanium as a radiation detector occurred in 1949 under the direction of Kenneth McKay of Bell Laboratories. Unlike most of the materials being investigated at the time, McKay found that charge-trapping and recombination were absent in his reverse-biased germanium diode structure. Unfortunately, McKay's detector suffered from poor counting geometry. Coupled with the poor charge-collection performance of other materials being investigated at the time, germanium as a radiation detector was largely overlooked until the late 1950's and early 1960's.[38][39]

From the early 1960's and continuing to this day, germanium-based radiation detectors have continued to evolve. Because of their superior energy resolution and ability to be manufactured in volumes exceeding 800 mL (4.4 kg) [45], modern germanium detectors are the standard tool for gamma-ray spectroscopy. Arguably, the most significant advancement in the last two decades has been the development of segmented germanium detectors. Segmentation effectively creates individual active-volume elements within a single germanium crystal and is achieved by electrically isolating (segmenting) the surface contacts through photolithography, masking, etching, or physical grooving.[49] Originally conceived as an alternative to the large arrays of small germanium

detectors utilized in medical imaging, segmented germanium detectors are currently utilized in many aspects of nuclear physics including gamma-ray tracking, gamma-ray imaging, and Compton imaging.[49] Before continuing with the details of the development of a new type of segmented germanium detector, it may be helpful to discuss the history and motivation behind this research.

3.1. Early Segmented Detector Development

When segmentation was first investigated, both p-type and n-type germanium crystals were used to fabricate detectors. The initial work with p-type crystals involved the masking of the outer contact prior to the application of the n-type lithium contact.[46] This work was met with limited success because subsequent warming and detector reconditioning (bake and pump) allowed the lithium to migrate on the outer surface thus destroying the electrical isolation of the contacts. Similarly, for n-type crystals, the outer surface of the detector was masked prior to the ion-implantation of boron to make the p-n junction. Since boron does not migrate with the application of heat, n-type segmented detectors were more tolerant to warming and multiple bake-and-pump cycles. Because of this robustness to reconditioning and the relative ease of masking the p-type contact, all commercially available segmented detectors are bulk n-type. There are, however, disadvantages to n-type detectors when considering their use in a large-scale ^{76}Ge neutrinoless double-beta decay experiment.

When a germanium crystal is grown, there is no a priori knowledge whether the final crystal will be n-type or p-type. In practice, a majority of crystals tend to be p-type. In a large scale $0\nu\beta\beta$-decay experiment consisting of hundreds of detectors, requiring the use of only n-type crystals results in a slow detector production rate since every p-type crystal must be returned to the crystal melt for regrowth. In addition to the significant added expense, increased exposure time above ground results in increased cosmic-ray muon produced backgrounds

in the germanium.[24] Crystal regrowth removes most of these cosmogenic contaminants, however, the ^{68}Ge concentration will continue to increase as long as the germanium material remains above ground. If segmented detectors are to be used in a large-scale experiment, the use of both n-type and p-type germanium crystals is highly desirable in order to keep cost and internal cosmogenic backgrounds as low as possible.

A second downside to using n-type segmented detectors is the limited vendor choice – currently only one manufacturer. This has the potential of devastating consequences to a large-scale experiment should a problem arise with the manufacturing facility or process. Relying upon a single manufacturer presents a very high risk to the success of the project. Because manufacturers are not likely to share fabrication technology or trade secrets, it would be highly desirable to find a solution that would allow other manufacturers to fabricate segmented detectors using non-proprietary methods.

While low detector yield and limited vendor choice are significant issues, arguably the most significant downside to using n-type segmented germanium detectors is the extreme care that must be exercised in handling a finished detector. The outer p-type contact is extremely thin - a few microns thick - and even the most delicate touch on the outer surface can have devastating consequences ranging from high surface leakage to destroyed segmentation. By contrast, p-type detectors are much more tolerant to handling since the outer lithium-diffused dead layer is 100 or more microns in depth. The question then becomes, how does one manufacture a p-type segmented germanium detector that will withstand thermal cycling and detector reconditioning. One solution is to apply amorphous germanium to the outer surface in the desired contact geometry. This type of segmentation has been demonstrated with success. However, the amorphous contacts are sensitive and require special handling similar to that of n-type detectors.[32] Another segmentation solution is

to physically cut grooves into the surface of the detector to form the desired contact geometry. In 2004, as part of the research efforts associated with the proposed MAJORANA experiment, Dr. Frank T. Avignone III of the University of South Carolina proposed a research project to investigate the feasibility of a physically segmented p-type semi-coaxial HPGe detector for a sensitive search for ^{76}Ge neutrinoless double-beta decay.

3.2. DETECTOR DESIGN

After extensive simulations and in consultation with the MAJORANA Collaboration, the segmentation scheme of the detector was chosen to illustrate the background rejection efficacy of detector segmentation in conjunction with pulse-shape discrimination (PSD). In general, the PSD method will function as a radial-event discriminator since it uses the time of arrival of electrons and holes as the basis of discrimination. Of the other two coordinates, z and ϕ, simulation results along with practicality and difficulty of physical segmentation dictated z-segmentation – also referred to as axial segmentation.

To prove that cutting grooves into the surface of a p-type crystal provided a viable segmentation option, a proof-of-concept detector was fabricated. Using a freshly-refurbished p-type HPGe crystal of approximately 40% relative efficiency, a deep circumferential groove was cut into the detector approximately 1 cm from the closed end. Since the diffusion depth of the lithium was not accurately know, the cut was made deep enough such that penetration of the dead layer was guaranteed. The location and depth of the cut can be seen in the photo in Figure 3.1. After the groove was cut, the crystal was reprocessed and the newly-cut groove was chemically treated to form a surface of high resistance. This process is identical to the process used to separate the n- and p-type crystal contacts. By creating the high resistance surface, the outer electrical contact is separated and electrically isolated. Tests using a low-energy

monoenergetic gamma-ray source demonstrated that electrical segmentation of the detector was achieved.

FIGURE 3.1. Photograph of the first USC p-type segmented germanium detector. The purpose of this detector was to demonstrate the feasibility of segmenting p-type detectors by cutting through the dead layer. This photograph shows the location and depth of the cut.

With the success of the proof-of-concept detector, a larger p-type crystal of 70% relative efficiency was procured from Canberra Industries and fabricated into a detector at Princeton Gamma Tech (PGT). The crystal has dimensions of 70.5 mm in length and 63.2 mm in diameter with a Li-diffused deadlayer thickness of $\sim$0.5 mm. After confirming that the detector was performing within manufacturer specifications, it was sent to Reeves and Sons, LLC for groove machining. The details of the groove-machining process can be found in reference [33]. A total of four $\sim$0.5 mm wide and $\sim$3mm deep grooves were cut. The

location of the grooves is illustrated in Figure 3.2. Figure 3.3 is a photograph of the crystal after the grooves were machined and prior to final processing.

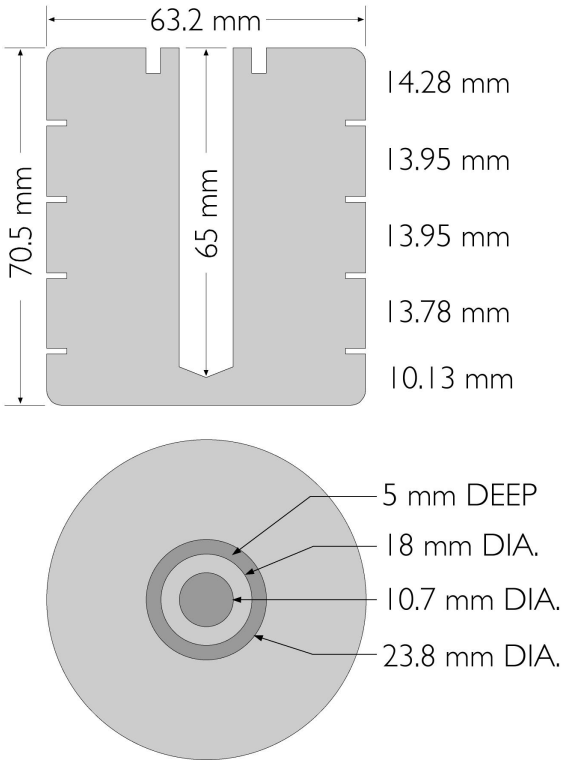

FIGURE 3.2. Schematic illustration of the placement of the grooves in the crystal. Prior to final processing, the grooves were cut to ∼3 mm depth and ∼0.5 mm width. After chemical treatment of the grooves to create a high-resistance surface, the width grew to ∼1.1 mm. The depth of the grooves is estimated to be ∼3.3 mm.

After successfully machining the circumferential grooves, the crystal was returned to PGT for processing and installation into a custom built cryostat. A schematic illustration of the assembled cryostat is shown in Figure 3.4 with detailed mechanical drawings of the cryostat given in Appendix A. The outer electrical contacts are not illustrated in this figure, but deserve mention. To make the outer electrical contacts, holes were drilled and tapped through the inner can to allow special bolts to press a thin wire into an indium patch on the segment. Indium is a commonly used material to make electrical contact with a germanium crystal because of its softness and conductivity.

FIGURE 3.3. Photograph of the PSEG detector after the grooves were cut and prior to final processing.

The detector required multiple processing attempts at PGT before the crystal was able to operate at depletion voltage. The delivered detector, named PSEG, is show in Figure 3.5 shortly after it arrived at the University of South Carolina.

After arriving at the University and verifying that the packaged detector operated within acceptable leakage current parameters, it was necessary to perform a controlled series of measurements to determine if the individual segments were electrically isolated. To do this, a well collimated low-energy gamma-ray source, ^{109}Cd, was placed approximately 6 inches from the crystal. With the collimated beam of gamma-rays focused at the center of the segment, data were collected from all six contacts. The data were then histogrammed to show whether there was signal leakage between segments. The results of this series of measurements clearly demonstrated that each segment was well isolated. Figure 3.6 is an example of a data set taken during the initial tests.[34] In this figure, the collimated source is focused at segment two. No evidence of

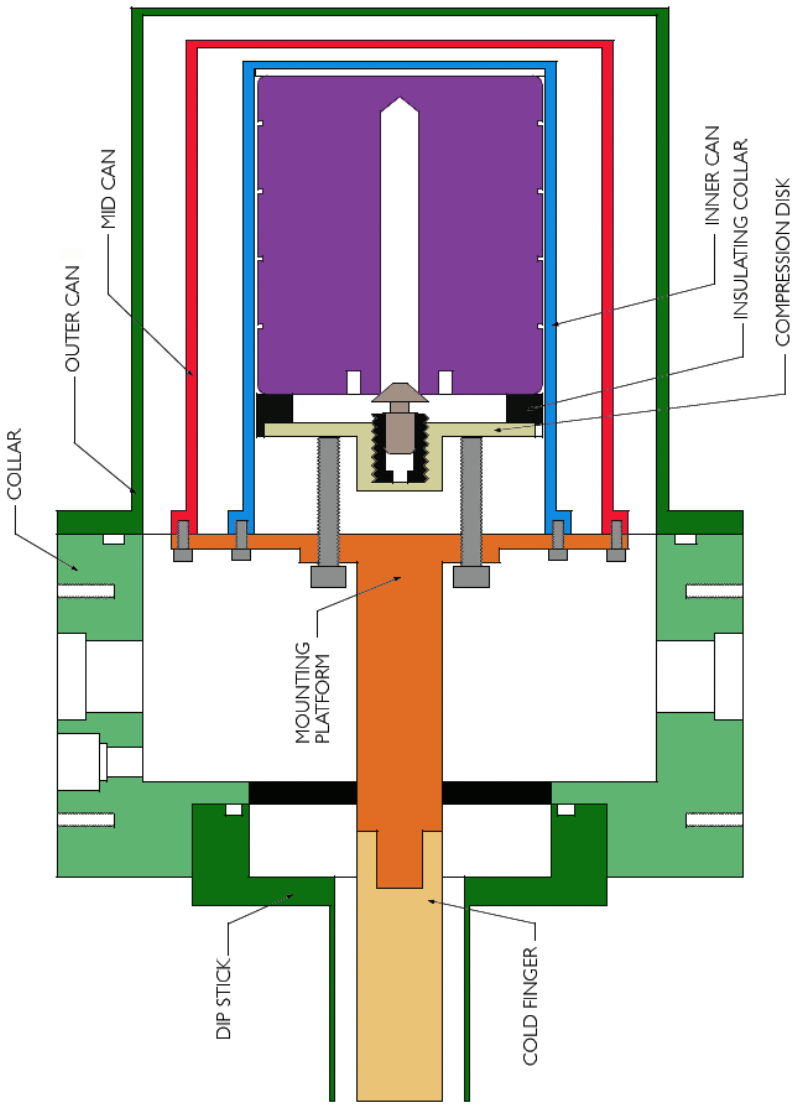

FIGURE 3.4. An illustration of the inside of the cryostat. Drawing is to scale. The abundance of space inside the cryostat was to facilitate prototype assembly. The electrical contacts of the outer segments are not shown. All six preamplifiers are rigidly mounted to the cryostat collar.

the 88 keV gamma ray peak can be seen in either segment one or three. While this does not indicate how effective segmentation will be, it does indicate that the physical grooving of the detector is a viable path to pursue further.

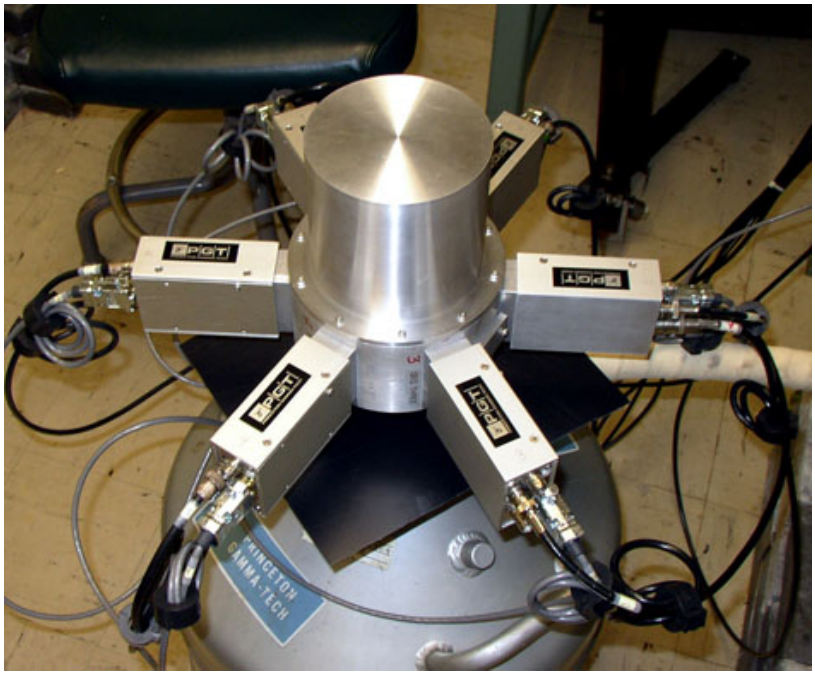

FIGURE 3.5. A photograph of the PSEG detector shortly after it arrived at the University of South Carolina. The boxes radiating outward from the cryostat are the preamplifiers. There are six preamplifiers in total - one for the center contact and one for each of the five outer contacts.

Additional details and a more thorough explanation of early measurements with PSEG can be found in references [33] and [34] but will not be further discussed except as needed. The remainder of this chapter focuses on recent improvements to the PSEG electronics.

3.3. ELECTRONICS

Core components of the PSEG detector are its preamplifiers. The center contact and each of the five segments is instrumented with a PGT RG11B charge-integrating preamplifier. The design of the preamplifier is decades old, but, it is still one of the more utilitarian preamplifiers for HPGe detectors due to the adjustability of operating parameters such at FET voltage, FET current, pole zero, and DC offset. There are two configurations in which HPGe preamplifiers can operate. In the first mode, the first stage of amplification is located in the

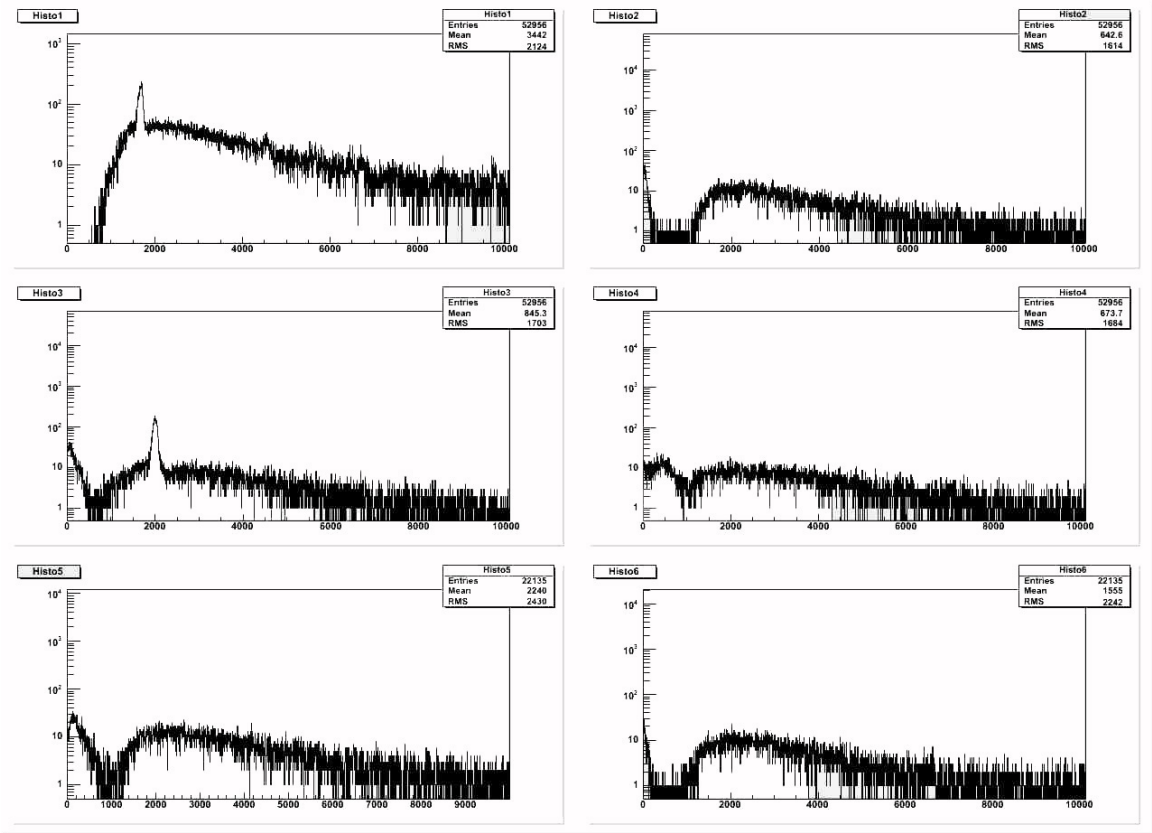

FIGURE 3.6. Example of the electrical isolation of the detector segments. In this particular data set, the collimated gamma-ray source was focused on segment two. In this figure, the upper left histogram is the center contact. Upper right histogram is segment one. Middle left histogram is segment two.

vacuum cryostat close to the germanium crystal. This is referred to as a cold FET configuration – see Figure 3.7(a). Conversely, in the second mode, the first stage of amplification is colocated with the second stage outside the vacuum. This is referred to as a warm FET configuration – see Figure 3.7(b).

There are positives and negatives with either configuration. For the PSEG detector, the preamplifiers were operated in the warm configuration because of the possibility of accidentally damaging the JFET in the first stage. In a warm configuration, its a simple matter of removing the preamplifier cover, removing the non-functioning JFET and soldering in a working replacement. In a cold configuration, if the JFET is damaged, the detector has to be warmed

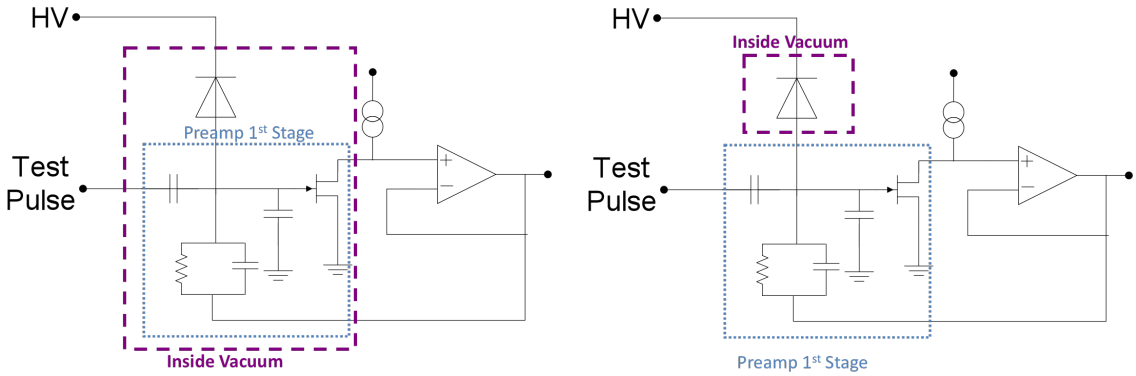

(a) Cold FET configuration (b) Warm FET configuration

FIGURE 3.7. Schematic illustrations of the first stage of the preamplifier. The germanium crystal is represented by the diode at the top of the figure. Figure (a) is the cold configuration with first stage located in the vacuum. Figure (b) is the warm configuration with the first stage colocated with the second stage outside of the vacuum. This is the configuration used with the PSEG detector.

and the vacuum cryostat breached in order to replace the JFET. This was not an acceptable risk for the PSEG detector since it was unknown whether warming the crystal would degrade or destroy segmentation. The downside of using the warm configuration for PSEG is the possible degradation of the signal prior to the first stage of preamplification. This could result in degraded energy resolution or signal bandwidth for pulse-shape discrimination. Previous work has shown that the minimum signal bandwidth to obtain satisfactory pulse-shape discrimination results is 25 MHz.[1]

3.3.1. Preamplifier Performance. Early efforts to demonstrate electrical segmentation were met with great success. However, further analysis efforts were hampered by extremely poor energy resolution. It was quickly observed that the magnitude and frequency of electronic noise in the system would prevent further analysis if not first addressed. Figure 3.8 shows some of the noise problems initially encountered in the system.

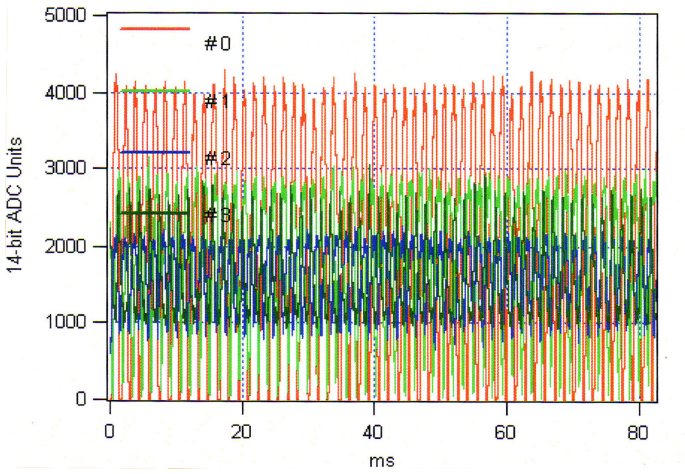

(a) Noise One

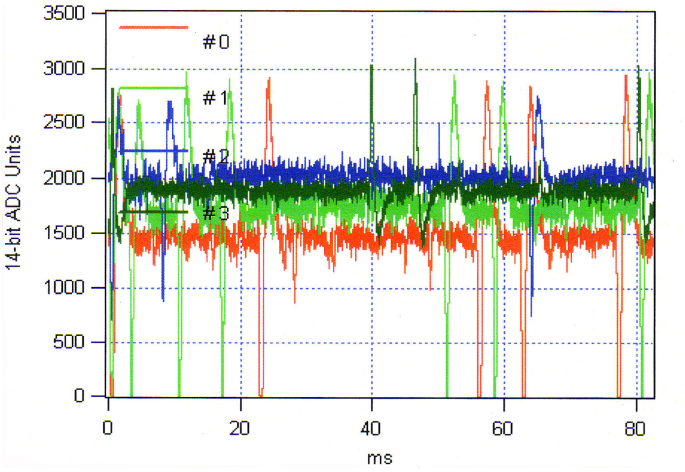

(b) Noise Two

FIGURE 3.8. Oscilloscope traces illustrating typical electronics noise encountered with PSEG. The four different-colored traces represent the four channels of a single XIA Pixie-4 DAQ card. Noise problems were constant, but the noise pattern would change randomly. (a) illustrates large amplitude low-frequency ($\sim$700 Hz) baseline noise. (b) illustrates large-amplitude random baseline noise chirps.

An extensive effort began in 2007 to track down and eliminate the sources of noise. To begin, new high voltage, signal, and preamplifier-power cables were procured and equal-length cable bundles assembled. A new Ortec Model 4003 NIM-based preamplifier power supply with 6 isolated and filtered channels was installed, and a high-capacity uninterruptible power supply was used

to filter the incoming main power. All of these efforts yielded only a small improvement. During these upgrades, the preamplifiers were observed to be rather old and in slightly differing configurations. This was a concern as older marginally-operational discrete components are known sources of noise. Several attempts were made to replace suspected-bad components. These repairs helped in most cases, and it was quickly apparent the the preamplifiers were the limiting factor in the noise performance.

It was decided that new preamplifiers would be purchased and installed. Upon complete replacement of the RG11s, a dramatic improvement in the noise performance was noted. For the center contact channel – primary energy channel – a base-line noise level of approximately 2 milli-Volts peak to peak ($\sim$2 mV_{PP}) was achieved. The outer-contact electronics channels did not experience the same performance improvement and suffered from noise in the microphonic frequency range with as much as 10 mV_{PP} amplitude. Although not optimal, the microphonics are on a time scale that is sufficiently long ($>$10 ms) compared to the median charge-collection time of a typical event ($\sim$500 ns), thus the impact on energy resolution performance is minimal. The reduced noise levels resulted in an improvement of the energy resolution on the center contact by a factor of 3 ($\sim$9 keV at 2615 keV to $<$3 keV at 2615 keV). Similar improvements were made in the energy resolution for the outer contacts.

3.3.2. Digital Waveform Acquisition. One of the most critical components of the electronics is the data acquisition system (DAQ). Originally, the PSEG detector was instrumented with the CAMAC-based DGF4C from XIA, LLC.[31] Each CAMAC module contains four pseudo-independently operated channels with flexible triggering that can span multiple modules. Each channel has an analog signal conditioning stage followed by a 14-bit 40 MHz ADC. The energy of the event is then reconstructed in a digital signal processor (DSP) using an adjustable trapezoidal digital filter. The user has the ability to store

digitized pulses up to 100 μs in length for later analysis, such as pulse-shape discrimination (PSD).

Initial PSD results with the PSEG detector indicated that the 40 MHz digitization rate was inadequate to maintain the fine structure of the pulses. To solve this problem, a newer product from XIA (Pixie-4) was installed. The compact-PCI based Pixie-4 system has the same functionality of the CAMAC-based system, but with lower overall noise and a faster 14-bit 75 MHz ADC. Complete details of the Pixie-4 system can be found in reference [30].

3.4. SUMMARY

The development of a new type of segmented germanium detector has been quite successful. While there are still outstanding questions regarding the long-term viability of a physically segmented p-type germanium detector – tolerance to thermal cycling and detector reconditioning – electrical isolation of segments and excellent energy resolution have been demonstrated. In the next chapter, details of the unique data analysis requirements related to improving the energy resolution and identification of valid energy depositions are presented.

CHAPTER 4

PSEG ANALYSIS

The analysis of PSEG data is fundamentally no different than it is for any other segmented germanium detector. For modestly-segmented detectors such as PSEG, 1 mm position resolution will never be achievable and therefore the complex analysis techniques used with highly-segmented detectors can be avoided. There are however several complications that make the analysis and event reconstruction for PSEG more challenging than a non-segmented detector. In the following sections, the analysis challenges will be reviewed and the solutions detailed.

4.1. EVENT RECONSTRUCTION

The begin the PSEG analysis, it is necessary to reconstruct the hit pattern for each event. The hit pattern is a TRUE-FALSE mask indicating which segments contain a valid energy deposition. Like most segmented germanium detector setups, the PSEG electronics are triggered by the center contact. For each trigger, the XIA Pixie-4 system, described in section 3.3.2, digitizes the preamplifier output pulse from the center contact and each of the five outer contacts. Each stored pulse is 6 μs in length to allow for offline application of user-implemented digital filtering if so desired. Figure 4.1 shows the digitized preamplifier outputs of a typical PSEG event. This triggering scheme ensures that spurious signals from outer contact channels do not falsely trigger the system. However, triggering the system in such a manner does not allow one to immediately know which segments contained an energy deposition.

To obtain the hit pattern, the data are processed on an event-by-event basis. The digitized preamplifier pulses from the five outer contacts are read into computer memory. For each pulse, the first 60 digitized points are averaged (AVG_{begin}) and last 60 digitized points are averaged (AVG_{end}). If the difference (AVG_{end} - AVG_{begin}) is greater than 1000 ADC units, then the channel is considered to contain a valid event and the hit pattern for that channel is set TRUE, otherwise the hit pattern for that channel is set FALSE. The segmentation geometry of the PSEG detector results in 31 possible hit patterns.

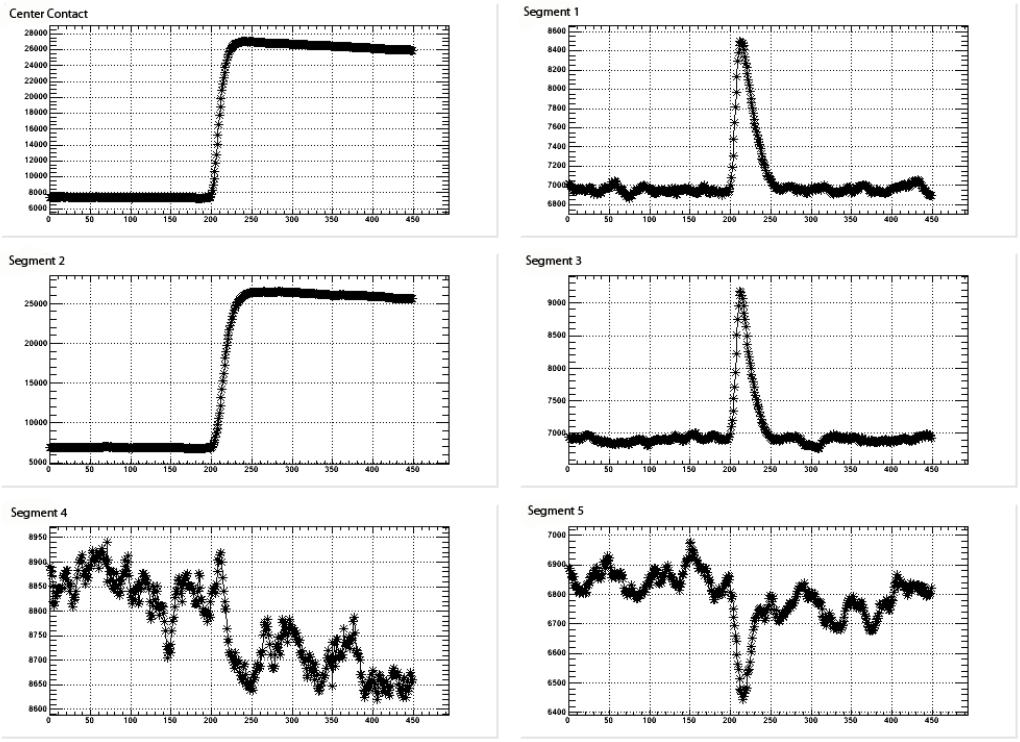

FIGURE 4.1. Digitized preamplifier traces for a typical event. The energy of this event is 1593.0 keV and the energy was entirely deposited in segment 2. Image charge can clearly be seen in segments 1 and 3.

Comment: The determination of what constitutes a valid energy deposition is a potential topic for debate. The method just described is in essence a crude high-pass energy filter. The need to implement such a filter is the result of image charge formation in the detector and the XIA Pixie-4 system's inability to

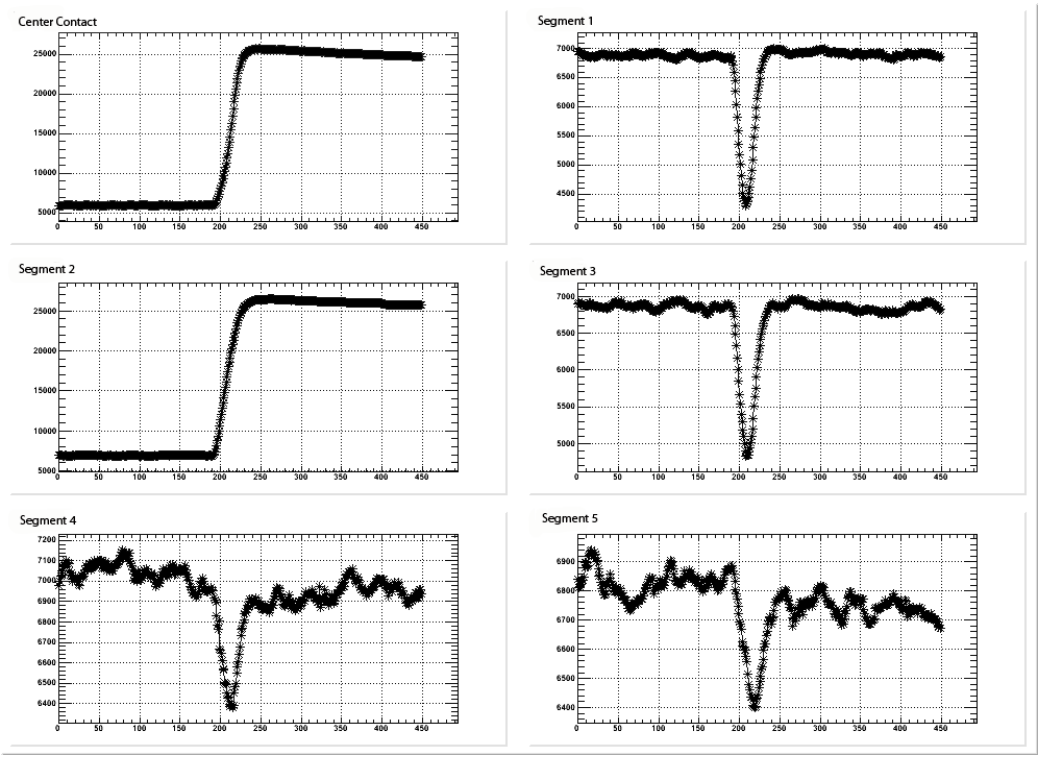

FIGURE 4.2. Digitized preamplifier traces for a typical event. The energy of this event is 1596.3 keV and the energy was entirely deposited in segment 2. Image charge can clearly be seen in segments 1, 3, 4, and 5.

correctly calculate the energy of such events. The events shown in Figures 4.1 and 4.2 correspond to energy depositions in only segment 2. As one would expect, the event is seen in segment 2 and the center contact. The pulses in segments 1, 3, 4, and 5 correspond to image charge. In comparing Figure 4.1 and Figure 4.2, the reader will likely notice the polarity difference in the image charge in segments one and three. This change in polarity results from the structure of the electric field within the crystal and the location of the energy deposition within the crystal. Image charge formation is a well studied characteristic of segmented germanium detectors and is crucial to obtaining the $\sim$1 mm position resolution in highly-segmented detectors.[21][35][40][22][13] For PSEG, the information that can be obtained from image charge is not needed for current research efforts and is presently ignored.

It is also necessary to explain the choice of a 1000 ADC unit threshold. It is said that a figure is worth a thousand words and that is certainly true in this case. The event in Figure 4.3 is very similar to the events in Figures 4.1 and 4.2 – the event deposited ∼1590 keV in segment 2 and image charge is recorded in segments 1, 3, 4, and 5. The difficulty with this event lies in segment 1. In addition to the image charge formation resulting from the energy deposition in segment 2, a low-energy energy deposition occurred in segment 1. This type of event easily passes the crude energy filter for low threshold values, however, the energy that is calculated by the XIA Pixie-4 energy filter is erroneously high. With threshold values less than ∼700 ADC units, these events were included in the processed data stream resulting in degraded PSEG energy resolution. This type of event occurs in less than 1% of the entire data set used in the analysis, therefore the incorrect classification of this type of event as single-segment has negligible consequences to the segmentation and pulse-shape discrimination analysis discussed in the following chapter.

4.2. Energy Calibration

The second step in the analysis of PSEG data is to perform a proper energy calibration for center contact events. A calibration is performed so that one can convert raw ADC values recorded by the Pixie-4 electronics into energy. To do this, a radioactive source with a broad range of well-know gamma-ray energies is placed in close proximity to the germanium crystal. Data are collected for a period of time sufficient to yield adequate counting statistics. Figure 4.4 is an example of a typical ADC spectrum obtained from PSEG using a ^{232}Th source. Centroids from five or more known peaks spanning the entire ADC dynamic range are located. The energy of the peak is plotted as a function of peak centroid and the data is fit with a second-order polynomial. While germanium detectors are know to be extremely linear in their response, slight

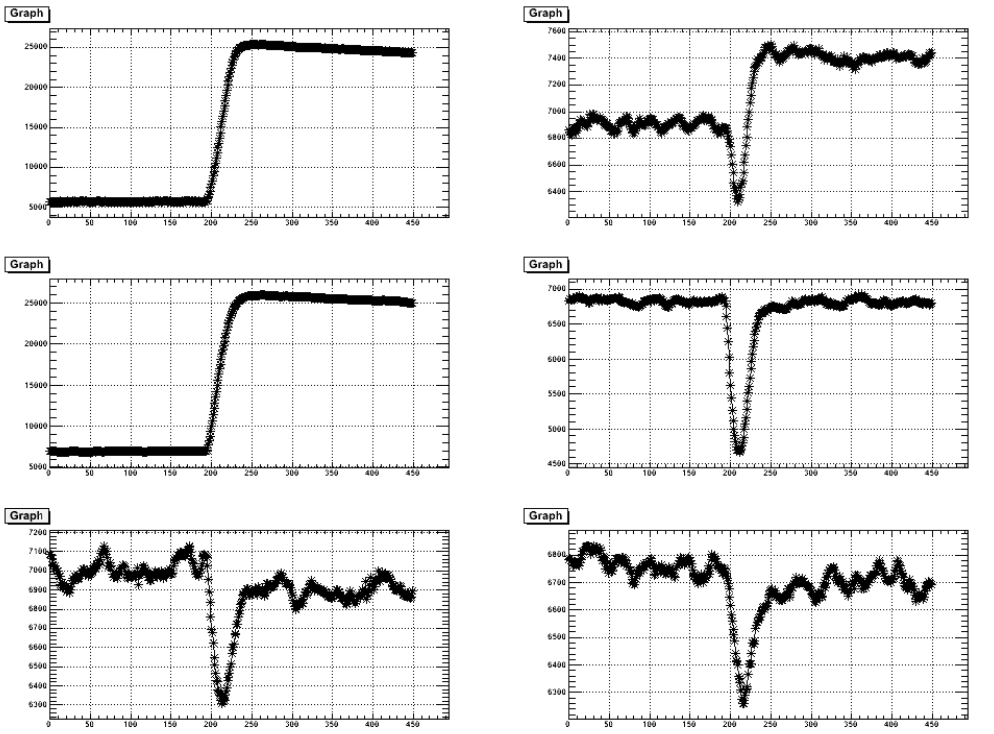

FIGURE 4.3. Digitized preamplifier traces for an event where most of the energy was deposited in segment 2 and a small fraction was deposited in segment 1. The pulse in segment 1 is a combination of the event in the segment plus the image charge from the large energy deposition ($\sim$1590 keV) in segment 2.

variations are compensated for by using the second-order term. Figure 4.5 shows an example of the fitting process. The fit produces three coefficients – the second order coefficient is the non-linearity (NL) term, the first order coefficient is the gain (G), and the zeroth order term is the offset (O). The fit coefficients are then used to convert from ADC units to energy in the following manner:

$$\text{Energy} = \text{O} + (\text{G} \times \text{ADC}) + (\text{NL} \times \text{ADC}^2) \tag{17}$$

In a typical germanium detector, this energy calibration is straight forward, but for the PSEG detector, the process is more complicated. In segmented germanium detectors, the energy of the event is measured at the center contact

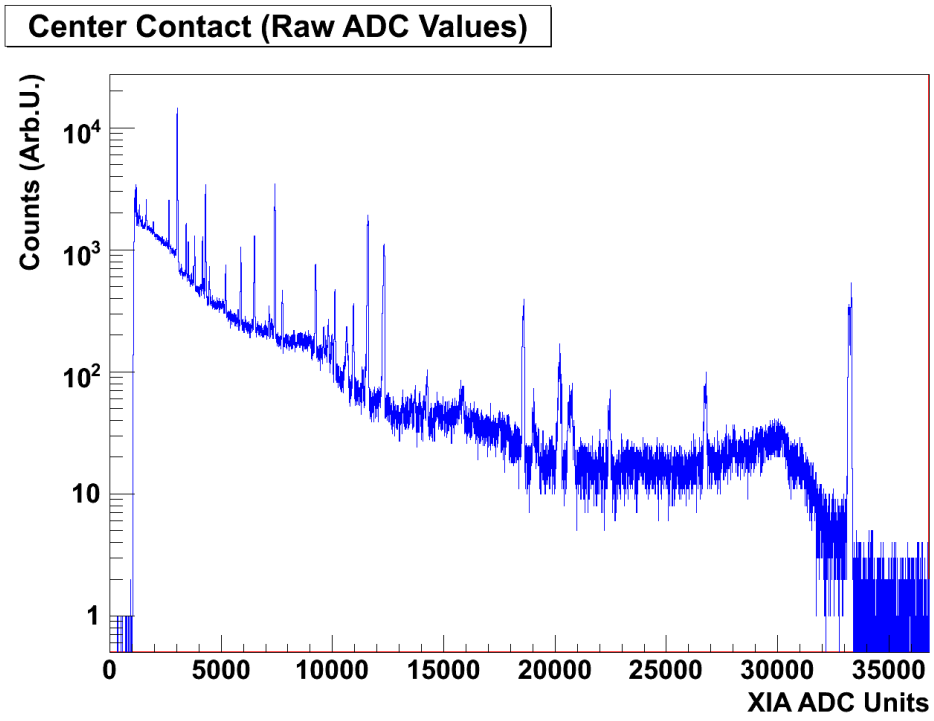

FIGURE 4.4. A typical ADC value spectrum from the center contact of the PSEG detector. The ADC stores values as a 16-bit word corresponding to a spectrum range from 0 to 65,535.

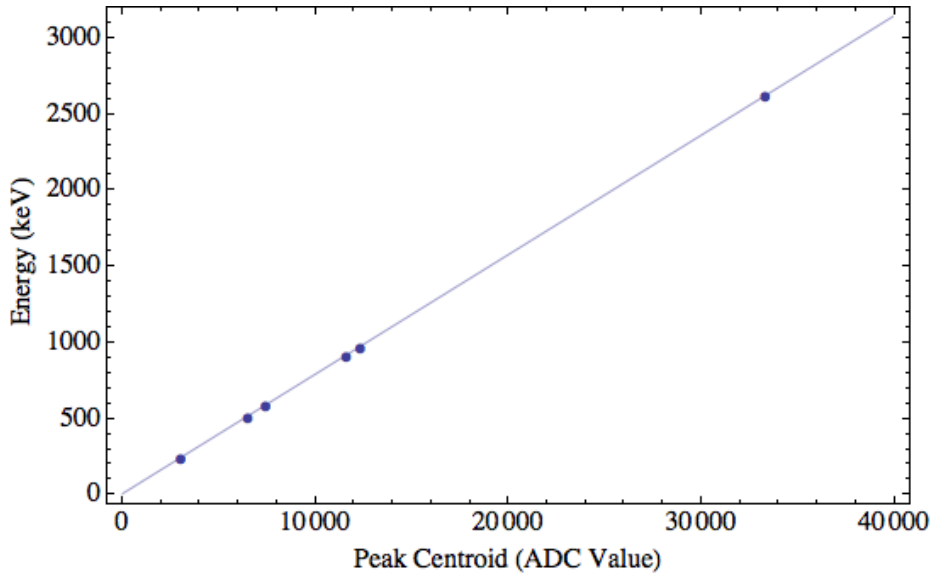

FIGURE 4.5. Peak energy plotted as a function of ADC centroid location and the second order polynomial fit to the data. The fit is nearly linear with an extremely small second-order term ($\sim 10^{-10}$)

and the outer contacts are used to determine the location of the event within the crystal. Calibrating the gain for the outer segments of PSEG is accomplished with the method previously described. For the inner contact however a more extensive procedure is required. Figure 4.6 illustrates the complexity inherent to the center contact data from PSEG. This portion of the ADC spectrum corresponds to the 2615 keV gamma ray from the decay of ^{208}Tl. In this histogram there appear to be two, possibly three, distinct peaks. Even more problematic is the energy region just above and below the double-escape peak (DEP) from the ^{208}Tl 2615 keV gamma ray, see Figure 4.7.

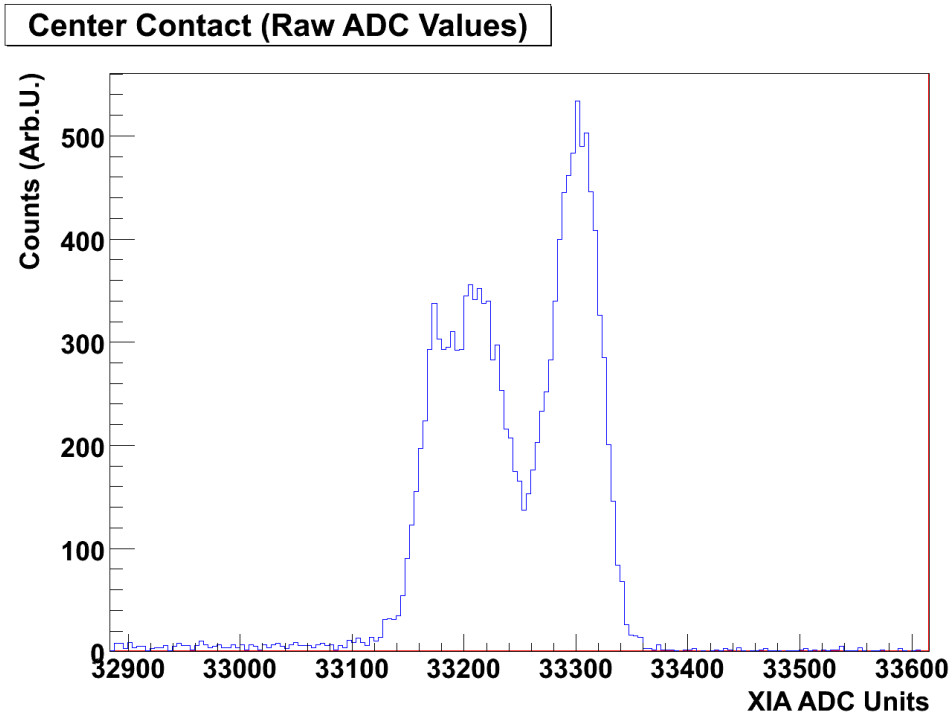

FIGURE 4.6. A range of ADC values corresponding to the 2615 keV gamma ray from ^{208}Tl.

An explanation for these multiplet peaks can be obtained through a simplified view of the PSEG detector. As discussed in section 3.2, the detector has one inner electronic contact – at negative high voltage – and five outer electronic contacts – at ground potential. As such, one could view PSEG as five individual detectors each with a slightly different electronic gain. By gain correcting each

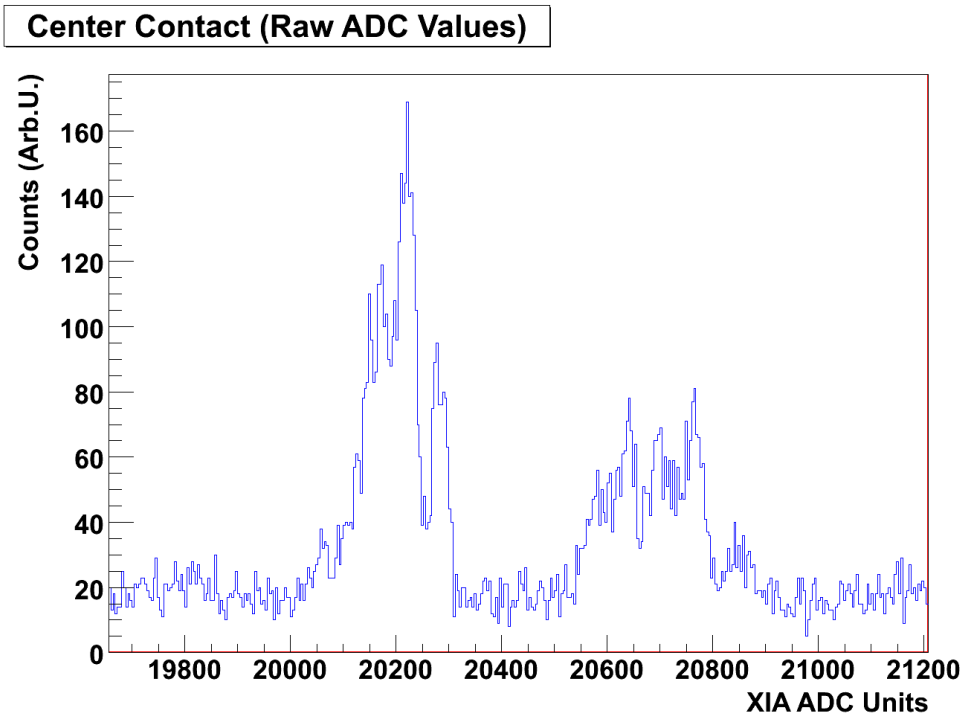

FIGURE 4.7. A portion of the ADC spectrum that contains the double-escape peak (DEP) of the 2615 keV gamma ray of ^{208}Tl. The cluster of peaks on the left of the histogram correspond to the 1592 keV DEP and the 1588 keV gamma ray of ^{228}Ac.

of the five segments separately, one should obtain a properly gain corrected energy spectrum without multiplet peaks.

4.3. CENTER CONTACT GAIN CORRECTION – SINGLE-SEGMENT EVENTS

To test this solution, the center contact data were processed using the hit pattern described earlier to locate events where energy was deposited in only one segment. Five histograms were incremented according to which segment contained the energy deposition. The data in these histograms did not exhibit the multiplet peaks seen in Figures 4.6 or 4.7. This was a good sign that a solution was at hand. Using the procedure described earlier, center-contact gain-correction coefficients were obtained for each segment – O_{seg}, G_{seg}, and

NL_{seg} where seg is the segment number where the energy was deposited. The code used to process and sort the data was modified to perform on-the-fly gain correction. Upon reprocessing the "single segment" data, the energy resolution performance for each segment and the sum were calculated. These values can be found in Table 4.1. The improvement in the resolution of the 2615 keV peak is shown in Figure 4.8 and the improvement in the region of the 2615 keV DEP is shown in Figure 4.9.

TABLE 4.1. Energy resolution measurements of the five individual segments. Each measurement corresponds to data in which the energy of the incident gamma ray was deposited solely in the corresponding segment.

Segment Number	Peak Centroid (keV)	Energy Resolution - FWHM (keV)
1	2614.86	2.75
2	2614.84	2.77
3	2614.92	2.81
4	2614.82	2.91
5	2614.89	3.00
Sum	2614.83	2.87

Treating the individual segments of PSEG as unique detectors is clearly a viable method for gain correction. A difficulty is introduced into the analysis when one attempts to process events in which the incident gamma-ray energy is deposited in more than one segment – multi-segment events. How does one perform a proper gain correction for these type of events? The answer lies in the signals from the outer contacts. Since these contacts are instrumented with preamplifiers capable of obtaining excellent energy resolution, one is able to determine how much of the total event energy was deposited in each segment. Using the fractional energy in each segment, along with the center contact gain shifting parameters for each individual segment, one can properly correct

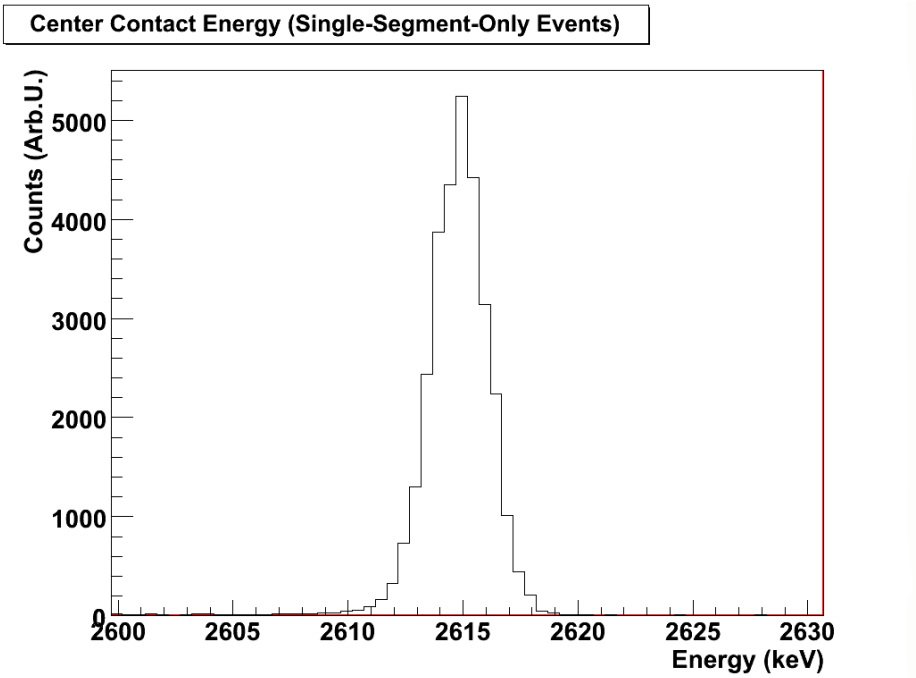

FIGURE 4.8. The 2615 keV gamma-ray peak from the decay of ^{208}Tl after properly gain shifting data from single-segment events. The shape of the peak in this figure can be compared to the multiplet peak in Figure 4.6. The data in both figures correspond to the same gamma-ray energy.

the energy of the event. Details of this calculation are presented in the next section.

4.4. CENTER CONTACT GAIN CORRECTION – MULTI-SEGMENT EVENTS

Correctly performing a gain shift on center contact data is tricky when multiple segments are involved in the event. The process that is described in this section works for those events that deposit energy in two to five segments. The examples and equations provided are for events where all five segments contained an energy deposition. For lower segment-multiplicity events it is a simple matter of neglecting terms involving segments without an energy deposition.

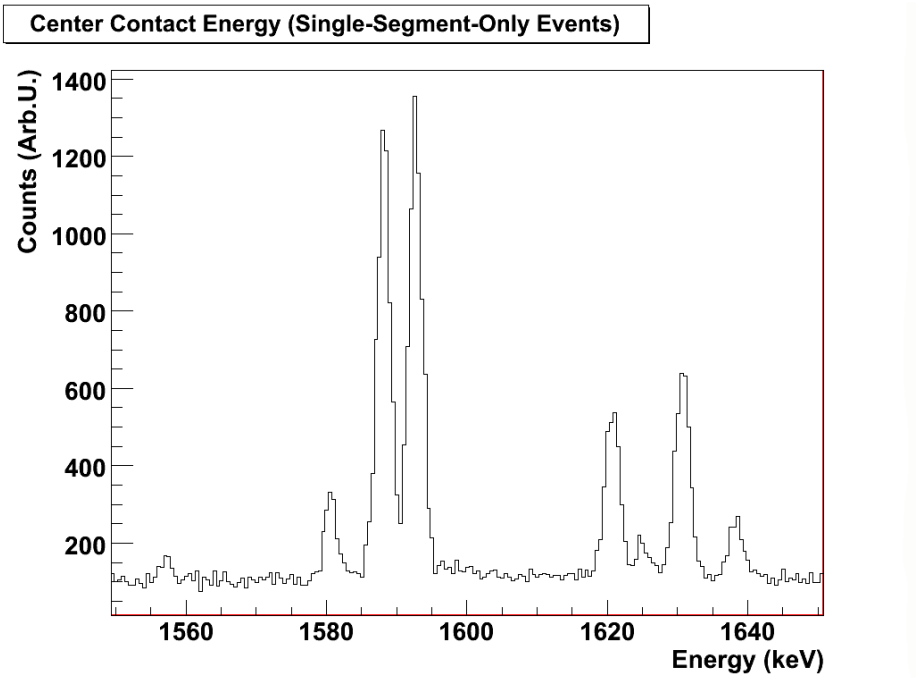

FIGURE 4.9. A 100 keV region around the 1592 keV DEP from ^{208}Tl after properly gain shifting data from single segment events. This energy range corresponds to the ADC range shown in Figure 4.7.

As an example of the process, consider that each of the five PSEG segments contains an energy deposition. Using the process described in section 4.2, the reconstructed energy from the segment 1 outer contact is given by $\mathrm{E}_1^{\mathbf{OC}}$. Similarly, the segment 2 outer contact energy is $\mathrm{E}_2^{\mathbf{OC}}$, the segment 3 outer contact energy is $\mathrm{E}_3^{\mathbf{OC}}$, the segment 4 outer contact energy is $\mathrm{E}_4^{\mathbf{OC}}$, and the segment 5 outer contact energy is $\mathrm{E}_5^{\mathbf{OC}}$.

The fraction of the total event energy, $\mathrm{E}f_{seg}$, in the segment, seg, is then given by:

$$\mathrm{E}f_{seg} = \frac{\mathrm{E}_{seg}^{\mathbf{OC}}}{\sum_{k=1}^{5} \mathrm{E}_k^{\mathbf{OC}}} \tag{18}$$

The next step is to gain correct the center-contact ADC value ($\mathrm{ADC}_{\mathbf{CC}}$) five times – once for each of the 5 sets of gain correction coefficients. This is accomplished using the procedure in section 4.2 with the gain correction factors

obtained in section 4.3, and is given by:

$$\mathrm{E}_{seg}^{\mathbf{cc}} = \mathrm{O}_{seg} + (\mathrm{G}_{seg} \times \mathrm{ADC}_{\mathbf{cc}}) + (\mathrm{NL}_{seg} \times \mathrm{ADC}_{\mathbf{cc}}^{2}) \tag{19}$$

This will result in five different center contact energy values for the same event – $\mathrm{E}_{1}^{\mathbf{cc}}$, $\mathrm{E}_{2}^{\mathbf{cc}}$, $\mathrm{E}_{3}^{\mathbf{cc}}$, $\mathrm{E}_{4}^{\mathbf{cc}}$, and $\mathrm{E}_{5}^{\mathbf{cc}}$. Multiplying each $\mathrm{E}_{seg}^{\mathbf{cc}}$ by $\mathrm{E}f_{seg}$ – where seg corresponds to the segment number – and summing the five terms,

$$\mathrm{Energy} = \sum_{seg=1}^{5} \mathrm{E}_{seg}^{\mathbf{cc}} \mathrm{E}f_{seg} \tag{20}$$

results in a properly gain-corrected center contact energy. Application of this method results in an energy resolution (FWHM) for the 2615 keV peak of 2.86 keV with a peak-centroid location of 2614.71 keV. Figure 4.10 and 4.11 are from the histogram containing all of the reconstructed events for the data set – 3,038,962 events. In comparing Figure 4.11 to Figure 4.9, the reader may notice the increased intensity of the 1588 keV peak relative to the 1592 keV peak. This is the result of including all event types in Figure 4.11, whereas Figure 4.9 is for events that occur in a single segment. Since the 1592 keV line is the double-escape peak from ^{208}Tl, one would not expect the intensity of this line to increase as events with higher segment multiplicity are considered.

4.5. SUMMARY

In the final analysis, the event sorting and gain correction for PSEG is not terribly complicated. However, that can only be said after many months of work uncovering the many idiosyncrasies of the detector and electronics and developing analysis routines to solve the problems. As a note, it is important for the reader to understand that the simplification and assumptions made – such as the sum of the energies measured at the outer contacts is equal to the energy recorded at the center contact – are valid as evidenced by the excellent

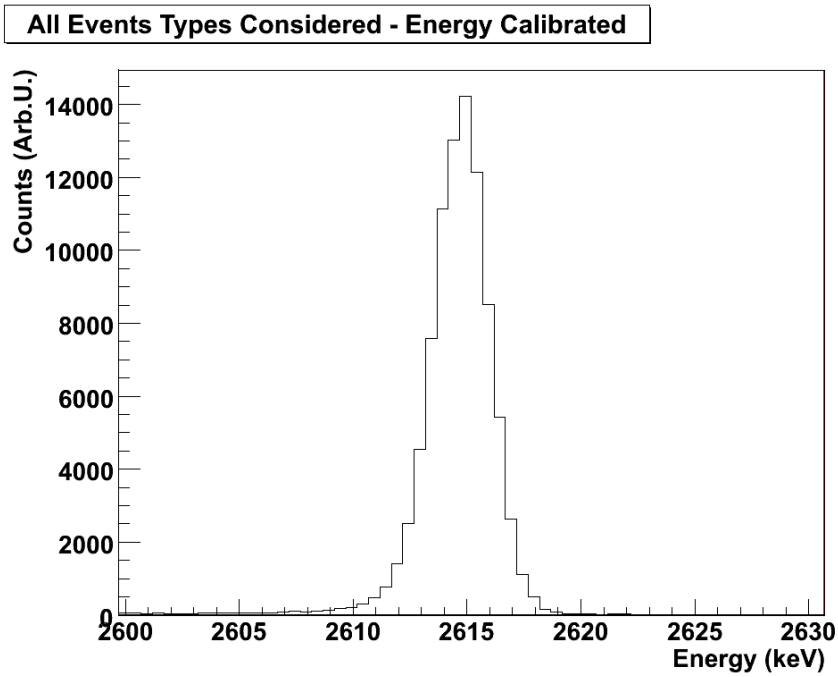

FIGURE 4.10. The 2615 keV gamma-ray peak from the decay of ^{208}Tl after properly gain shifting data from all event types. This figure should be compared to Figure 4.8 and 4.6 (for ADC values corresponding to the same energy range).

energy resolution performance of the detector. The energy calibration technique and event sorting are crucial before more advanced analysis techniques, such and pulse-shape discrimination and segmentation, can be implemented. In the next chapter, the background reduction efficacy of applying these advanced techniques is quantified and discussed.

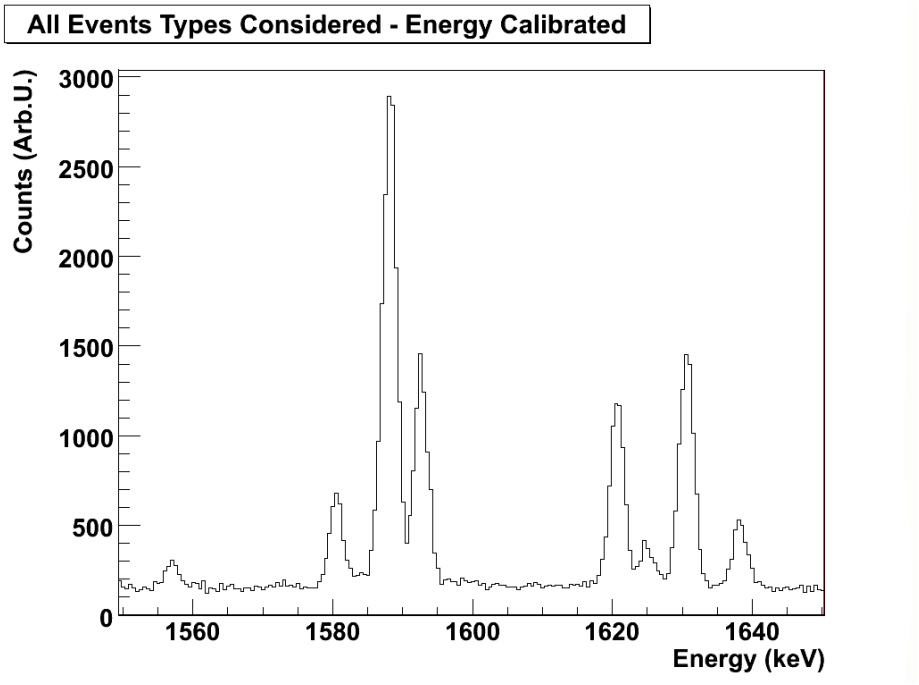

FIGURE 4.11. 100 keV region around the 1592 keV DEP from ^{208}Tl after properly gain shifting data from all event types. This figure should be compared to Figure 4.9 and 4.7(for ADC values corresponding to the same energy range).

CHAPTER 5

BACKGROUND REDUCTION EFFICACY

When further efforts to increase materials purity are no longer practical, analysis methods are required to mitigate remaining background interferences. A complete list of techniques planned for next generation ^{76}Ge $0\nu\beta\beta$-decay experiments is provided in section 2.2. In this chapter, implementation of two of these analysis cuts – segmentation and pulse-shape discrimination (PSD) – are described and their background rejection efficacy for PSEG data is quantified.

5.1. BACKGROUND REDUCTION USING SEGMENTATION

The application of a segmentation cut is the most straightforward of the two analysis cuts implemented for this work. As discussed previously, for each event, a hit pattern is formed by looking at which segments contain a valid energy deposition. The segmentation geometry of the PSEG detector results in a total of 31 possible hit patterns. By applying a logical comparison between the event hit pattern and the hit pattern required for analysis, an event can be accepted or rejected. Figure 5.1 is an example that illustrates the power of the segmentation cut. The figure contains three histograms - the white histogram is the raw (uncut) data, the grey histogram is the result of applying a "single-segment only" cut, and the black histogram is the result of applying a "two-adjacent-segment only" cut. While both cuts reduce the 1588 keV peak by roughly half, the 1592 keV peak is almost entirely rejected by the "two-adjacent-segment only" cut and accepted by the "single-segment only" cut. This

is consistent since the 1592 keV line corresponds to the double-escape peak of the 2615 keV gamma ray of ^{208}Tl.

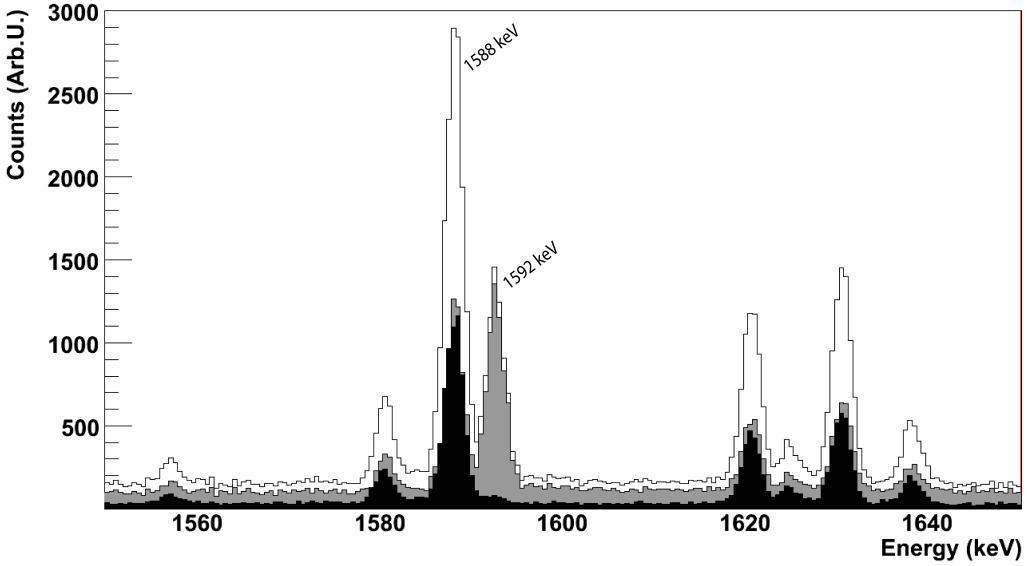

FIGURE 5.1. This figure illustrates the rejection of events based on the number of segments involved in the event. The white histogram is the raw (uncut) data in the energy region 1550 keV to 1650 keV. The grey histogram is the result of vetoing events in which more than one segment recorded an energy deposition. The black histogram contains those events in which energy was deposited in two adjacent segments.

For a $0\nu\beta\beta$-decay event, the signature will be single site and thus would be single segment. Using the definition in equation 16, the efficacy of the single-segment-only (single-site-only) segmentation cut can be quantified. Using the data in Figure 5.1 the figure of merit (FOM) for the segmentation cut is 1.428. Comparing this FOM value to that – calculated from simulation – in Table 2.1 for external ^{208}Tl for a 1-by-5 segmentation, its clear that the cut efficacy with the PSEG detector is far short of the predicted value of 2.410. The impact to next-generation experiments resulting from this lower-than-predicted FOM are discussed in chapter 6.

5.2. BACKGROUND REDUCTION USING PULSE-SHAPE DISCRIMINATION

Several techniques for pulse-shape discrimination in germanium detectors have been investigated[29][1][35][37][2][10]. All of these techniques use properties of the current pulse in an attempt to determine the number of unique energy deposition locations within the crystal for a given event. In general, the focus is to separate single-site events from multi-site events. For analysis of the PSEG data, a multi-parametric approach was utilized. Complete details of the technique can be found in reference [1], but a brief summary is presented here.

5.2.1. Review of Multi-Parametric PSD. To begin, the current pulse is reconstructed from the charge-integrated preamplifier output pulse using a Savitzky-Golay (SG) filter.[43] (Figure 5.2 is an example of applying an SG filter of order 9 to an integrated preamplifier pulse.) The discriminator algorithm then calculates three parameters from each current pulse. These parameters were chosen as a result of extensive simulation studies on the charge transport, charge collection, and electronics response of germanium detectors and therefore have a physically motivated origin.[1] The parameters are pulse width, pulse asymmetry, and normalized moment and are calculated in the following manner:

- The pulse width is the amount of time over which the current pulse evolves. To calculate the value, the time at which the maximum current is observed is located, MAXCURRENT. The beginning of the pulse is found by moving back in time from MAXCURRENT until the value of the current falls below a user defined threshold. The end of the pulse is determined in a similar fashion by looking forward in time from MAXCURRENT.

- The pulse asymmetry is calculated from the area of the current pulse. The midpoint of the pulse is located using the information calculated in the previous step. The area under the curve is integrated for the first half of the pulse – FRONT-HALF – and the last half of the pulse – BACK-HALF. Subtracting the BACK-HALF from the FRONT-HALF and dividing by their sum yields the pulse asymmetry.
- The normalized moment is calculated using the equation for the normalized moment of a square pulse, namely:

$$I_n = \frac{\sum_{i=N_0}^{N} j_i((i - N_{mid})\Delta t)^2}{\frac{1}{12}\sum_{i=N_0}^{N} j_i \Delta t^2} \tag{21}$$

  where j_i is the value of the current at i, N_{mid} is the midpoint of the pulse, Δt is the time step, N_0 is the starting sample of the pulse, and N is the number of samples between the beginning and end of the pulse.

By histogramming these three parameters for each event, a distribution is created in a three-dimensional parameter space. The discriminator compares the parameter-space distribution of experimental events to a parameter-space distribution of known single-site events. Events that fall outside of the specified single-site distribution are considered to be multi-site and vetoed. Figure 5.3 is a example distribution of single-site events from a semi-coaxial germanium detector – from the 1592 keV double-escape peak of ^{208}Tl. Figure 5.4 is an example distribution of single- and multi-site events from a semi-coaxial germanium detector – from the energy range 1550 keV to 1700 keV. Using the single-site distribution in Figure 5.3 to form the parameter-space acceptance region, the PSD algorithm is applied to the data in Figure 5.4. The result of applying the PSD cut is shown in Figure 5.5. The discriminator accepted

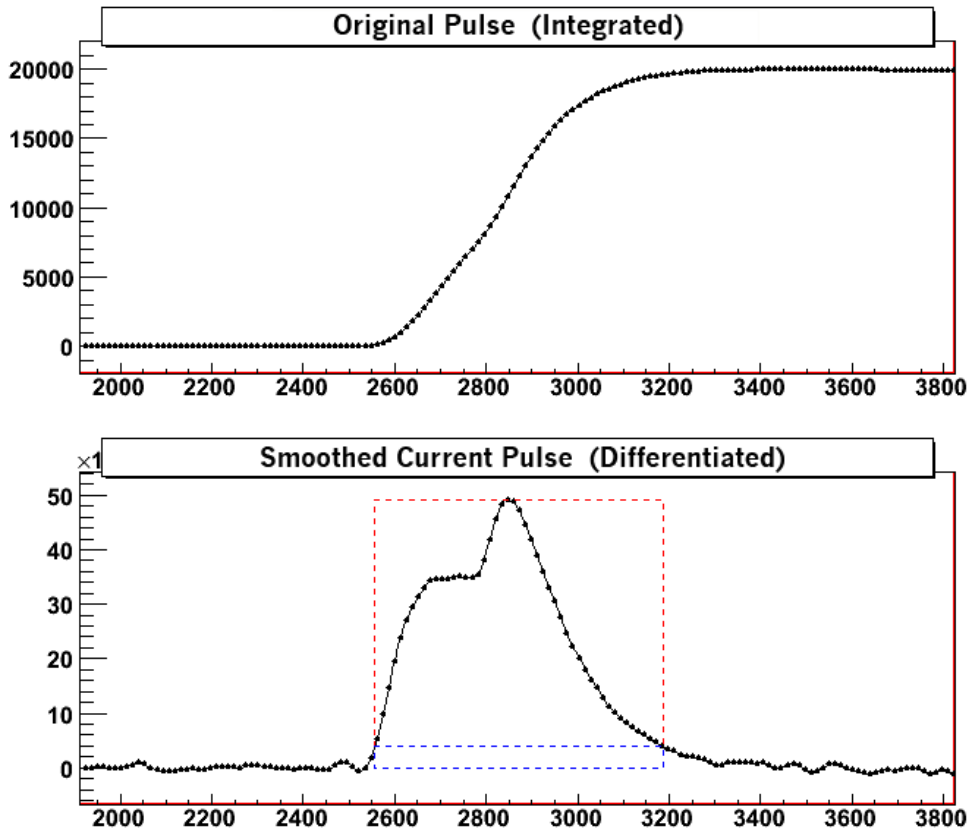

FIGURE 5.2. Result of applying the Savitzky-Golay filter to reconstruct the current. The top pane is the preamplifier output pulse (integrated) and the lower pane is the smoothed current pulse (differentiated).

80.18% of the signal of interest (single-site events) while rejecting 73.55% of background (multi-site events). This results in a figure of merit (FOM) of 1.56.

5.2.2. Pulse-Shape Discrimination with PSEG. With a basic understanding of the pulse-shape discrimination (PSD) algorithm now understood, attention is directed to the implementation of the PSD cut to PSEG data. The analysis begins with a sorted and gain-shifted data set. A three-dimensional parameter space of single-site events is created by gating on events that fall between 1592 keV and 1595 keV – the double-escape peak (DEP) from ^{208}Tl. (As a note, the lopsided DEP region-of-interest (ROI) was chosen such that the tail of the 1588 keV peak would not pollute the single-site population.) The

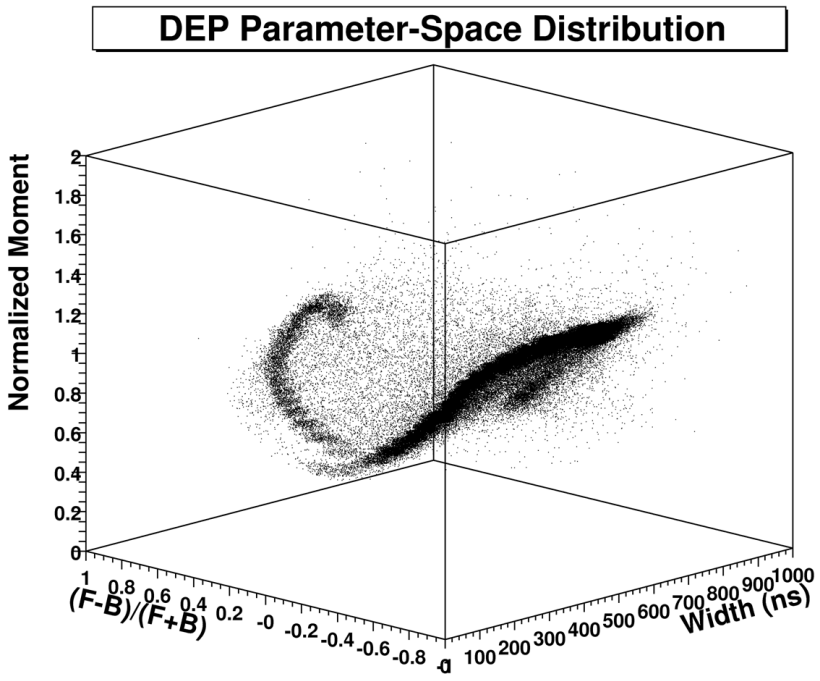

FIGURE 5.3. The 3-D parameter space distribution of single-site events. These events are from the double-escape peak of ^{208}Tl. Graphic taken from [1].

resulting three-dimensional parameter space is shown in Figure 5.6 with two-dimensional projections shown in Figures 5.7, 5.8, and 5.9. This parameter space was created using a Savitzky-Golay (SG) filter of order 9 with 100 bins per histogram axis.

Examining the parameter space for events of all energies – shown in Figure 5.10 with 2-D projections in Figures 5.11, 5.12, and 5.13 – one immediately notices that the distribution of events is much less well defined than the acceptance region shown in Figure 5.6.

Applying the PSD cut to the events in an energy range from 1550 keV to 1650 keV, see Figure 5.14, one immediately notices that the 1592 keV peak is almost completely preserved while the 1588 keV peak is reduced by roughly one third. To quantify the efficacy of the cut, equation 16 is used, with $\epsilon_{\beta\beta}$ as the

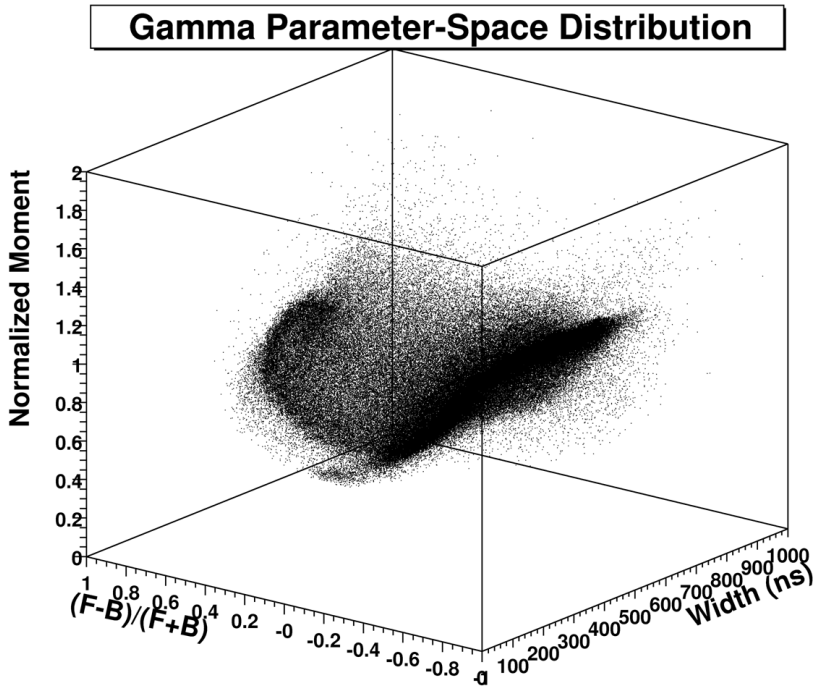

FIGURE 5.4. The 3-D parameter space distribution of multi-site events. These events are from the 1620 keV full-energy peak of ^{212}Bi. Graphic taken from [1].

acceptance fraction of 1592 keV-peak events (1.0) and $\epsilon_{background}$ the acceptance fraction of 1588 keV-peak events (0.6884). This results in a FOM of 1.205.

While this FOM is good, its not as good as one might expect given previous PSD results from reference [1]. Hope is not lost; there are two parameters that can be "tweaked" in an attempt to improve the PSD cut efficacy. The first is the parameter space acceptance fraction – the amount of the single-site parameter-space distribution used to form the acceptance region. The second is the binning granularity of the parameter space.

5.2.3. Adjusting the Acceptance Fraction. When the acceptance fraction is adjusted, one is in essence focusing in on the core of the single-site distribution. To explain this statement, its necessary to understand how the acceptance region is defined. To begin the process, the DEP events used to form the acceptance region are histogrammed into the parameter space. The

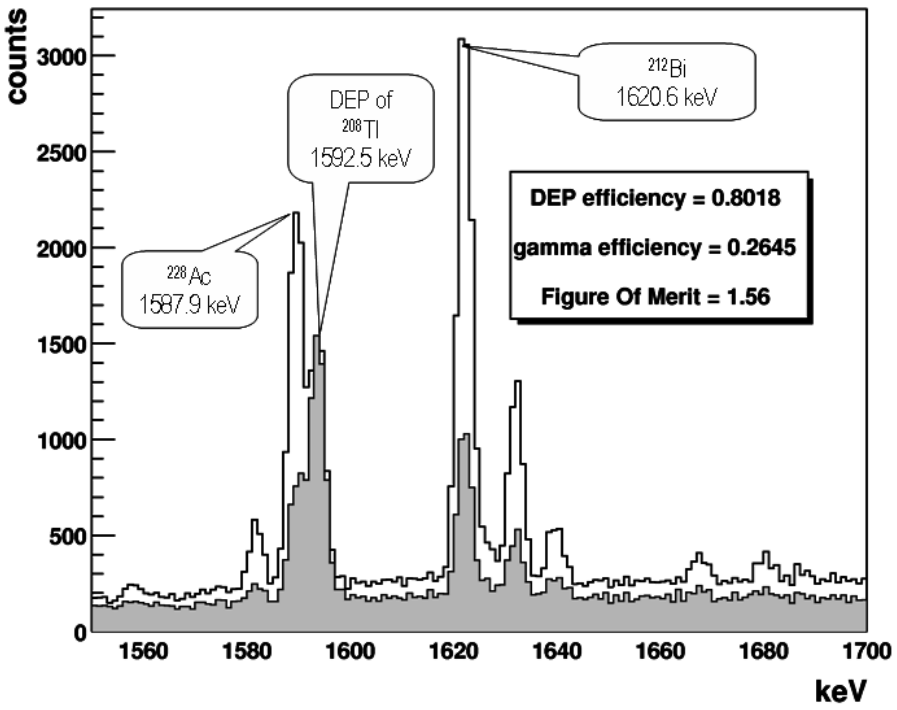

FIGURE 5.5. Results of applying the 3-D parameter-space discriminator to data from a ^{208}Tl source. The white spectrum is the raw energy histogram. The gray spectrum is the result of applying the discriminator – 1592 keV peak height has been normalized. Graphic taken from [1].

histogram bins are then sorted in descending order of bin contents. The sorted list is summed, also in descending order, until a user-specified percentage of the total number of events is reached. This percentage is the parameter-space (PS) acceptance fraction. This implies that a smaller PS acceptance fraction results in a smaller acceptance region.

The PS acceptance fraction is specified by the user at the time the PSD cut is applied. To examine the effect of adjusting the PS acceptance fraction, the data in Figure 5.14 were reprocessed with PS acceptance fractions of 0.75, 0.55, and 0.45. The effect of reducing the acceptance region is seen in Figure 5.15. The figures of merit for the different PS acceptance fractions are summarized in Table 5.1.

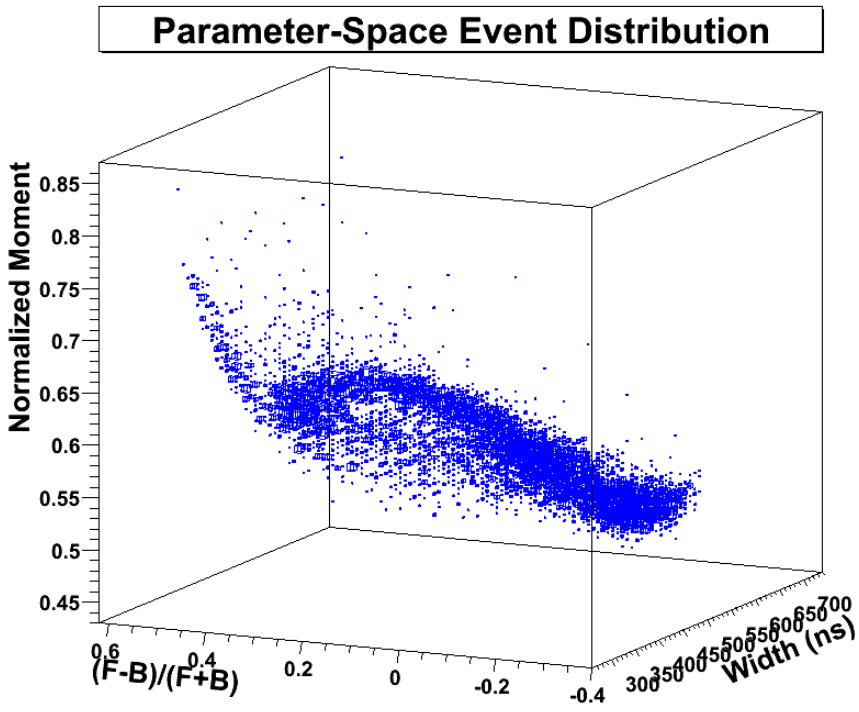

FIGURE 5.6. The 3-D parameter-space distribution corresponding to those events in the double-escape peak (DEP) energy region 1592 keV to 1595 keV.

TABLE 5.1. Compilation of the figures of merit (FOM) for different parameter-space acceptance fractions for a given data set. (Details: SG order = 9, bins per axis = 100)

Acceptance Fraction	*1588 keV Pk Cts* Raw	Residual	*1592 keV Pk Cts* Raw	Residual	*Figure of Merit (FOM)*
0.95	5076.74	3494.89	2270.94	2270.94	1.205
0.75		2577.63		1818.31	1.124
0.55		1901.08		1426.31	1.026
0.45		1293.56		1058.57	0.923

Analysis of the data shows the 1588 keV background peak to be increasingly reduced as the PS acceptance fraction is reduced, so to is the 1592 keV single-site peak. This is to be expected, however, the reduction in the 1588 keV peak must be more than the square of the reduction in the 1592 keV peak in order

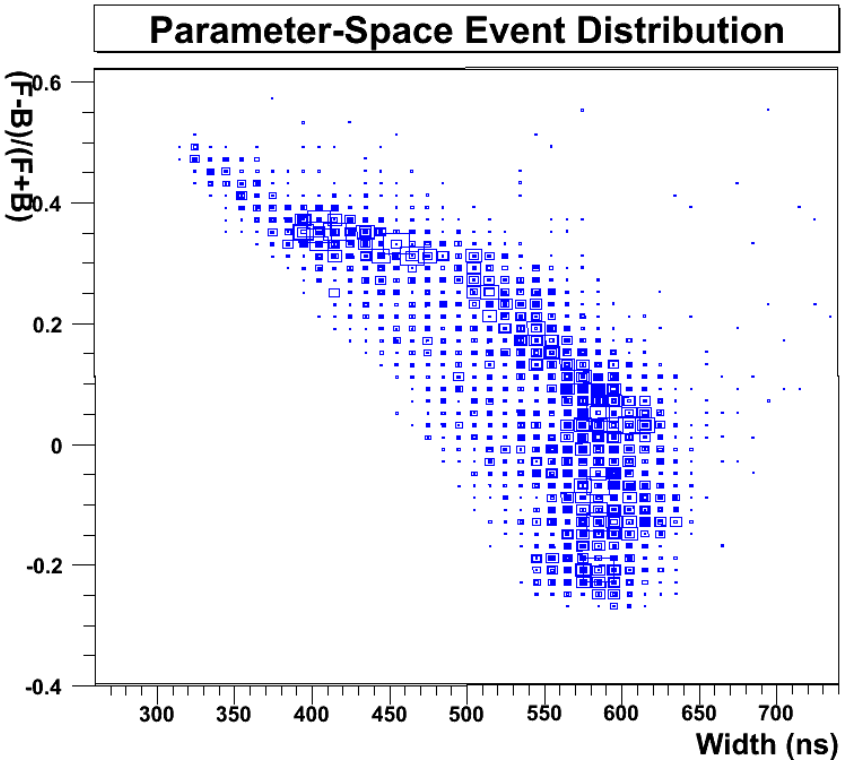

FIGURE 5.7. A two dimensional projection of the three dimensional parameter-space distribution corresponding to those events in the double-escape peak (DEP) energy region 1592 keV to 1595 keV. The data have been projected onto the pulse asymmetry vs. pulse width plane.

for the PSD cut to be more effective. The figures of merit in Table 5.1 indicate that at a 55% parameter-space acceptance fraction, the PSD cut is no longer effective. From this data set, one could conclude that it is beneficial to maintain as much of the parameter-space acceptance region as possible. For larger data sets that contain more DEP events, this conclusion may no longer hold as the edges of the distribution will likely become less defined.

5.2.4. Adjusting the Binning Granularity. Another parameter that can be adjusted in an attempt to improve PSD cut efficacy is the binning granularity of parameter space. The previous analysis utilized a parameter space of 100^3 bins – 1 million voxels (smallest distinguishable box-shaped part of a three dimensional space). The hypothesis here is that increasing the number

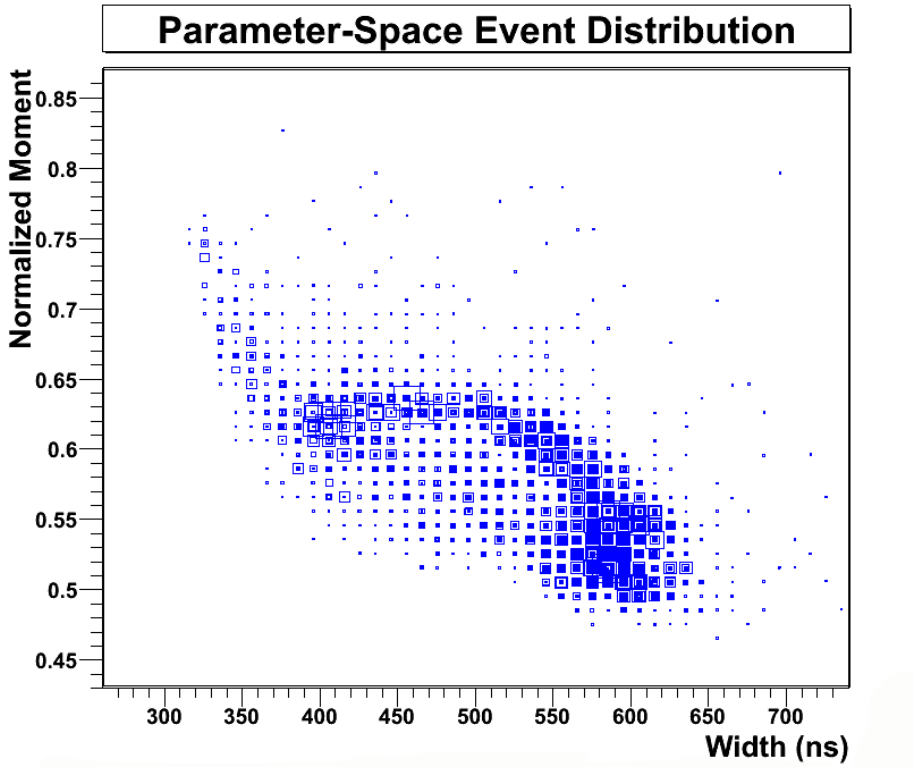

FIGURE 5.8. A two dimensional projection of the three dimensional parameter-space distribution corresponding to those events in the double-escape peak (DEP) energy region 1592 keV to 1595 keV. The data have been projected onto the normalized moment vs. pulse-width plane.

of bins in the parameter space will more sharply define the acceptance region. To test this hypothesis, the single-site parameter space used to define the acceptance region was regenerated with 125 bins per histogram axis – roughly doubling the number of voxels in parameter space. Results of applying the PSD algorithm with parameter-space acceptance fractions of 0.95, 0.65, and 0.35 are shown in Figure 5.16 and summarized in Table 5.2

Note: As the reader may have noticed, the acceptance fractions used in the 100 bins/axis versus 125 bins/axis analysis are different. This is a result of the algorithm used to define the acceptance region in parameter space. As previously mentioned, the parameter-space histogram bins are sorted in descending

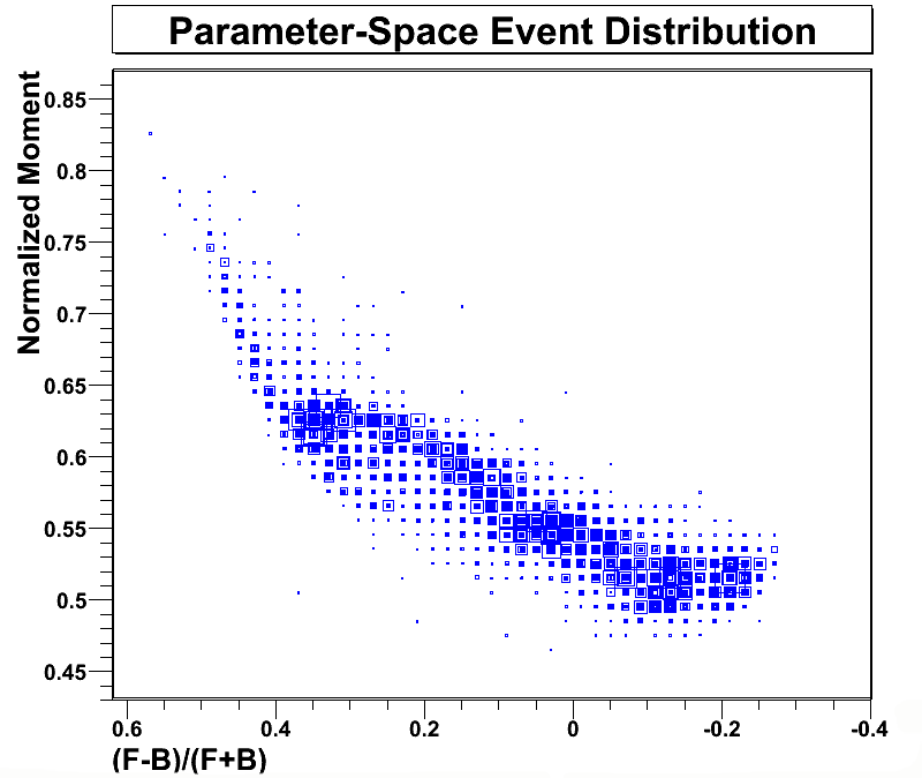

FIGURE 5.9. A two dimensional projection of the three dimensional parameter-space distribution corresponding to those events in the double-escape peak (DEP) energy region 1592 keV to 1595 keV. The data have been projected onto the normalized moment vs. pulse-asymmetry plane.

TABLE 5.2. Compilation of the figures of merit (FOM) for different parameter-space acceptance fractions for a given data set. (Details: SG order = 9, bins per axis = 125)

Acceptance Fraction	*1588 keV Pk Cts* Raw	Residual	*1592 keV Pk Cts* Raw	Residual	*Figure of Merit (FOM)*
0.95	5076.74	2743.47	2270.94	2270.94	1.360
0.65		1603.11		1520.04	1.191
0.35		931.06		936.00	0.962

order. The bins are then summed in descending order until the user-defined acceptance fraction of the total number of events is reached. The algorithm uses the bin contents of the summed bin that surpassed the threshold to define the

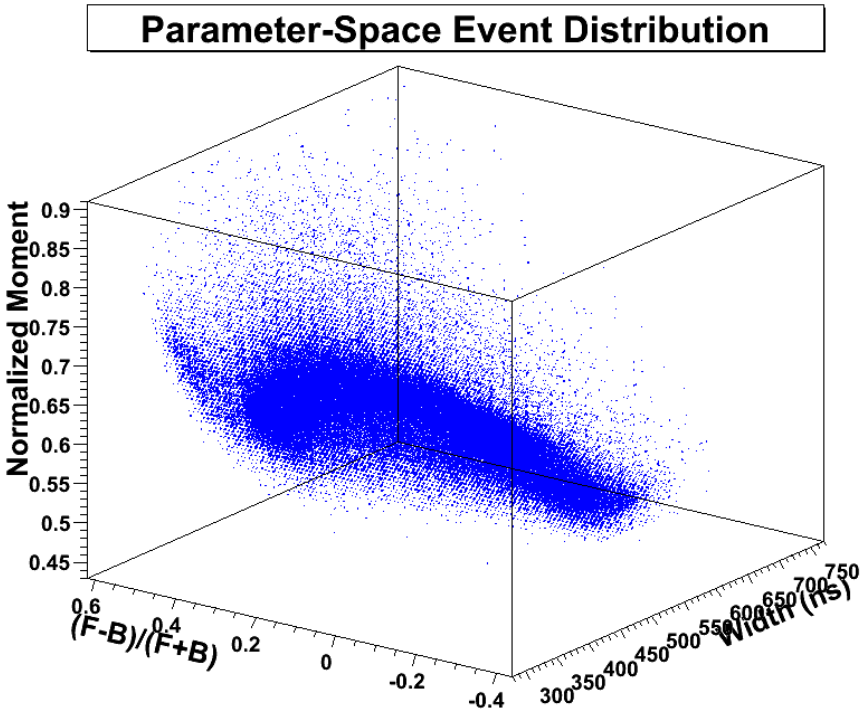

FIGURE 5.10. The 3-D parameter-space distribution corresponding to those events in the double-escape peak (DEP) energy region 1592 keV to 1595 keV.

minimum bin contents used to define the edges of the acceptance region. An example might be useful; if the acceptance fraction is reached and the bin contents are 5 events, then the acceptance region is defined by those bins from the DEP distribution that contain 5 or more events. By increasing the bin granularity to 125 bins per axis, the user defined acceptance fraction may be reached for a bin containing 3 events. So, as the granularity of parameter space is increased each bin will, on average, contain fewer events and more bins will have the same number of events.

5.3. COMMUTATION OF SEGMENTATION AND PSD CUTS

As alluded to in chapter 2, an important consideration in the application of the analysis cuts is the order of operation. Does the application of a PSD cut prior to a segmentation cut or a segmentation cut prior to a PSD cut change the

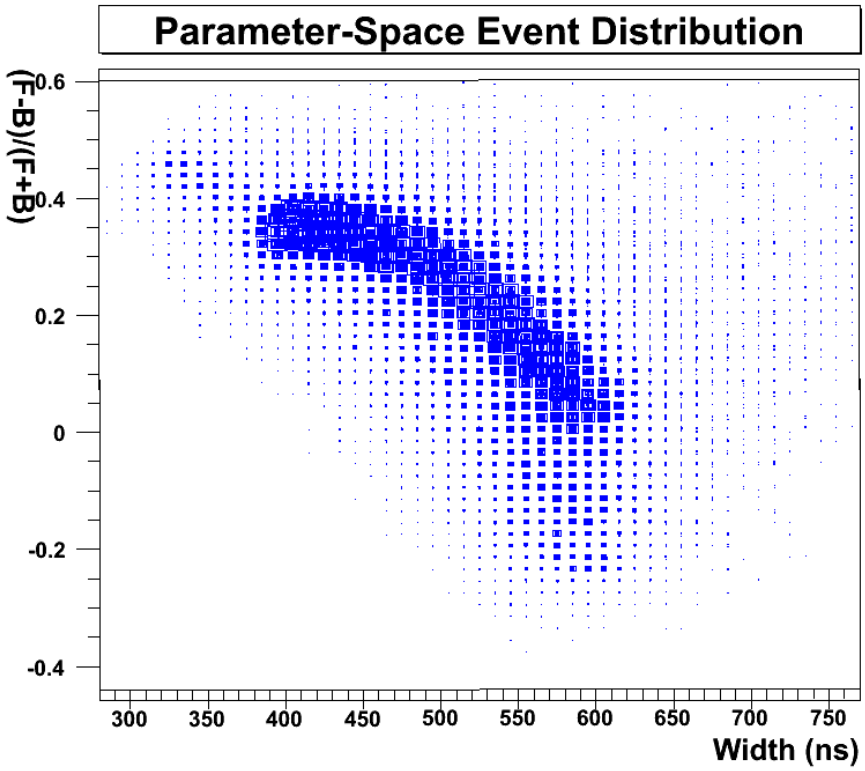

FIGURE 5.11. A two dimensional projection of the three dimensional parameter-space distribution corresponding to those events in the double-escape peak (DEP) energy region 1592 keV to 1595 keV. The data have been projected onto the pulse asymmetry vs. pulse width plane.

FOM? One would expect that the step-by-step FOM would be different based on order of operation, but the overall FOM should not be dependent upon order of operation. In this section the commutative nature of the segmentation and PSD cuts is examined.

5.3.1. Segmentation Followed by PSD. To begin the study of how the order of application of the cuts affects the figure of merit, the case of segmentation followed by PSD is examined. The result of the cuts for a 100^3 voxel parameter space are shown in Figure 5.17. The white histogram is the raw data, the yellow histogram is the residue after applying the single-segment-only segmentation cut, and the grey histogram is the result of applying the PSD cut to

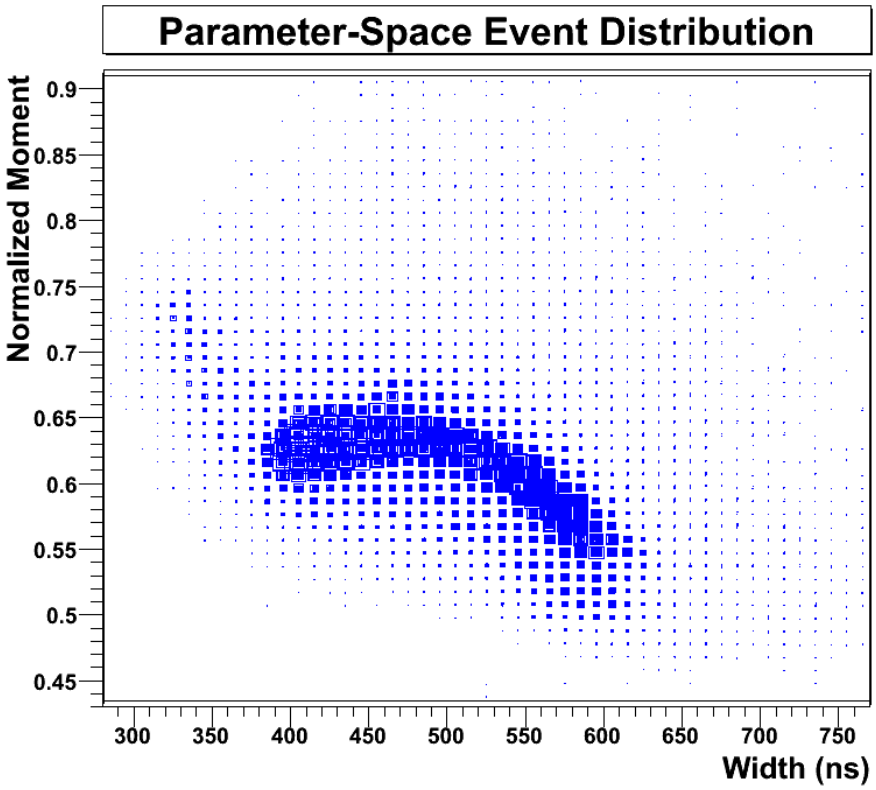

FIGURE 5.12. A two dimensional projection of the three dimensional parameter-space distribution corresponding to those events in the double-escape peak (DEP) energy region 1592 keV to 1595 keV. The data have been projected onto the normalized moment vs. pulse width plane.

the segmentation residue. These cuts were also applied to data defined by a parameter space of 125^3 voxels and the results are shown in Figure 5.18. A FOM was calculated for each cut individually as well as the cumulative (segmentation plus PSD) cut. These values are presented in Table 5.3. One should note the difference in the cumulative cut efficacy for the 100^3 voxel versus 125^3 voxel parameter space.

5.3.2. PSD Followed by Segmentation. It has just been shown that the granularity of the PSD parameter space has a significant impact on the cumulative FOM. The study of the affect on the FOM due to the order of application

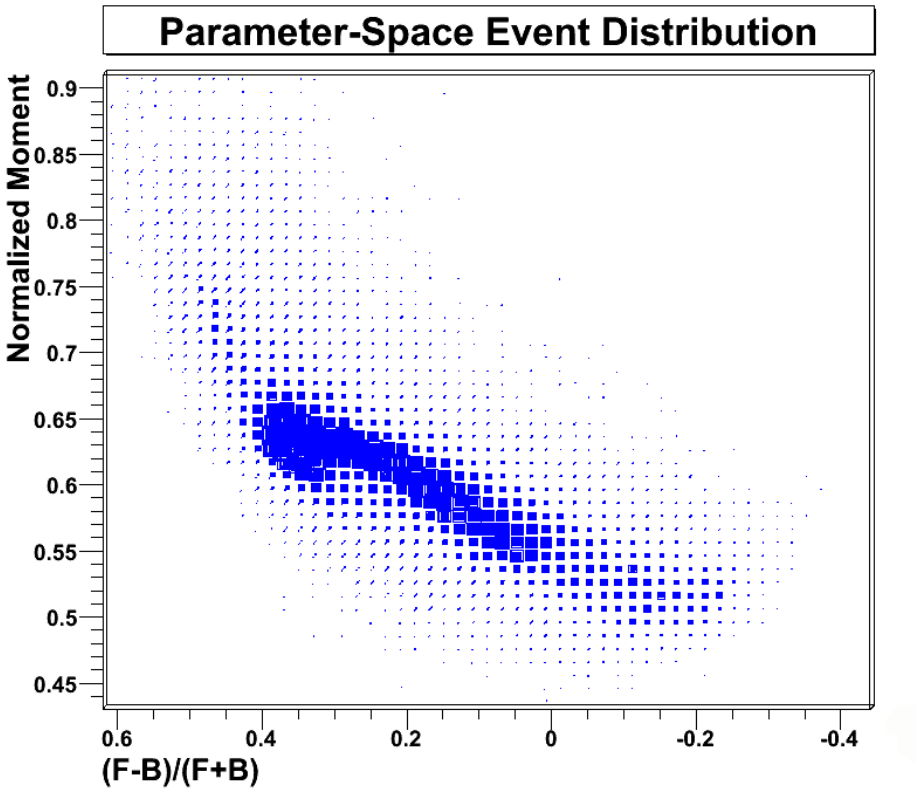

FIGURE 5.13. A two dimensional projection of the three dimensional parameter-space distribution corresponding to those events in the double-escape peak (DEP) energy region 1592 keV to 1595 keV. The data have been projected onto the normalized moment vs. pulse asymmetry plane.

TABLE 5.3. Table summarizing the figures of merit (FOMs) for individual and cumulative cuts. Here, the segmentation cut was applied first. The pulse-shape discrimination (PSD) cut was then applied to the segmentation residue. The cumulative FOM is the net result of both cuts.

	100^3 voxels		125^3 voxels	
Cut Type	FOM	Uncert	FOM	Uncert
Seg	1.428	$\pm$0.001	1.428	$\pm$0.002
PSD	1.193	$\pm$0.001	1.353	$\pm$0.002
Cumul	1.704	$\pm$0.001	1.933	$\pm$0.002

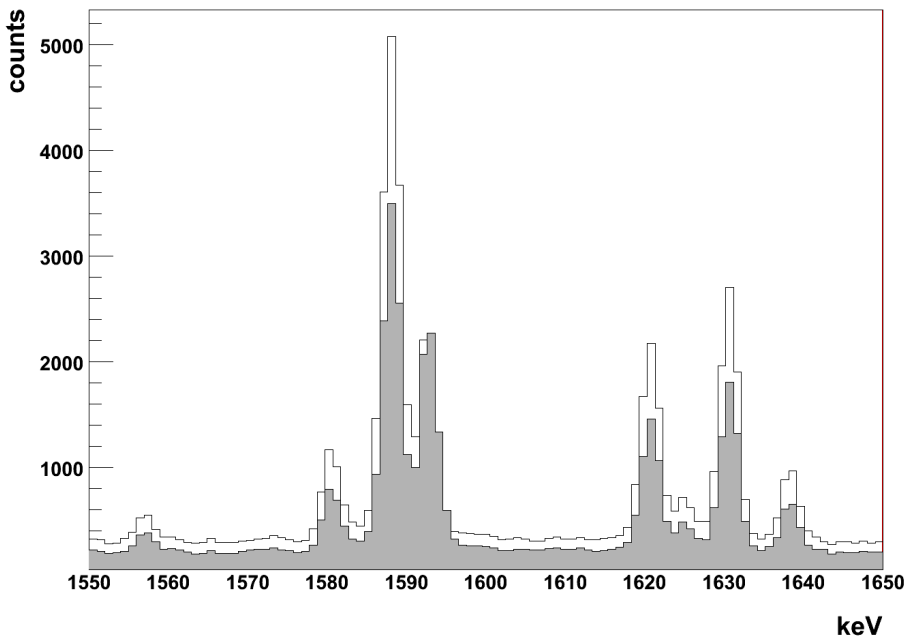

FIGURE 5.14. The result of applying a pulse-shape discrimination (PSD) cut. White histogram is raw (uncut) data. Grey histogram is what remains after PSD. (Details: SG order = 9, bins per axis = 100, acceptance fraction = 0.95)

of the cuts continues with the case of PSD followed by segmentation. The results of applying the cuts to the 100^3 voxel and 125^3 voxel parameter spaces are shown in Figures 5.19 and 5.20, respectively. The white histogram is the raw data, the grey histogram is the residue after applying the PSD cut, and the yellow histogram is the result of applying the segmentation cut to the PSD residue. Again, the FOM was calculated for each cut as well as the cumulative cut. These values are presented in Table 5.4. Again, one should note the marked improvement in the cumulative FOM for the 125^3 voxel parameter space versus the 100^3 voxel parameter space. Comparing the cumulative FOMs in Table 5.3 with the values in Table 5.4, one could argue that the difference in the FOMs is statistically significant and a segmentation cut followed by a PSD cut is more effective at reducing the background signal. However, only statistical error has been considered up to this point. If one uses the variation on the PSD cut efficacy for 100^3 voxel versus 125^3 voxel parameter space

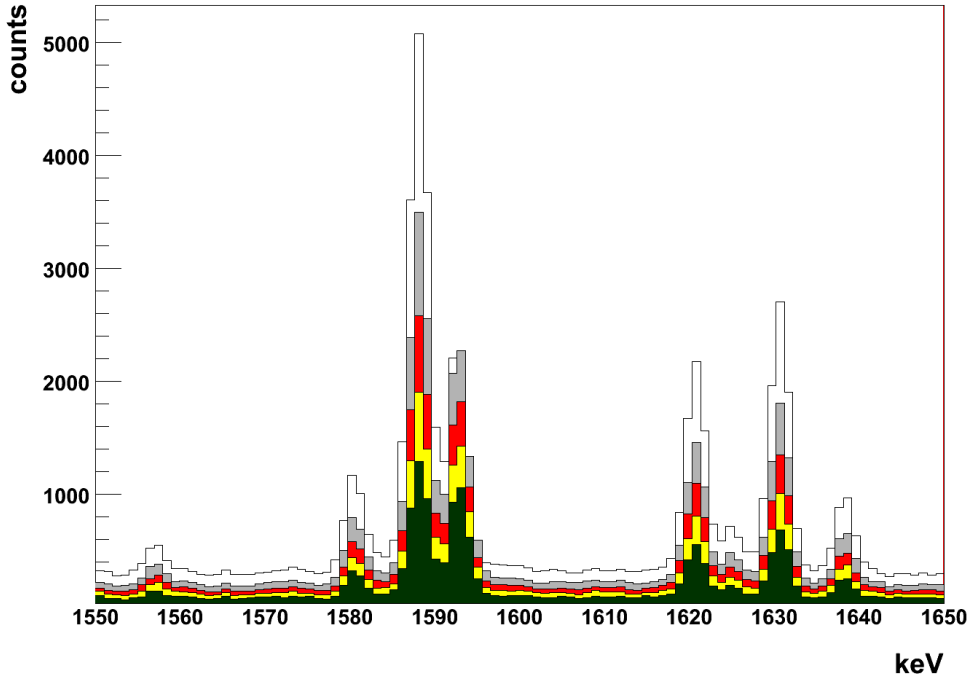

FIGURE 5.15. The results of applying a pulse-shape discrimination (PSD) cut with different parameter-space (PS) acceptance fractions (AF). The white histogram is raw (uncut) data. Grey histogram corresponds to a PS AF of 0.95. Red histogram corresponds to a PS AF of 0.75. Yellow histogram corresponds to a PS AF of 0.55. Green histogram corresponds to a PS AF of 0.45. (Details: SG order = 9, bins per axis = 100)

as a conservative estimate of the systematic uncertainty – $\sim$10% – then the cumulative FOMs are consistent regardless of the order in which the cuts are applied.

5.4. SUMMARY

In this chapter, the efficacy of segmentation and pulse shape discrimination analysis cuts for background reduction has been quantified. It was shown that the experimentally determined FOM for the rejection of ^{208}Tl is significantly less than what was predicted by simulation. Additionally, the PSD FOM was shown to be quite variable based on the parameters used to define the event

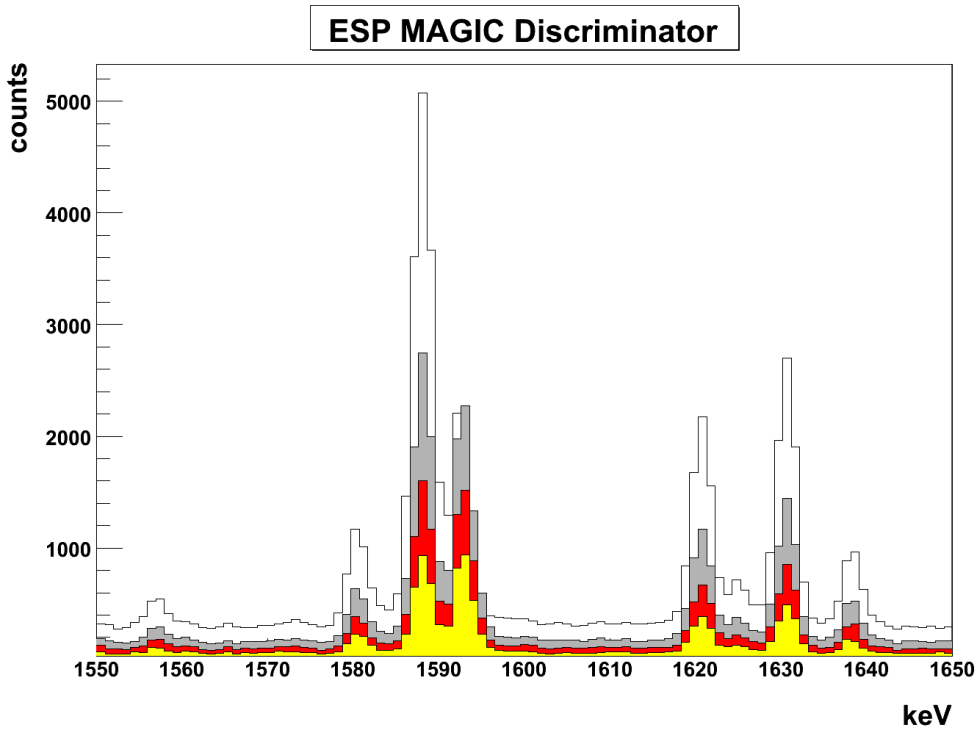

FIGURE 5.16. The results of applying a pulse-shape discrimination (PSD) cut with different parameter-space (PS) acceptance fractions (AF). The white histogram is raw (uncut) data. Grey histogram corresponds to a PS AF of 0.95. Red histogram corresponds to a PS AF of 0.65. Yellow histogram corresponds to a PS AF of 0.35. (Details: SG order = 9, bins per axis = 125)

TABLE 5.4. Table summarizing the figures of merit (FOMs) for individual and cumulative cuts. Here, the pulse-shape discrimination (PSD) cut was applied first. The segmentation cut was then applied to the PSD residue. The cumulative FOM is the net result of both cuts.

	100^3 voxels		125^3 voxels	
Cut Type	FOM	Uncert	FOM	Uncert
PSD	1.205	$\pm$0.001	1.360	$\pm$0.001
Seg	1.385	$\pm$0.001	1.378	$\pm$0.002
Cumul	1.669	$\pm$0.001	1.874	$\pm$0.002

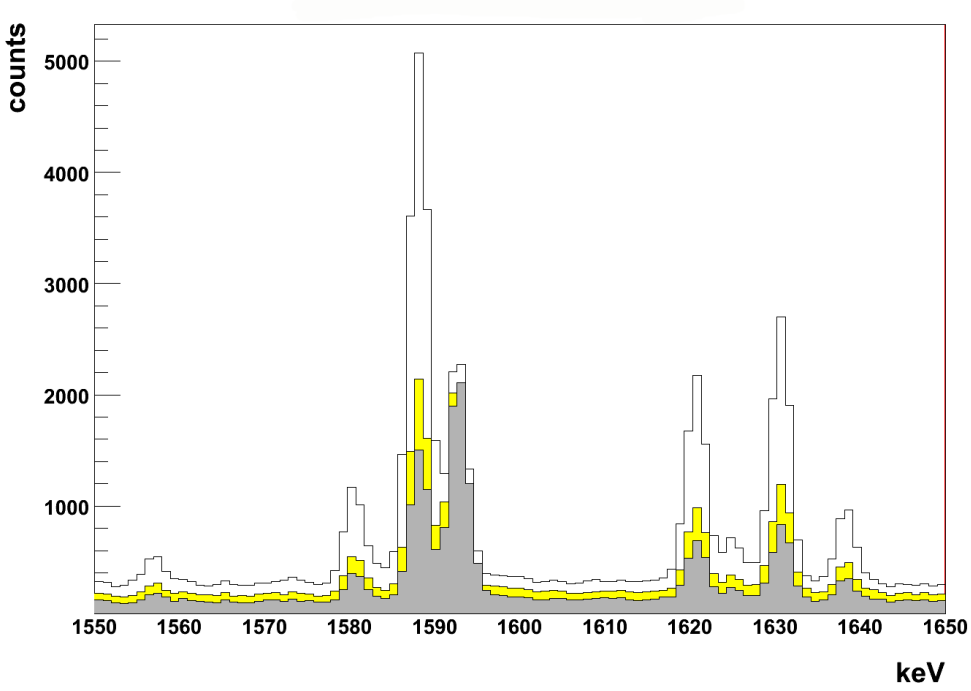

FIGURE 5.17. Result of applying a single-segment-only segmentation cut (yellow) followed by a pulse-shape discrimination (PSD) cut (grey). The PSD acceptance region is 100^3 voxels.

acceptance region. And finally, it was shown that to within systematic uncertainty, the order in which the individual cuts is applied does not change the overall FOM for the cumulative cut. In the next chapter, the impact on the sensitivity of a next-generation ^{76}Ge $0\nu\beta\beta$-decay experiment using a PSEG-type detector and implementing multi-parametric PSD is estimated and discussed.

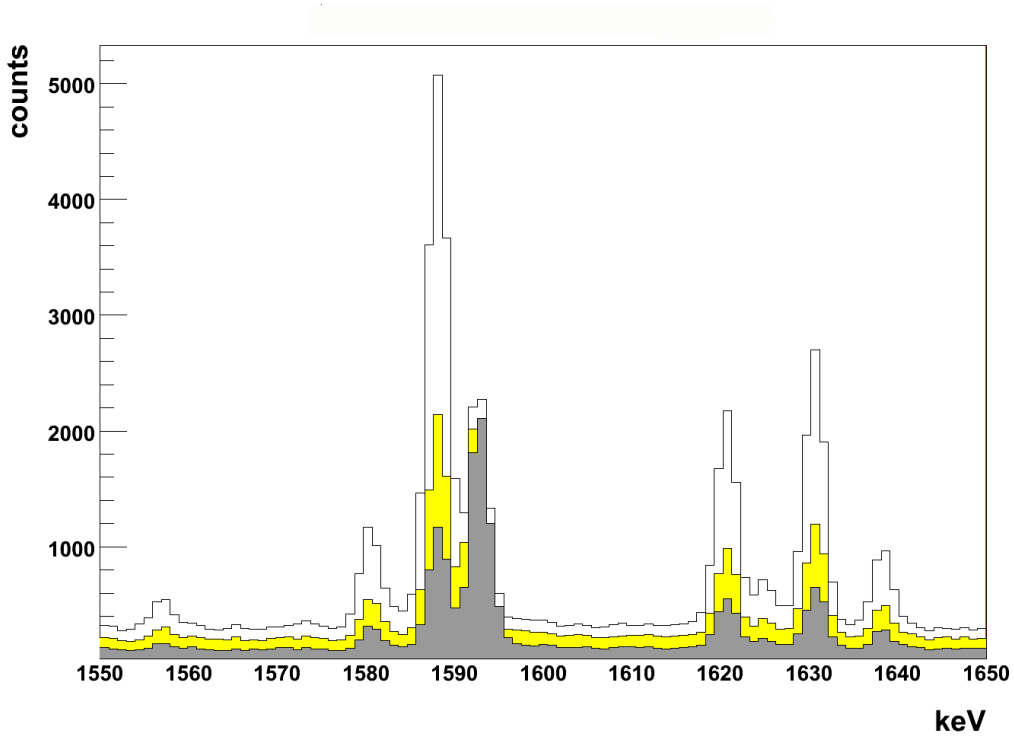

FIGURE 5.18. Result of applying a single-segment-only segmentation cut (yellow) followed by a pulse-shape discrimination (PSD) cut (grey). The PSD acceptance region is 125^3 voxels.

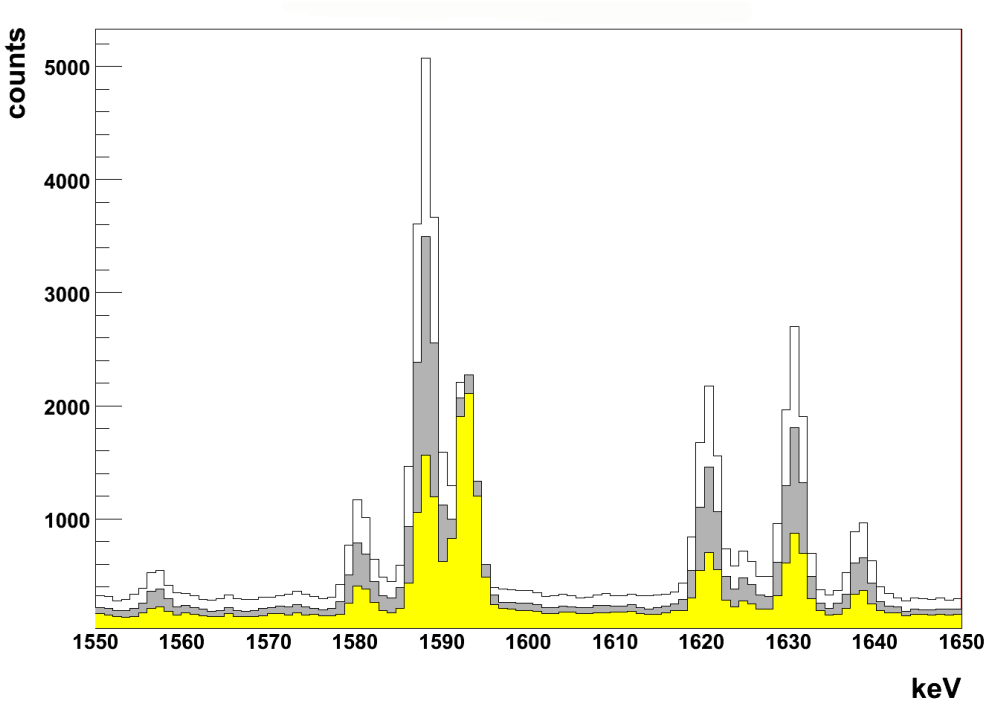

FIGURE 5.19. Result of applying a pulse-shape discrimination (PSD) cut (grey) followed by a single-segment-only segmentation cut (yellow). The PSD acceptance region is 100^3 voxels.

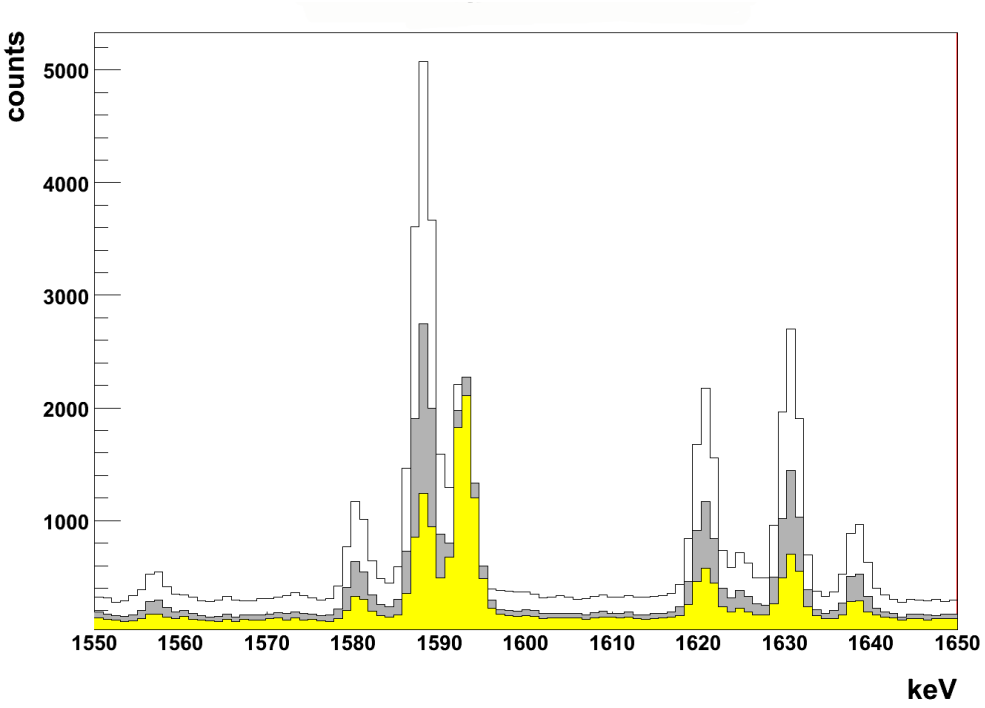

FIGURE 5.20. Result of applying a pulse-shape discrimination (PSD) cut (grey) followed by a single-segment-only segmentation cut (yellow). The PSD acceptance region is 125^3 voxels.

CHAPTER 6

IMPROVING THE PHYSICS IMPACT OF NEXT-GENERATION ^{76}GE DOUBLE-BETA DECAY EXPERIMENTS

In the previous chapter, details of the implementation of segmentation and pulse-shape discrimination cuts on PSEG data were presented and the efficacy of these cuts quantified. In this chapter, that information is used to estimate the impact on the $T^{0\nu}_{1/2}$and $\langle m_{\beta\beta}\rangle$sensitivity of a next generation ^{76}Ge neutrinoless double-beta decay experiment. Additionally, a practical matter surrounding the use of segmented detectors is discussed and the true impact on $T^{0\nu}_{1/2}$and $\langle m_{\beta\beta}\rangle$sensitivity is calculated.

6.1. QUANTIFYING $T^{0\nu}_{1/2}$IMPROVEMENT

As stated previously, the figure of merit (FOM) defined in equation 16 is a direct multiplier onto the $T^{0\nu}_{1/2}$discovery sensitivity of the experiment,

$$T^{0\nu}_{1/2}(n_\sigma) = \frac{4.16\times10^{26}y}{n_\sigma}\left(\frac{\varepsilon a}{W}\right)\sqrt{\frac{Mt}{b\Delta(E)}}$$

One could rewrite this equation as:

$$T^{0\nu}_{1/2}(n_\sigma) = \mathbf{FOM}\cdot\frac{4.16\times10^{26}y}{n_\sigma}\left(\frac{\varepsilon a}{W}\right)\sqrt{\frac{Mt}{b\Delta(E)}} \tag{22}$$

As a reminder – n_σ is the desired standard deviation of the measurement, ϵ is the event-detection efficiency, a is the isotopic abundance in the source material, W is the molecular weight of the source material, M is the total

mass of the source, t is the experiment live time, b is the background rate in counts/(keV kg y) before segmentation and PSD, and ΔE is the spectral resolution of the experiment – also called the ROI.

The cumulative FOM given in Table 5.3 for the 125^3-voxel parameter space is approximately 1.9. This means that by simply implementing these two analysis cuts, the half life sensitivity of a PSEG-based ^{76}Ge $0\nu\beta\beta$-decay experiment is nearly doubled. Additionally, for a fixed $T^{0\nu}_{1/2}$sensitivity, implementation of segmentation and PSD cuts is equivalent to having increased the mass (M) of the experiment by a factor of 3.6 or reduced the background (b) by a factor of 3.6.

To illustrate the impact of segmentation and PSD analysis cuts on a next-generation ^{76}Ge $0\nu\beta\beta$-decay experiment, consider the following. Such an experiment will have a mass (M) of 1000 kg and run for 10 years (t=10). Using the values of a = 0.86, W = 76, ΔE = 3.5 keV, a projected (before any cuts) background (b) of 0.001 counts/(keV kg yr), and an event identification efficiency of 95% (ϵ = 0.95), one could expect at the 3σ (99.73%) confidence level a $T^{0\nu}_{1/2}$sensitivity of:

$$T^{0\nu}_{1/2}(\mathbf{FOM} = 1) = 2.52 \times 10^{27}\ \mathbf{yr}$$

Using the segmentation plus PSD FOM of 1.9, the $T^{0\nu}_{1/2}$sensitivity becomes:

$$T^{0\nu}_{1/2}(\mathbf{FOM} = 1.9) = 4.78 \times 10^{27}\ \mathbf{yr}$$

In the following section, this $T^{0\nu}_{1/2}$sensitivity enhancement is used to predict the neutrino mass-range sensitivity of a next-generation ^{76}Ge $0\nu\beta\beta$-decay experiment.

6.2. Implications to Improving the Neutrino Mass Sensitivity

How does the $T^{0\nu}_{1/2}$sensitivity enhancement effect the neutrino mass ($\langle m_{\beta\beta}\rangle$) sensitivity of this next-generation experiment? From equation 14, we have:

$$\langle m_{\beta\beta}\rangle = m_e[T^{0\nu}_{1/2}F_N]^{-1/2} \tag{23}$$

where F_N is defined as:

$$F_N = G_{0\nu}(Q_{\beta\beta}, Z)|M_{0\nu}|^2 m_e^2 \tag{24}$$

As mentioned in section 1.2.2, there is a good deal of uncertainty in the value of the nuclear matrix element, $M_{0\nu}$, for all $0\nu\beta\beta$-decay candidate isotopes.[47] This uncertainty is propagated into the nuclear structure function, F_N.

Using the $T^{0\nu}_{1/2}$values calculated above (section 6.1) and three published values of F_N, the effective Majorana neutrino mass sensitivity of the experiment can be calculated. This calculation was performed for $F_N = 1.22^{+0.10}_{-0.11} \times 10^{-14}$ [44], $F_N = 4.29 \times 10^{-14}$ [41], and $F_N = 7.01 \times 10^{-14}$ [12]. Disregarding segmentation and PSD cuts (FOM=1), this results in a $\langle m_{\beta\beta}\rangle$sensitivity range of:

$$\langle m_{\beta\beta}\rangle = 38 - 92 \text{ meV} \tag{25}$$

An experiment using PSEG-type detectors and incorporating segmentation and PSD cuts (FOM=1.9) will have an improved $\langle m_{\beta\beta}\rangle$sensitivity of:

$$\langle m_{\beta\beta}\rangle = 29 - 69 \text{ meV} \tag{26}$$

A complete summary of the calculation results can be found in Table 6.1.

TABLE 6.1. Calculated values of $\langle m_{\beta\beta}\rangle$based on three different published values of the nuclear structure function, F_N.[44][41][12] The calculated $T^{0\nu}_{1/2}$values from section 6.1 have been used.

F_N (yr^{-1})	$\langle m_{\beta\beta}\rangle$(meV) for $T^{0\nu}_{1/2}$(FOM=1)	$\langle m_{\beta\beta}\rangle$(meV) for $T^{0\nu}_{1/2}$(FOM=1.9)
$1.22^{+0.10}_{-0.11} \times 10^{-14}$ [44]	92	69
4.29×10^{-14} [41]	49	37
7.01×10^{-14} [12]	38	29

6.3. RECOGNIZING A DECEPTIVE FIGURE OF MERIT

A very important detail has thus far been overlooked. While the calculations in sections 6.1 and 6.2 are correct, the segmentation plus PSD FOM of 1.9 must be tempered by reality. In instrumenting a segmented detector for a ^{76}Ge $0\nu\beta\beta$-decay experiment, it is necessary to locate the first stage of preamplification close to the germanium crystal. This is dictated by the minimum 25 MHz electronics bandwidth required for pulse-shape discrimination. The first stage of the preamplifier contains electronic components that are known to have trace radioactive impurities. These impurities are extremely difficult to mitigate and would contribute significantly to the background of an experiment. For example, the MAJORANA Collaboration expects that 90% of the background will come from "small parts" – front-end electronics. Using this value, one can go back to equation 22 and calculate the corrected or "true" figure of merit – FOM' – for a PSEG-based experiment utilizing segmentation and PSD cuts. For the 1000 kg example, the background (b) would increase by a factor of 5.5 – from 0.001 counts/(keV kg yr) to 0.0055 counts/(keV kg yr). Using the original segmentation plus PSD FOM of 1.9 and a new background of b=0.0055, the "true" FOM for the experiment would be FOM'=0.81. This is significant because it means the sensitivity of a PSEG-based experiment would

be reduced by 19% when compared to a comparable experiment using unsegmented detectors. The corresponding values of $T^{0\nu}_{1/2}$and $\langle m_{\beta\beta}\rangle$are then:

$$T^{0\nu}_{1/2}(\textbf{FOM} = 0.81) = 2.04 \times 10^{27}\ \textbf{yr}$$

and:

$$\langle m_{\beta\beta}\rangle = 43 - 102\ \textbf{meV} \tag{27}$$

The reduced neutrino mass sensitivity resulting from the increased background clearly shows that any advantage resulting from segmentation is more than eliminated. This conclusion is completely dependent upon the background model used by the MAJORANA Collaboration. If a method is developed to improve material purity of the electronic components, then the calculation must be revisited.

6.4. A NEWER DETECTOR FOR ^{76}GE DOUBLE-BETA DECAY

There is an interesting new development in the ^{76}Ge $0\nu\beta\beta$-decay community. Researchers at the University of Chicago have been working on a new type of germanium detector – p-type point contact (PPC) – for use in dark-matter and neutrino-scattering experiments.[7] This detector technology has been around for many years, however the use of low-background low-noise electronics is a new development. One of the primary advantages of this detector is the ability to determine the number of unique energy deposition locations within the crystal by simply counting the number of times that charge arrives at the point contact. No complex multi-parametric PSD or segmentation is required. Using the same calculation for the FOM that was used throughout this work, the experimentally determined PPC FOM is 2.68.[7] This would correspond to a $T^{0\nu}_{1/2}$and $\langle m_{\beta\beta}\rangle$sensitivity improvement for our example experiment of:

$$T^{0\nu}_{1/2}(\textbf{FOM} = 2.68) = 6.75 \times 10^{27}\ \textbf{yr}$$

and:

$$\langle m_{\beta\beta} \rangle = 23 - 56 \text{ meV} \tag{28}$$

This exciting result implies a physics reach down into the normal hierarchy region of neutrino parameter space.

Due to the simplicity of the analysis and the overall decrease in experimental complexity (ie. fewer signal cables and electronics) p-type point contact detectors should be considered for use in next-generation experiments. One downside that currently exists with this type of detector is the limited size a detector can be made and still efficiently collect the charge. Research with PPC detectors is currently being conducted by several members of the MAJORNA Collaboration.

6.5. SUMMARY AND CONCLUSION

In this chapter the impact of implementing segmentation and pulse-shape discrimination cuts to improve the sensitivity of a PSEG-based next-generation ^{76}Ge $0\nu\beta\beta$-decay experiment have been explored. It was shown that these two analysis cuts can improve the $T^{0\nu}_{1/2}$sensitivity of such an experiment by 90%. However, when one includes the practical aspect of having to instrument the added segments using electronics with radioactive impurities, the $T^{0\nu}_{1/2}$sensitivity of the experiment is reduced by 19%.

This has extremely important consequences for planned next-generation experiments since both active collaborations, MAJORANA and GERDA, initially planned to, and still may, use some or all segmented detectors to mitigate backgrounds. For many years now, these two collaborations strongly advocated the use of highly-segmented germanium detectors. Based upon the research in this document, it is the strong opinion of the author that implementation of even modestly-segmented germanium detectors can not be justified when considering the current radioactive impurity level of front-end electronics. Without an

intensive research effort to improve the radioactive cleanliness of these components, the use of segmented germanium detectors in a next-generation ^{76}Ge $0\nu\beta\beta$-decay experiment should be abandoned. At present, the only reasonable conclusion that can be reached is that either unsegmented semi-coaxial p-type or p-type point contact detectors should be considered for a next-generation experiment.

While this research has shown that segmented germanium detectors are not a suitable choice for a next-generation ^{76}Ge $0\nu\beta\beta$-decay experiment, the technology of a physically-segmented p-type germanium detector has proven itself, thus far, to be a useful and practical tool in modern nuclear physics. The technology of the PSEG detector deserves further consideration and development. One potential application for this technology is in the analysis of fission products. Exploiting the unique coincidence signatures found in nearly all fission products to increase the signal-to-background ratio, a researcher can detect and quantify low-activity isotopes that were previously obscured in background interferences.

BIBLIOGRAPHY

[1] Craig E. Aalseth. Germanium spectrometer pulse-shape discrimination for germanium-76 double-beta decay. Technical report, University of South Carolina, PhD Dissertation, 2000.

[2] I. Abt, A. Caldwell, K. Kröninger, J. Liu, X. Liu, and B. Majorovits. Pulse shapes from electron and photon induced events in segmented high-purity germanium detectors. *The European Physical Journal C*, 52(1):19–27, Sep 2007.

[3] B. Ananthanarayan and Ritesh K. Singh. Direct observation of neutrino oscillations at the sudbury neutrino observatory. *Current Science*, 83:553, 2002.

[4] F. T. Avignone III, G. S. King III, and Yu. G. Zdesenko. Next generation double-beta decay experiments: metrics for their evaluation. *New Journal of Physics*, 7:6, 2005.

[5] Frank T. Avignone III, Steven R. Elliott, and Jonathan Engel. Double beta decay, majorana neutrinos, and neutrino mass. *Reviews of Modern Physics*, 80(2), 2008.

[6] A. S. Barabash. Double-beta decay to the excited states (experiment). *Czechoslovak Journal of Physics*, 50(4):447–453, 04 2000/04/21/.

[7] P. S. Barbeau, J. I. Collar, and O. Tench. Large-mass ultralow noise germanium detectors: performance and applications in neutrino and astroparticle physics. *Journal of Cosmology and Astroparticle Physics*, 2007(09):009, 2007.

[8] H. A. Bethe and R. F. Bacher. Nuclear physics a. stationary states of nuclei. *Rev. Mod. Phys.*, 8(2):82, Apr 1936.

[9] Felix Boehm and Petr Vogel. *Physics of Massive Neutrinos, Second Edition*. Cambridge University Press, 1992.

[10] D. Budjáš, M. Barnabé Heider, O. Chkvorets, S. Schönert, and N. Khanbekov. Pulse shape analysis with a broad-energy germanium detector for

the gerda experiment. *ArXiv e-prints*, Dec 2008.

[11] David O. Caldwell, editor. *Current Aspects of Neutrino Physics*. Springer, 2001.

[12] O. Civitarese and J. Suhonen. Light-neutrino mass spectrum, nuclear matrix elements, and the observability of neutrinoless [beta][beta] decay. *Nuclear Physics A*, 729(2-4):867 – 883, 2003.

[13] W. Coburn, S. E. Boggs, S. Amrose, R. P. Lin, M. T. Burks, M. Amman, P. N. Luke, N. W. Madden, and E. L. Hull. Results of charge sharing tests in a ge-strip detector. *Nuclear Science Symposium Conference Record, 2001 IEEE*, 1:226–229 vol.1, 2001.

[14] The GERDA Collaboration. Technical proposal.

[15] The Gretina Collaboration. Proposal for Gretina. Technical report, Argonne National Laboratory, Lawrence Berkley National Laboratory, Michigan State University, Oak Ridge National Laboratory, Washington University, 2003.

[16] The KATRIN Collaboration. http://www-ik.fzk.de/ katrin/index.html.

[17] The KATRIN Collaboration. Design report 2004. Technical report, Forschungszentrum Karlsruhe, Universität Mainz, Institute for Nuclear Research, University of Washington, Massachusetts Institute of Technology, University of Wales, CCLRC Daresbury Laboratory, University College London, Nuclear Physics Institute - Prague, Fachhochschule Fulda, Universität Karlsruhe, Universität Münster, Universität Bonn, Joint Institute for Nuclear Research, 2005.

[18] The Majorana Collaboration. The proposed MAJORANA ^{76}Ge double-beta decay experiment. http://majorana.pnl.gov.

[19] The Majorana Collaboration. Draft proposal for the majorana zero-neutrino double-beta decay experiment. Technical report, Brown University, Institute for Theoretical and Experimental Physics, Joint Institute for Nuclear Research, Lawrence Berkley National Laboratory, Lawrence Livermore National Laboratory, Los Alamos National Laboratory, Oak Ridge National LAboratory, Osaka University, Pacific Northwest NAtional Laboratory, Queen's University, Traingle University Nuclear LAboratory, University of Chicago, University of South Carolina, University of Tennessee, University of Washington, 2004.

[20] The Majorana Collaboration. Overview of the majorana neutrinoless double-beta decay experiment. Technical report, Brown University, Institute for Theoretical and Experimental Physics, Joint Institute for Nuclear Research, Lawrence Berkley National Laboratory, Lawrence Livermore National Laboratory, Los Alamos National Laboratory, Oak Ridge National LAboratory, Osaka University, Pacific Northwest NAtional Laboratory, Queen's University, Traingle University Nuclear LAboratory, University of Chicago, University of South Carolina, University of Tennessee, University of Washington, 2005.

[21] M. A. Deleplanque, I. Y. Lee, K. Vetter, G. J. Schmid, F. S. Stephens, R. M. Clark, R. M. Diamond, P. Fallon, and A. O. Macchiavelli. Greta: utilizing new concepts in gamma-ray detection. *Nuclear Instruments and Methods in Physics Research Section A: Accelerators, Spectrometers, Detectors and Associated Equipment*, 430(2-3):292 – 310, 1999.

[22] M. Descovich, P. J. Nolan, A. J. Boston, J. Dobson, S. Gros, J. R. Cresswell, J. Simpson, I. Lazarus, P. H. Regan, J. J. Valiente-Dobon, P. Sellin, and C. J. Pearson. The position response of a large-volume segmented germanium detector. *Nuclear Instruments and Methods in Physics Research Section A: Accelerators, Spectrometers, Detectors and Associated Equipment*, 553(3):512–521, 11 2005/11/21.

[23] Guilhem Douysset, Tomas Fritioff, Conny Carlberg, Ingmar Bergström, and Mikael Björkhage. Determination of the ^{76}Ge double beta decay Q value. *Phys. Rev. Lett.*, 86(19):4259–4262, May 2001.

[24] J. I. Collar H. S. Miley E. Garcia A. Morales J. Morales R. Nuñez-Lagos J. H. Reeves C. Saenz F. T. Avignone III, R. L. Brodzinski and J. I. Villar. Theoretical and experimental investigation of cosmogenic radioisotope production in germanium. *Nuclear Physics B, Proceedings Supplements*, 28A:280–285, 1992.

[25] Enrico Fermi. Versuch einer theorie der beta-strahlen i. *Zeitschrift für Physik*, 88:161, 1934.

[26] Ettore Fiorini and et.al. A search for lepton non-conservation in double beta decay with a germanium detector. *Physics Letters*, 25:602–603, 1967.

[27] Richard B. Firestone and Virginia S. Shirley. *Table of Isotopes, Eigth Edition*. Wiley-Interscience, 1998.

[28] Y. Fukuda and et. al. Evidence for oscillation of atmospheric neutrinos. *Physical Review Lettters*, 81(8):1562–1567, 1998.

[29] D. González and et. al. Pulse shape discrimination in the igex experiment. *Nuclear Instruments and Methods in Physics Research Section A*, 515(3):634–643, 2003.

[30] W. Hennig, Y.X. Chu, H. Tan, A. Fallu-Labruyere, W.K. Warburton, and R. Grzywacz. The dgf pixie-4 spectrometer - compact digital readout electronics for HPGe clover detectors. *Nuclear Instruments and Methods in Physics Research Section B: Beam Interactions with Materials and Atoms*, 263(1):175 – 178, 2007.

[31] Bradley Hubbard-Nelson, Michael Momayezi, and William K. Warburton. A module for energy and pulse shape data acquisition. *Nuclear Instruments and Methods in Physics Research Section A: Accelerators, Spectrometers, Detectors and Associated Equipment*, 422(1-3):411 – 416, 1999.

[32] Ethan L. Hull, Richard H. Pehl, James R. Lathrop, Gregory N. Martin, R. B. Mashburn, Harry S. Miley, Craig E. Aalseth, and Todd W. Hossbach. Segmentation of the outer contact on p-type coaxial germanium detectors. In *Proceedings of the 29th Monitoring Research Review: Ground-Based Nuclear Explosion Monitoring Technologies*, 2006.

[33] G. S. King III, F. T. Avignone III, C. E. Cox, T. W. Hossbach, W. Jennings, and J. H. Reeves. Pulse shape discrimination in the igex experiment. *Nuclear Instruments and Methods in Physics Research Section A: Accelerators, Spectrometers, Detectors and Associated Equipment*, 595:599–604, 2008.

[34] George S. King III. *New segmented p-type germanium detector for neutrino-less double-beta decay*. PhD thesis, University of South Carolina, 2006.

[35] Th. Kröll, I. Peter, Th. W. Elze, J. Gerl, Th. Happ, M. Kaspar, H. Schaffner, S. Schremmer, R. Schubert, K. Vetter, and H. J. Wollersheim. Analysis of simulated and measured pulse shapes of closed-ended HPGe detectors. *Nuclear Instruments and Methods in Physics Research Section A: Accelerators, Spectrometers, Detectors and Associated Equipment*, 371(3):489 – 496, 1996.

[36] Michael F. L'Annunziata. *Radioactivity: Introduction and History*. Elsevier Science, 2007.

[37] B. Majorovits and H.V. Klapdor-Kleingrothaus. Digital pulseshape analysis by neural networks for the heidelberg-moscow-double-beta-decay-experiment. *The European Physical Journal A*, 6(4):463–469, dec 1999.

[38] Kenneth G. McKay. A germanium counter. *Phys. Rev.*, 76(10):1537, Nov 1949.

[39] G. L. Miller, W. M. Gidson, and P. F. Donovan. Semiconductor particle detectors. *Annual Review of Nuclear Science*, 12(1):189–220, 1962.

[40] L. Nelson, M.R. Dimmock, A.J. Boston, H.C. Boston, J.R. Cresswell, P.J. Nolan, I. Lazarus, J. Simpson, P. Medina, C. Santos, and C. Parisel. Characterisation of an agata symmetric prototype detector. *Nuclear Instruments and Methods in Physics Research Section A: Accelerators, Spectrometers, Detectors and Associated Equipment*, 573(1-2):153 – 156, 2007. Proceedings of the 7th International Conference on Position-Sensitive Detectors - PSD-7, 7th International Conference on Position-Sensitive Detectors.

[41] A. Poves, E. Caurier, and F. Nowacki. Presented at Neutrinos and Dark Matter, Paris, France, 2006.

[42] Bogdan Povh, Klaus Rith, Christoph Scholz, and Frank Zetsche. *Particles and Nuclei, Fifth Edition*. Springer, 2006.

[43] William H. Press, Saul A. Teukolsky, William T. Vetterling, and Brian P. Flanery. *Numerical Recipes in C*. Cambridge University Press, second edition, 1988.

[44] V.A. Rodin, Amand Faessler, F. Simkovic, and Petr Vogel. Assessment of uncertainties in QRPA $0\nu\beta\beta$-decay nuclear matrix elements. *Nuclear Physics A*, 766:107 – 131, 2006.

[45] Pat Sangsingkeow, Kevin D. Berry, Edward J. Dumas, Thomas W. Raudorf, and Teresa A. Underwood. Advances in germanium detector technology. *Nuclear Instruments and Methods in Physics Research Section A: Accelerators, Spectrometers, Detectors and Associated Equipment*, 505(1-2):183 – 186, 2003. Proceedings of the tenth Symposium on Radiation Measurements and Applications.

[46] P. Sangsingkeow (Ortec). Private communication.

[47] Fedor Simkovic, Amand Faessler, Herbert Muther, Vadim Rodin, and Markus Stauf. The $0\nu\beta\beta$-decay nuclear matrix elements with self-consistent short-range correlations. *ArXiv e-prints*, 2009.

[48] T. Tomoda. Double beta decay. *Reports on Progress in Physics*, 54(1):53–126, 1991.

[49] Kai Vetter. Recent developments in the fabrication and operation of germanium detectors. *Annual Review of Nuclear and Particle Science*, 57(1):363–404, 2007.

[50] C. F. v. Weizsäcker. Zur theorie der kernmassen. *Zeitschrift für Physik A Hadrons and Nuclei*, 96(7):431–458, 1935.

APPENDIX A

PSEG CRYOSTAT DESIGN SPECIFICATIONS

The following is a complete set of measured drawings used to construct the PSEG cryostat.

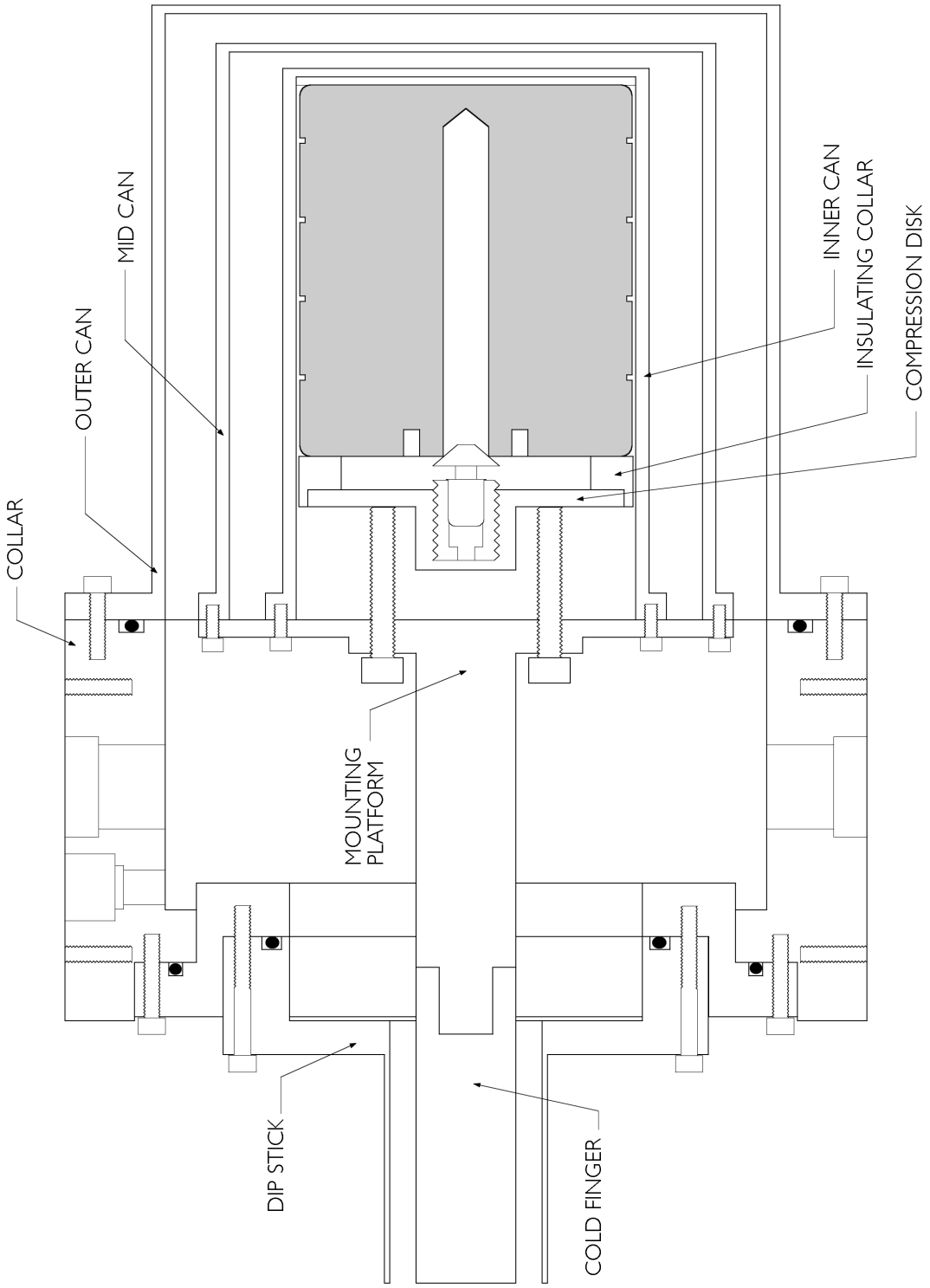
COLLAR
OUTER CAN
MID CAN
INNER CAN
INSULATING COLLAR
COMPRESSION DISK
MOUNTING PLATFORM
DIP STICK
COLD FINGER

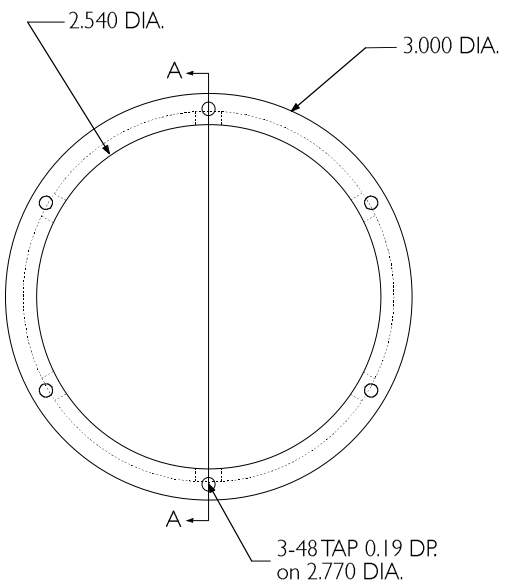

BOTTOM

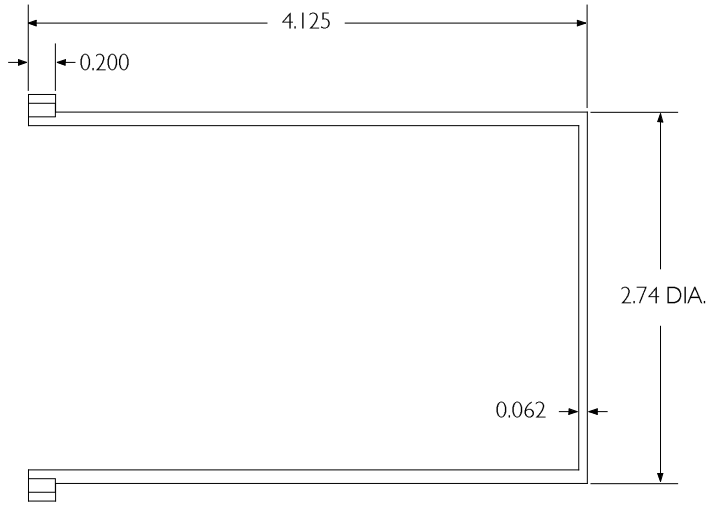

SECTION A-A

INNER CAN
ALUMINUM
MEASURMENTS IN INCHES

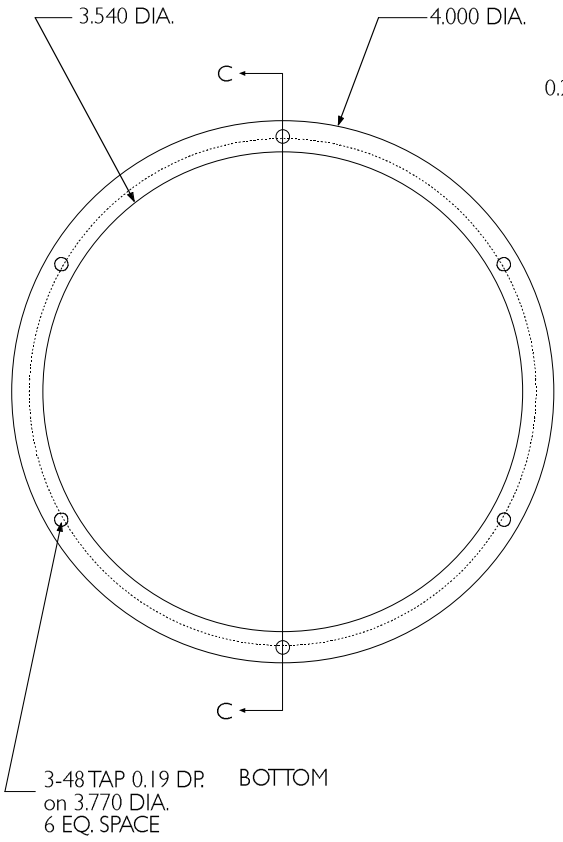

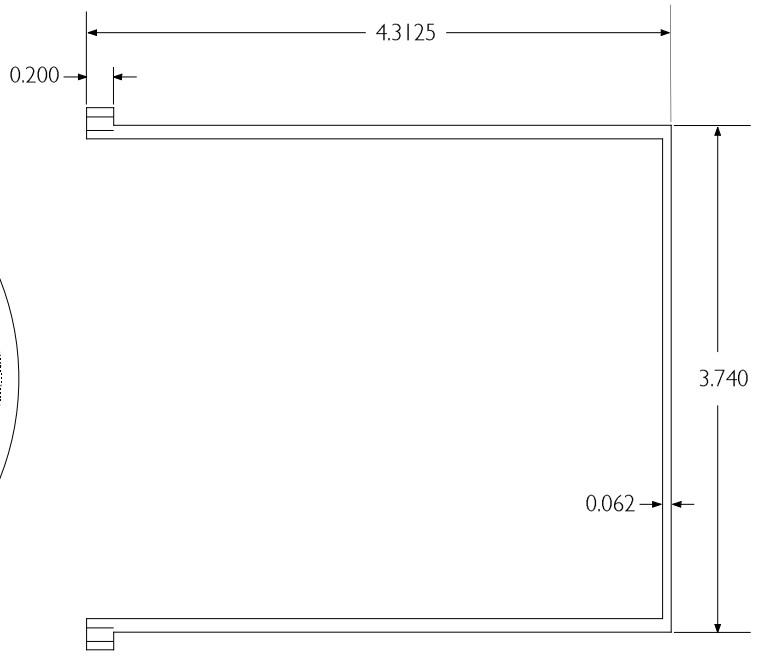

SECTION C-C

MID-CAN
ALUMINUM
MEASUREMENTS IN INCHES

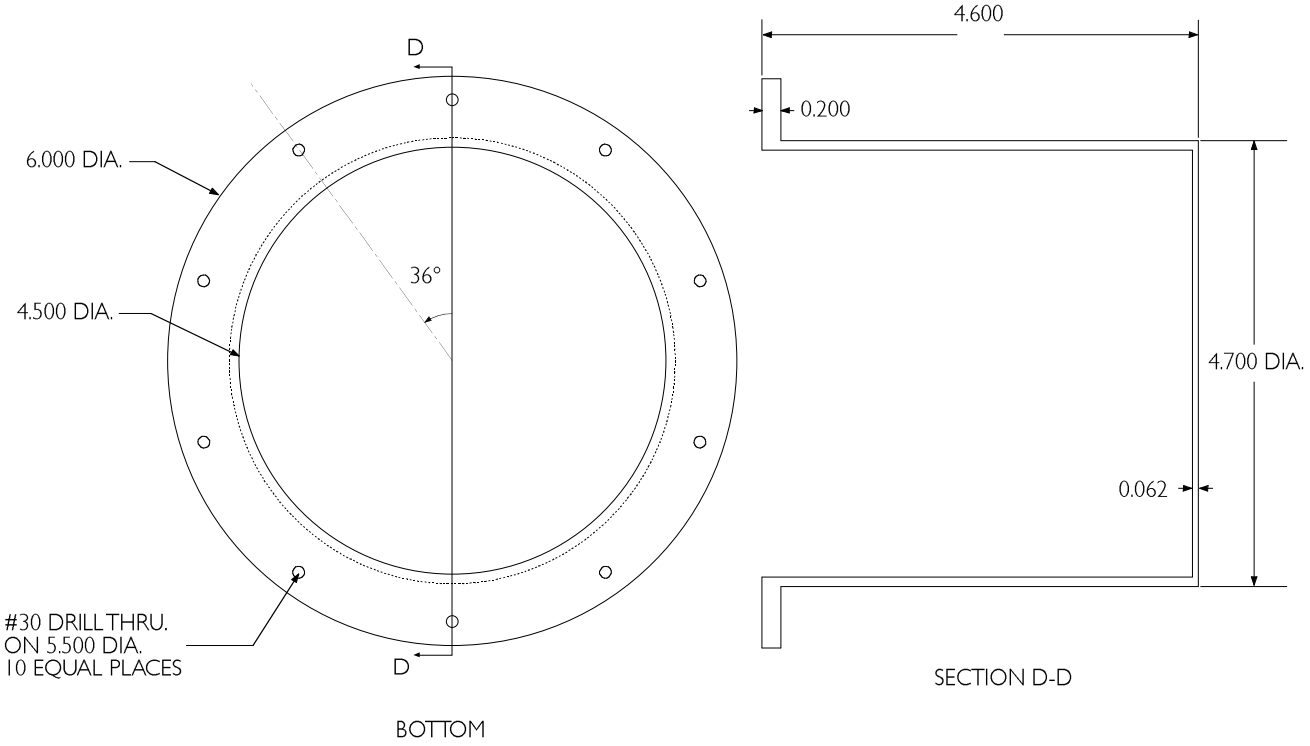

OUTER CAN
ALUMINUM
MEASUREMENTS IN INCHES

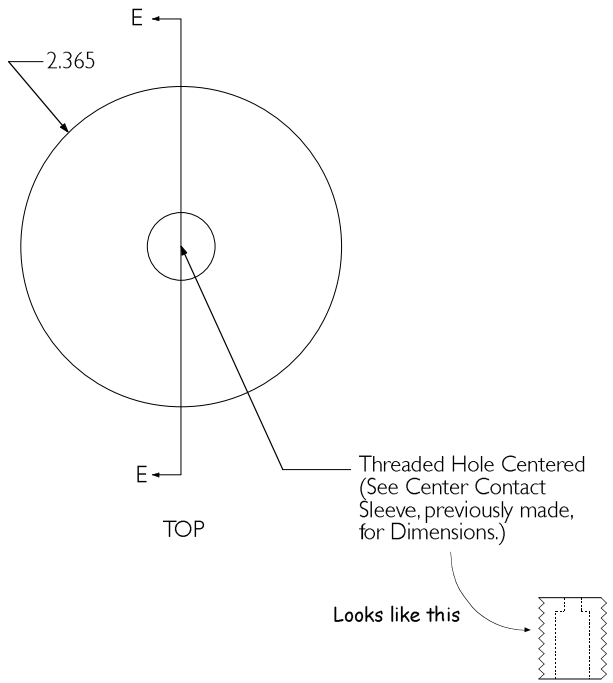

TOP

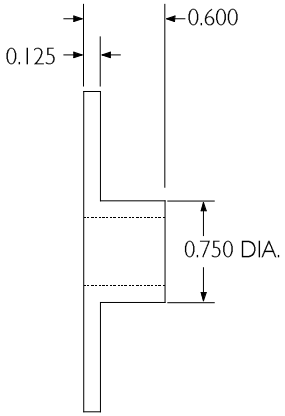

SECTION E-E

COMPRESSION DISK
ALUMINUM
MEASUREMENTS IN INCHES

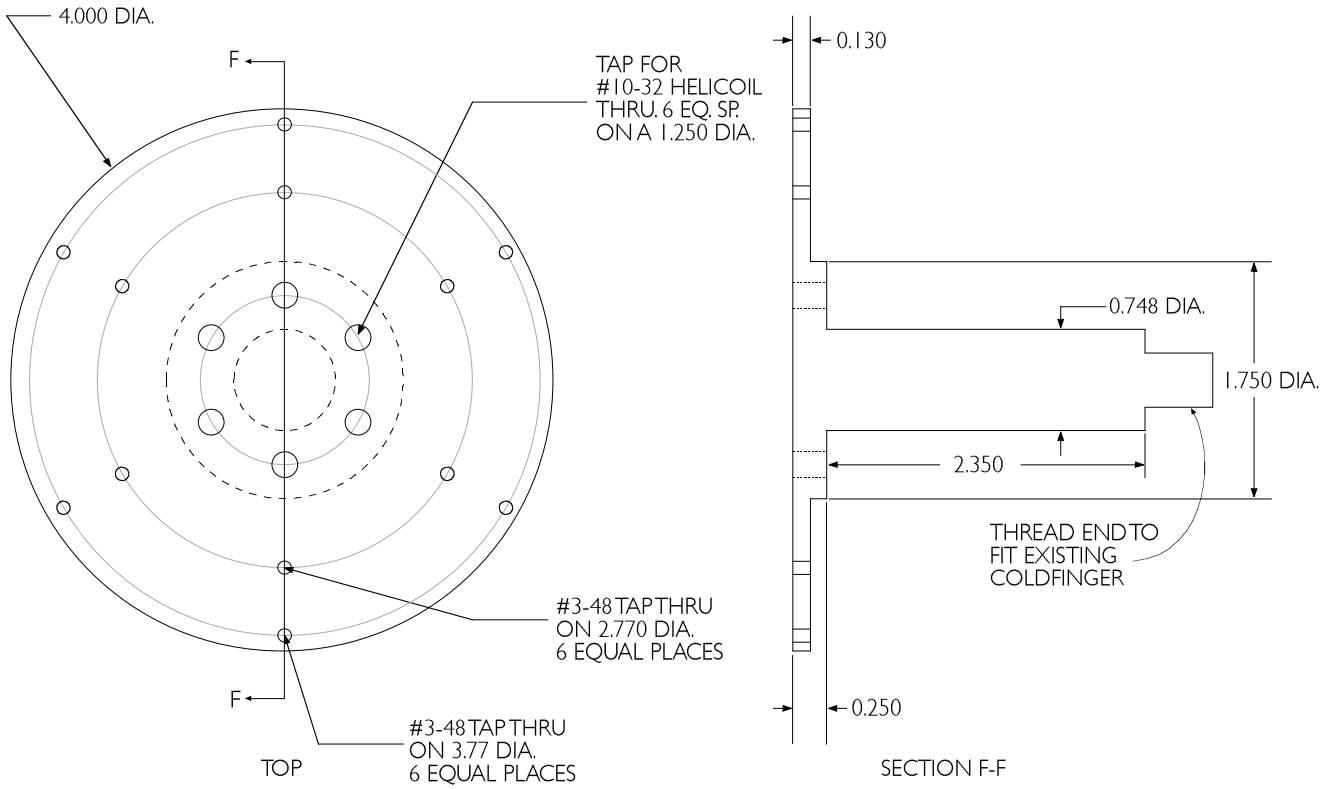

MOUNTING PLATFORM
ALUMINUM
MEASURMENTS IN INCHES

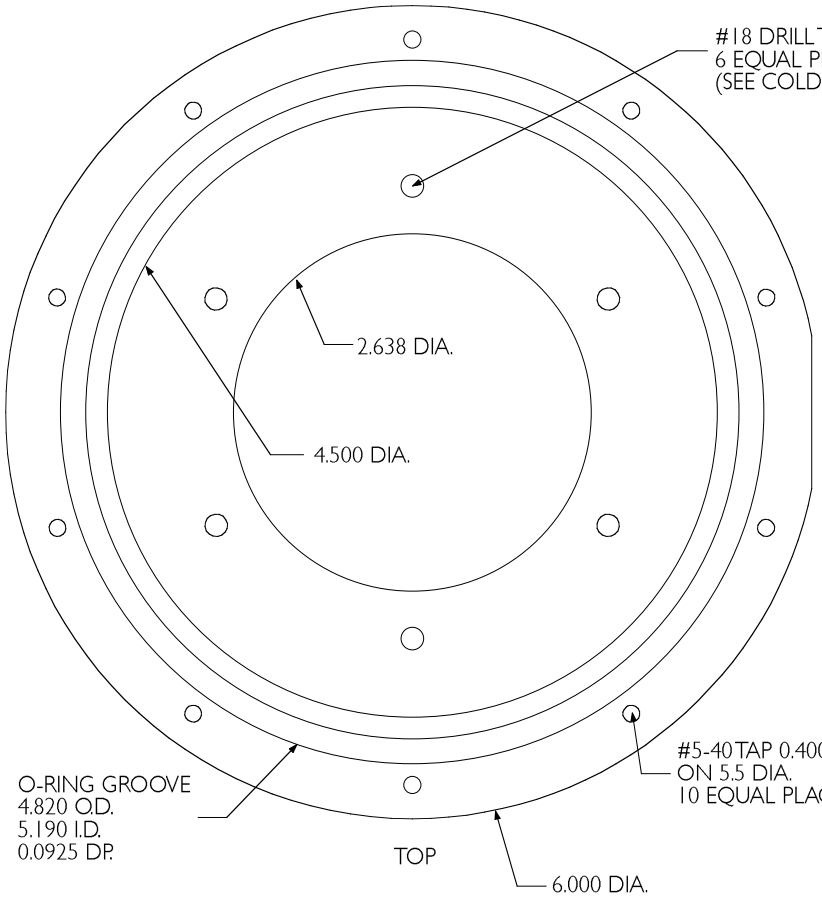

COLLAR
ALUMINUM (6061)
MEASURMENTS IN INCHES

ELECTRONICS
CONNECTION
PORT TYPE I
VACUUM PORT
ELECTRONICS
CONNECTION
PORT TYPE II
(5 EQ. SPACED)
COLLAR
ALUMINUM
MEASURMENTS IN INCHES
60°
TOP

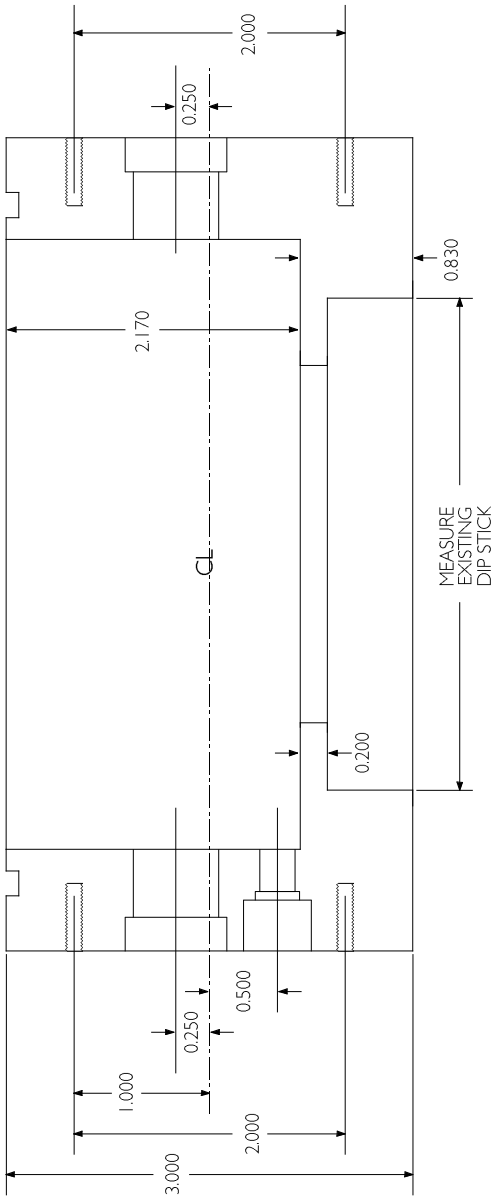

COLLAR (SECTION)
ALUMINUM
MEASURMENTS IN INCHES

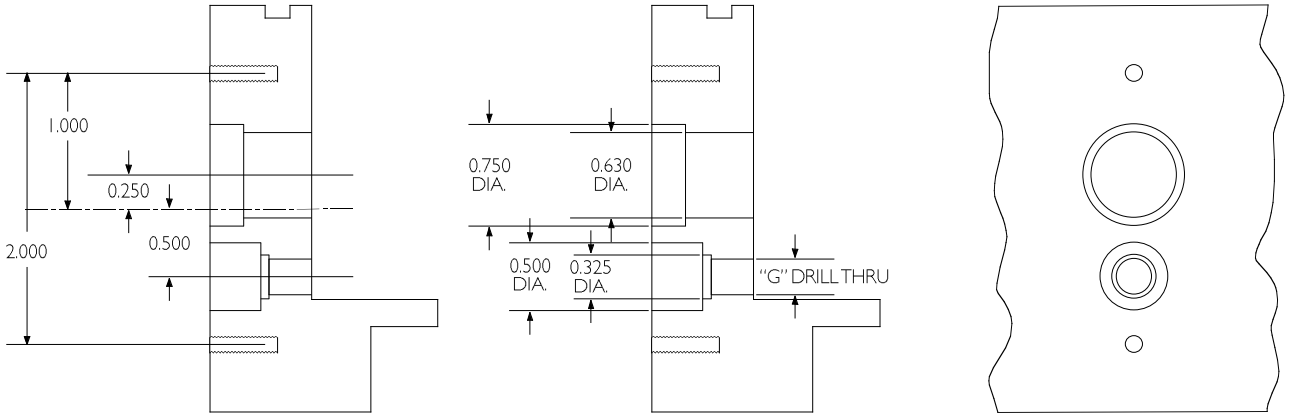

SECTION
(POSITIONS)

SECTION
(DIAMETERS)

SIDE

COLLAR
ELECTRONICS
CONNECTION
PORT TYPE I

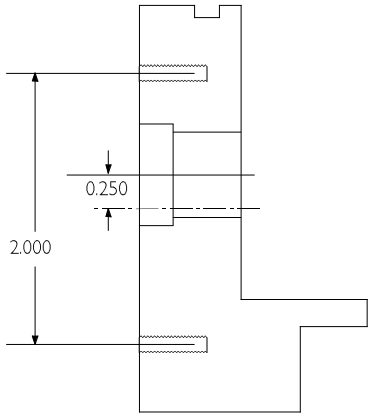

SECTION
(POSITIONS)

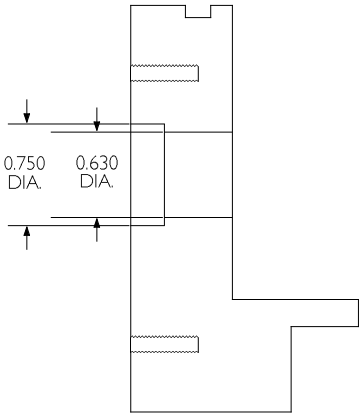

SECTION
(DIAMETERS)

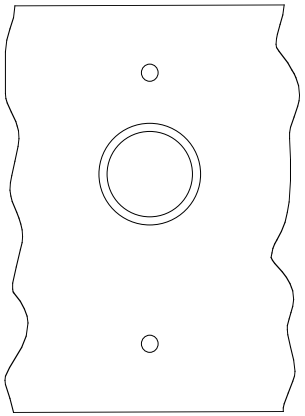

SIDE

ELECTRONICS
CONNECTION
PORT TYPE II

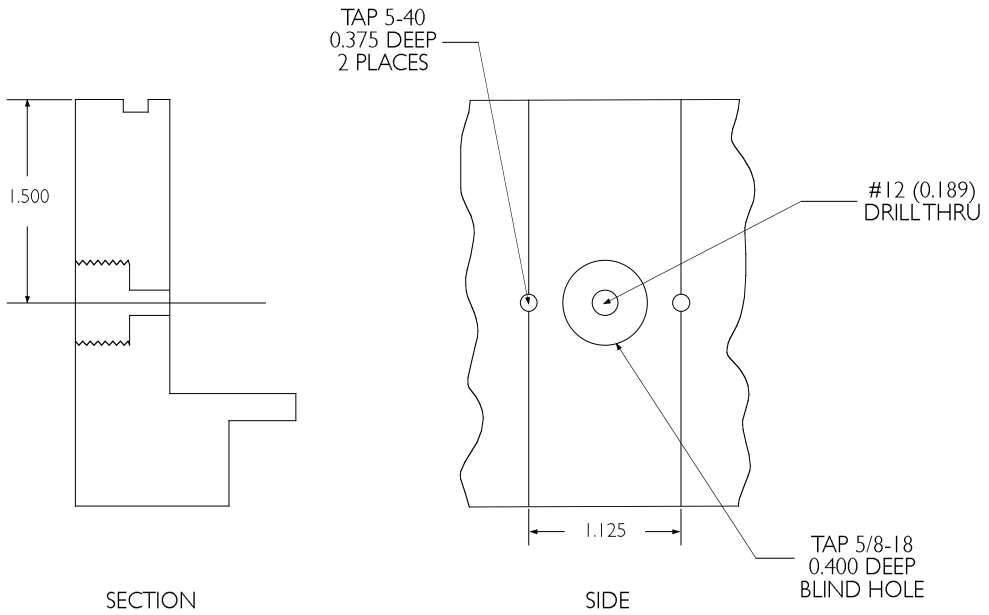

COLLAR VACUUM PORT

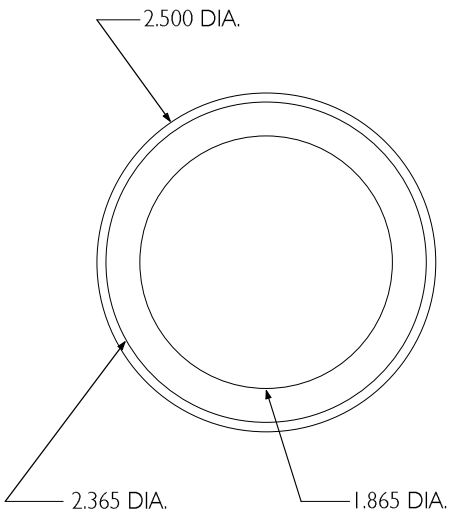

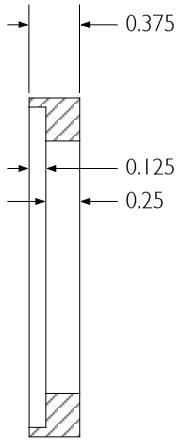

INSULATING RING
VIRGIN ELECTRICAL GRADE PTFE
MEASUREMENTS IN INCHES

TOP INSULATOR DISK
4 Each
VIRGIN ELECTRICAL GRADE PTFE
MEASUREMENTS IN INCHES

MODIFIED COLLAR
(SECTION)
ALUMINUM
MEASURMENTS IN INCHES

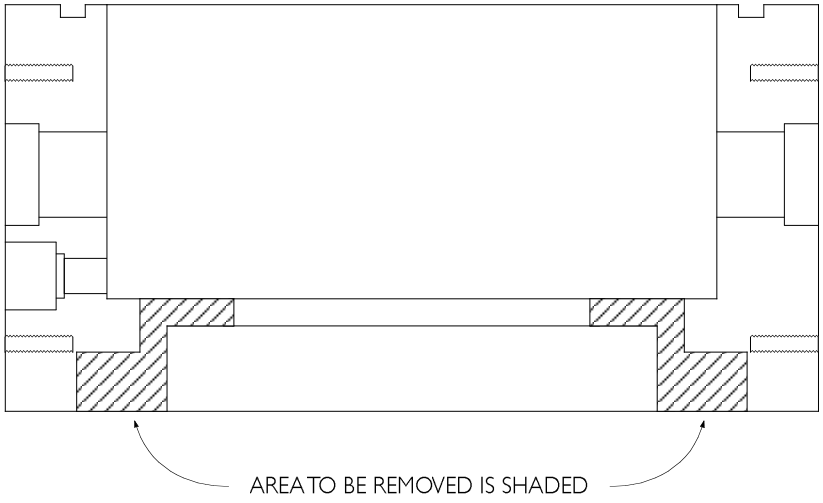

COLLAR (SECTION)
SHOWING AREA TO BE REMOVED
ALUMINUM
MEASURMENTS IN INCHES

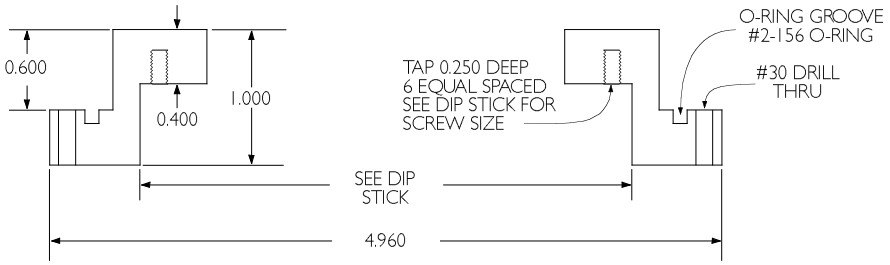

ADAPTER RING
ALUMINUM
MEASURMENTS IN INCHES

Pacific Northwest
NATIONAL LABORATORY

U.S. DEPARTMENT OF
ENERGY

Proudly Operated by **Battelle** *Since 1965*

902 Battelle Boulevard
P.O. Box 999
Richland, WA 99352
1-888-375-PNNL (7665)
www.pnl.gov